FACULDADE DE ENGENHARIA DA UNIVERSIDADE DO PORTO

Numerical Study of Supercritical CO_2 in an Orifice Geometry

Inês Maria Mestre dos Santos Silva



Master's in Mechanical Engineering

Supervisor (VKI): Dr. Jorge Pinho (Senior Research Engineer)

Supervisor (FEUP): Professor José Luis Alexandre

Co-Supervisor (FEUP): Professor Bruno Henrique Santos

Advisor (VKI): Dr. Maria Teresa Scelzo (Senior Research Engineer)

Advisor (VKI): Dr. Antonio Cantiani (Research Engineer)

October 9, 2026



von KARMAN INSTITUTE
FOR FLUID DYNAMICS

Numerical Study of Supercritical CO_2 in an Orifice Geometry

Inês Maria Mestre dos Santos Silva

Master's in Mechanical Engineering

October 9, 2026

Abstract

Supercritical carbon dioxide (sCO_2) has gained a lot of attention over the last year as a working fluid for power cycles due to the strong non-linear dependence of its thermophysical properties on temperature and pressure in the supercritical state. However, these unique thermophysical properties introduce numerical challenges when trying to simulate this fluid using computational fluid dynamics (CFD). The present dissertation presents a CFD model, developed using the software OpenFOAMv13, which seeks to predict the behaviour of CO_2 flow through an orifice geometry across a wide range of thermodynamic regimes, including subcritical and supercritical.

The CFD model was first developed using water (H_2O) as the working fluid and compared against CFD data present in the existing literature. For the water case, a mesh independence study was carried out to determine the most appropriate mesh, being selected the one with 25793 cells. Subsequently, the CFD model was tested using liquid CO_2 far and close to the critical point, and supercritical CO_2 far from the critical point without crossing the Widom line, and closer to the critical point crossing the Widom line. The discharge coefficient was selected as the parameter to assess the quality of the results. For the water case, a C_d of 0.748 was obtained, which was taken as the benchmark value for the following simulations. For Cases A_1, far from the critical point, and A_2, closer to the critical point,a deviation of -2.01% was obtained for both cases. Subsequently, the model was tested in supercritical conditions. Given the instabilities encountered when simulating sCO_2, adaptations to the CFD model initially developed were required for the remaining cases. For the case of sCO_2 without crossing the Widom line, the lowest deviation reported was -4.30%, obtained when introducing the correction for the compressible behaviour of the CO_2 under these conditions. For the case of sCO_2 crossing the Widom line, the lowest recorded was -3.74%. The deviations obtained for the discharge coefficient values against the water case, which was used as a benchmark value, show that the model yields consistent results across all thermodynamic regimes. After the adaptations required to deal with the numerical instabilities encountered, the model is capable of simulating supercritical CO_2 in an orifice geometry, within the limitations of the pseudo-phase change approach adopted.

Keywords: Supercritical carbon dioxide • Widom line • CFD • Orifice geometry • Discharge coefficient

Resumo

O dióxido de carbono supercrítico (CO_2) tem ganho bastante atenção nos últimos anos como fluido de trabalho para ciclos de potência, devido à forte dependência não linear das suas propriedades termofísicas com a temperatura e a pressão no estado supercrítico. No entanto, estas propriedades termofísicas distintas introduzem desafios numéricos na simulação deste fluido utilizando a dinâmica de fluidos computacional (CFD). A presente dissertação apresenta um modelo CFD, desenvolvido em OpenFOAM v13, para prever o comportamento do escoamento de CO_2 através de uma geometria de orifício numa vasta gama de regimes termodinâmicos, incluindo o subcrítico e o supercrítico.

O modelo CFD foi primeiramente desenvolvido utilizando água (H_2O) como fluido de trabalho e validado com dados de CFD presentes na literatura existente. Para o caso da água, foi realizado um estudo de independência de malha para determinar a malha mais adequada, tendo sido escolhida uma malha de 25793 células. Subsequentemente, o modelo CFD foi testado com CO_2 líquido longe e perto do ponto crítico, com CO_2 supercrítico sem atravessar a linha de Widom, e sCO_2 mais próximo do ponto crítico, atravessando a linha de Widom. O coeficiente de descarga foi selecionado como o parâmetro para avaliar a qualidade dos resultados. Para o caso da água foi obtido um C_d de 0,748, que foi tomado como valor de referência para as simulações seguintes. Para os Casos A_1, longe do ponto crítico, e A_2, mais próximo, foi obtido um desvio de -2,01% em ambos os casos. Posteriormente, o modelo foi testado em condições supercríticas. Devido às instabilidades numéricas que se verificaram durante as simulações de sCO_2, algumas alterações tiveram de ser aplicadas ao modelo CFD inicialmente desenvolvido. Após estas alterações, foi simulado um regime termodinâmico em que a linha de Widom não é atravessada, e para estas condições o menor desvio reportado foi de -4,30%, obtido ao introduzir a correção para o comportamento compressível do CO_2 nestas condições. Para o caso de sCO_2 atravessando a linha de Widom, o menor registado foi de -3,74%. Os desvios obtidos entre os coeficientes de descarga e o valor de referência, obtido no caso da água, demonstram que o modelo obteve resultados consistentes em todos os regimes termodinâmicos. Após as alterações necessárias para ultrapassar as instabilidades numéricas encontradas, o modelo demonstrou ser capaz de simular sCO_2 numa geometria de orifício, dentro das limitações do modelo de mudança de pseudo-fase adotado.

Palavras-chave: Dióxido de carbono supercrítico • Linha de Widom • CFD• Geometria orifício• Coeficiente de descarga

"Não tenhamos pressa, mas não percamos tempo."

José Saramago

Acknowledgements

I would like to express my gratitude to all those who contributed to the development and completion of this Master's thesis.

First, I would like to extend my sincere thanks to my supervisor at the von Karman Institute, Dr. Jorge Pinho, for his steady direction, valuable insights, and continuous academic support throughout this project. His guidance was essential to the realisation of this work.

I am equally thankful to Professor José Luis Alexandre for his academic support and guidance, which contributed significantly to the progress of this research.

My gratitude also goes to Professor Bruno Henrique Santos for his advice, constructive feedback, and assistance throughout the research process.

I would like to give a special mention to my advisor Dr. Antonio Cantiani, whose constant availability and guidance were fundamental to the execution of this work. I am also very grateful to Dr. Maria Teresa Scelzo for her help and valuable recommendations, which were essential for the work developed.

Finally, I would like to thank my family and friends for their continuous support, understanding, and encouragement throughout the course of my studies.

Inês Mestre Silva

Declaração de Honra

Declaro que a presente dissertação é de minha autoria e não foi previamente apresentada e avaliada nesta ou em outra instituição. As referências a outros autores (afirmações, ideias, pensamentos), assim como a utilização de trabalhos publicados respeitam escrupulosamente as regras da atribuição, e encontram-se devidamente indicadas no texto e nas referências bibliográficas, de acordo com as normas de referenciação. Tenho consciência de que a prática de plágio ou de autoplágio constituem ilícitos académicos, conforme estabelecido no Código de Ética da U.Porto.

Declaro, ainda, que utilizei ferramentas de Inteligência Artificial, nomeadamente Gemini e Claude, para a realização de parte(s) da presente dissertação, como instrumento de apoio no desenvolvimento do presente trabalho, especificamente no auxílio à pesquisa e seleção de literatura científica e na revisão, melhoria estilística e correção linguística do texto.

Inês Maria Mestre dos Santos Silva

Contents

List of Figures ix

List of Tables xiii

List of Acronyms xiv

List of Symbols xv

1 Introduction 1
- 1.1 Motivation . . . 1
- 1.2 Objectives . . . 3
- 1.3 Dissertation Structure . . . 4

2 Literature Review 6
- 2.1 Supercritical Fluids . . . 6
  - 2.1.1 Supercritical Carbon Dioxide . . . 8
- 2.2 Numerical Simulations of SCFs . . . 11
  - 2.2.1 Numerical Simulations of sCO_2 . . . 11
  - 2.2.2 Numerical Simulations of Water . . . 14

3 Numerical Framework & Theoretical Background 16
- 3.1 Pseudo-phase Change Model . . . 16
- 3.2 Volume of Fluid method . . . 18
- 3.3 Schnerr-Sauer Model Source Terms . . . 19
- 3.4 k-ε Turbulence Model . . . 20
- 3.5 Relevant Parameters for CFD . . . 21
  - 3.5.1 Mesh Quality Parameters . . . 21
  - 3.5.2 Courant Number . . . 22
- 3.6 Fundamentals of Flow Through an Orifice . . . 22
  - 3.6.1 Discharge Coefficient . . . 24

4 H_2O Numerical Simulations: Methodology & Validation 26
- 4.1 Methodology of H_2O Simulations . . . 26
  - 4.1.1 Geometry . . . 27
  - 4.1.2 Numerical Solver . . . 29
  - 4.1.3 Turbulence Model . . . 30

4.1.4 Boundary Conditions . . . 30
4.1.5 Convergence Criteria . . . 31
4.2 Mesh Independence Study . . . 31
4.2.1 Comparison of Results Against Reference Study . . . 37
4.2.2 Results of the Water Case . . . 40

5 CO_2 Numerical Simulations 42
5.1 Thermodynamic Regimes . . . 42
5.2 Case A - Liquid CO_2 . . . 43
5.2.1 Case A_1 Results . . . 44
5.2.2 Case A_2 Results . . . 46
5.3 Case B - Supercritical without Crossing the Widom Line . . . 49
5.3.1 Case B - Alterations to CFD Model . . . 49
5.3.2 Case B Results . . . 50
5.4 Case C - Supercritical Crossing the Widom Line . . . 55
5.4.1 Case C - Alterations to CFD Model . . . 55
5.4.2 Case C Results . . . 56
5.5 Summary of Results . . . 68

6 Conclusions 70

7 Future Work 73

References 75

A Simulation Results 78
A.1 Case Water . . . 78
A.2 Case A_1 . . . 81
A.3 Case A_2 . . . 84
A.4 Case B . . . 87
A.5 Case C - Polynomial Pressure . . . 92
A.6 Case C - Constant Pressure . . . 95

List of Figures

1.1 Schematic representation of a simple sCO_2 Brayton cycle [6]. 2
1.2 T-s diagram of the sCO_2 Brayton cycle. 2

2.1 Carbon dioxide p-T diagram [3]. 7
2.2 Transition of CO_2 through various phases: (a)–(c) sub-critical, (d)–(g) transition through the critical point, (h) supercritical fluid, (i) between supercritical fluid and superheated vapour, (j) superheated vapour, (k) compressed fluid and (l) between compressed fluid and supercritical fluid [3]. 8
2.3 Properties of CO_2 as a function of temperature at different supercritical pressures: (a) heat capacity, (b) density, (c) dynamic viscosity, and (d) thermal conductivity [3]. 9
2.4 p-T diagram for CO_2 showing both the saturation line (solid line), which delineates the subcritical phase boundary between liquid and vapour, and the Widom line (dashed line), which marks the positions of specific heat capacity maxima [12]. 10
2.5 Computational domain of the valve, 2D axisymmetric, used by [12]. 11
2.6 Computational domain of the circular orifice, 2D axisymmetric, used by [8]. . . . 12
2.7 Computational domain of the annular orifice, 2D axisymmetric, used by [8]. . . . 12
2.8 Computational domain of the two-tooth labyrinth seal, 2D axisymmetric, used by [10]. 13
2.9 Computational domain of the test section, 2D axisymmetric, used by [9]. 13
2.10 Computational domain of the laval nozzle, three-dimensional, used by [11]. . . . 14
2.11 Computational domain of the test section, three-dimensional, used by [20]. 15
2.12 Computational domain of the test section, two-dimensional, used by [21]. 15

3.1 C_p as a function of temperature at 77 bar [12]. 17
3.2 Interface tracking in VoF multiphase model [23]. 19
3.3 Static pressure distribution along an orifice plate, showing the position of the vena contracta [31]. 23
3.4 Flow pattern with an orifice plate [31]. 24

4.1 Diagram of the methodology of the dissertation. 27
4.2 Side view of the pseudo-axisymmetric computational domain. 28
4.3 Cross-sectional view of the wedge-shaped domain. 29
4.4 Detail of the orifice region of the computational domain (side view). 29
4.5 Example of mesh structure near the orifice for 8375 cells. 32
4.6 Scheme of D and $D/2$ tappings (not to scale). 33
4.7 Scheme of the locations of the velocity profiles (not to scale). 34

4.8 Pressure drop measured across the orifice, for D and $D/2$ tappings. 35
4.9 Velocity profile 47 mm upstream from the middle of the orifice (a). 35
4.10 Velocity profile 3 mm downstream from the middle of the orifice (b). 36
4.11 Velocity profile 53 mm downstream from the middle of the orifice (c). 36
4.12 Comparison of velocity profiles at 47mm upstream. 37
4.13 Comparison of velocity profiles at 3mm downstream. 38
4.14 Comparison of velocity profiles at 53mm downstream. 38
4.15 Velocity contour of water case for U_{inlet} of 0.755 m/s. 39
4.16 Velocity vectors of water case for U_{inlet} of 0.755 m/s. 39
4.17 (A) Velocity contour and (B) velocity vectors obtained by the reference study [20]. 39
4.18 Pressure contour of water case for U_{inlet} of 0.755 m/s. 41
4.19 Pressure along the axis of symmetry of water case for U_{inlet} of 0.755 m/s. 41
4.20 Temperature contour of water case for U_{inlet} of 0.755 m/s. 41

5.1 Representations of the cases simulated in the CO_2 p-T diagram. 43
5.2 Velocity contour of Case A_1 for U_{inlet} of 0.755 m/s. 45
5.3 Velocity vectors of Case A_1 for U_{inlet} of 0.755 m/s. 45
5.4 Pressure contour of Case A_1 for U_{inlet} of 0.755 m/s. 46
5.5 Temperature contour of Case A_1 for U_{inlet} of 0.755 m/s. 46
5.6 Velocity contour of Case A_2 for U_{inlet} of 0.755 m/s. 48
5.7 Velocity vectors of Case A_2 for U_{inlet} of 0.755 m/s. 48
5.8 Pressure contour of Case A_2 for U_{inlet} of 0.755 m/s. 48
5.9 Temperature contour of Case A_2 for U_{inlet} of 0.755 m/s. 48
5.10 Mass flow rate as a function of $\sqrt{\Delta p}$ between the inlet and outlet. 51
5.11 Velocity contour of Case B for p_{outlet} of 490 bar. 53
5.12 Velocity vectors of Case B for p_{outlet} of 490 bar. 53
5.13 Pressure contour of Case B for p_{outlet} of 490 bar. 53
5.14 Temperature contour of Case B for p_{outlet} of 490 bar. 53
5.15 Velocity contour of Case B for p_{outlet} of 380 bar. 54
5.16 Velocity vectors of Case B for p_{outlet} of 380 bar. 54
5.17 Pressure contour of Case B for p_{outlet} of 380 bar. 54
5.18 Temperature contour of Case B for p_{outlet} of 380 bar. 54
5.19 Mass flow rate as a function of $\sqrt{\Delta p}$ between the inlet and outlet. 57
5.20 Velocity contour of Case C for p_{outlet} of 170 bar, polynomial p_c. 59
5.21 α contour of Case C for p_{outlet} of 170 bar, polynomial p_c. 59
5.22 Pressure contour of Case C for p_{outlet} of 170 bar, polynomial p_c. 59
5.23 Temperature contour of Case C for p_{outlet} of 170 bar, polynomial p_c. 59
5.24 Velocity contour of Case C for p_{outlet} of 160 bar, polynomial p_c. 60
5.25 α contour of Case C for p_{outlet} of 160 bar, polynomial p_c. 60
5.26 Pressure contour of Case C for p_{outlet} of 160 bar, polynomial p_c. 61
5.27 Temperature contour of Case C for p_{outlet} of 160 bar, polynomial p_c. 61
5.28 Velocity contour of Case C for p_{outlet} of 145 bar, polynomial p_c. 61
5.29 α contour of Case C for p_{outlet} of 145 bar, polynomial p_c. 61
5.30 Pressure contour of Case C for p_{outlet} of 145 bar, polynomial p_c. 62
5.31 Temperature contour of Case C for p_{outlet} of 145 bar, polynomial p_c. 62
5.32 Velocity contour of Case C for p_{outlet} of 145 bar, constant p_c. 65
5.33 α contour of Case C for p_{outlet} of 145 bar, constant p_c. 65
5.34 Pressure contour of Case C for p_{outlet} of 145 bar, constant p_c. 65
5.35 Temperature contour of Case C for p_{outlet} of 145 bar, constant p_c. 66

5.36 Velocity contour of Case C for p_{outlet} of 140 bar, constant p_c. 67
5.37 α contour of Case C for p_{outlet} of 140 bar, constant p_c. 67
5.38 Pressure contour of Case C for p_{outlet} of 140 bar, constant p_c. 67
5.39 Temperature contour of Case C for p_{outlet} of 140 bar, constant p_c. 68

A.1 Velocity contour of water case for U_{inlet} of 0.5 m/s. 78
A.2 Velocity contour of water case for U_{inlet} of 0.5 m/s. 78
A.3 Pressure contour of water case for U_{inlet} of 0.5 m/s. 79
A.4 Temperature contour of water case for U_{inlet} of 0.5 m/s. 79
A.5 Velocity contour of water case for U_{inlet} of 1 m/s. 79
A.6 Velocity contour of water case for U_{inlet} of 1 m/s. 79
A.7 Pressure contour of water case for U_{inlet} of 1 m/s. 80
A.8 Temperature contour of water case for U_{inlet} of 1 m/s. 80
A.9 Velocity contour of Case A_1 for U_{inlet} of 0.5 m/s. 81
A.10 Velocity vectors of Case A_1 for U_{inlet} of 0.5 m/s. 81
A.11 Pressure contour of Case A_1 for U_{inlet} of 0.5 m/s. 81
A.12 Temperature contour of Case A_1 for U_{inlet} of 0.5 m/s. 82
A.13 Velocity contour of Case A_1 for U_{inlet} of 1 m/s. 82
A.14 Velocity vectors of Case A_1 for U_{inlet} of 1 m/s. 82
A.15 Pressure contour of Case A_1 for U_{inlet} of 1 m/s. 82
A.16 Temperature contour of Case A_1 for U_{inlet} of 1 m/s. 83
A.17 Velocity contour of Case A_2 for U_{inlet} of 0.5 m/s. 84
A.18 Velocity vectors of Case A_2 for U_{inlet} of 0.5 m/s. 84
A.19 Pressure contour of Case A_2 for U_{inlet} of 0.5 m/s. 84
A.20 Temperature contour of Case A_2 for U_{inlet} of 0.5 m/s. 85
A.21 Velocity contour of Case A_2 for U_{inlet} of 1 m/s. 85
A.22 Velocity vectors of Case A_2 for U_{inlet} of 1 m/s. 85
A.23 Pressure contour of Case A_2 for U_{inlet} of 1 m/s. 85
A.24 Temperature contour of Case A_2 for U_{inlet} of 1 m/s. 86
A.25 Velocity contour of Case B for p_{outlet} of 460 bar. 87
A.26 Velocity vectors of Case B for p_{outlet} of 460 bar. 87
A.27 Pressure contour of Case B for p_{outlet} of 460 bar. 87
A.28 Temperature contour of Case B for p_{outlet} of 460 bar. 88
A.29 Velocity contour of Case B for p_{outlet} of 440 bar. 88
A.30 Velocity vectors of Case B for p_{outlet} of 440 bar. 88
A.31 Pressure contour of Case B for p_{outlet} of 440 bar. 88
A.32 Temperature contour of Case B for p_{outlet} of 440 bar. 89
A.33 Velocity contour of Case B for p_{outlet} of 420 bar. 89
A.34 Velocity vectors of Case B for p_{outlet} of 420 bar. 89
A.35 Pressure contour of Case B for p_{outlet} of 420 bar. 89
A.36 Temperature contour of Case B for p_{outlet} of 420 bar. 90
A.37 Velocity contour of Case B for p_{outlet} of 400 bar. 90
A.38 Velocity vectors of Case B for p_{outlet} of 400 bar. 90
A.39 Pressure contour of Case B for p_{outlet} of 400 bar. 90
A.40 Temperature contour of Case B for p_{outlet} of 400 bar. 91
A.41 Velocity contour of Case C for p_{outlet} of 165 bar, polynomial p_c. 92
A.42 α contour of Case C for p_{outlet} of 165 bar, polynomial p_c. 92
A.43 Pressure contour of Case C for p_{outlet} of 165 bar, polynomial p_c. 92
A.44 Temperature contour of Case C for p_{outlet} of 165 bar, polynomial p_c. 92

A.45 Velocity contour of Case C for p_{outlet} of 155 bar, polynomial p_c. 93
A.46 α contour of Case C for p_{outlet} of 155 bar, polynomial p_c. 93
A.47 Pressure contour of Case C for p_{outlet} of 155 bar, polynomial p_c. 93
A.48 Temperature contour of Case C for p_{outlet} of 155 bar, polynomial p_c. 93
A.49 Velocity contour of Case C for p_{outlet} of 150 bar, polynomial p_c. 94
A.50 α contour of Case C for p_{outlet} of 150 bar, polynomial p_c. 94
A.51 Pressure contour of Case C for p_{outlet} of 150 bar, polynomial p_c. 94
A.52 Temperature contour of Case C for p_{outlet} of 150 bar, polynomial p_c. 94
A.53 Velocity contour of Case C for p_{outlet} of 170 bar, constant p_c. 95
A.54 α contour of Case C for p_{outlet} of 170 bar, constant p_c. 95
A.55 Pressure contour of Case C for p_{outlet} of 170 bar, constant p_c. 95
A.56 Temperature contour of Case C for p_{outlet} of 170 bar, constant p_c. 95
A.57 Velocity contour of Case C for p_{outlet} of 165 bar, constant p_c. 96
A.58 α contour of Case C for p_{outlet} of 165 bar, constant p_c. 96
A.59 Pressure contour of Case C for p_{outlet} of 165 bar, constant p_c. 96
A.60 Temperature contour of Case C for p_{outlet} of 165 bar, constant p_c. 96
A.61 Velocity contour of Case C for p_{outlet} of 160 bar, constant p_c. 97
A.62 α contour of Case C for p_{outlet} of 160 bar, constant p_c. 97
A.63 Pressure contour of Case C for p_{outlet} of 160 bar, constant p_c. 97
A.64 Temperature contour of Case C for p_{outlet} of 160 bar, constant p_c. 97
A.65 Velocity contour of Case C for p_{outlet} of 155 bar, constant p_c. 98
A.66 α contour of Case C for p_{outlet} of 155 bar, constant p_c. 98
A.67 Pressure contour of Case C for p_{outlet} of 155 bar, constant p_c. 98
A.68 Temperature contour of Case C for p_{outlet} of 155 bar, constant p_c. 98
A.69 Velocity contour of Case C for p_{outlet} of 150 bar, constant p_c. 99
A.70 α contour of Case C for p_{outlet} of 150 bar, constant p_c. 99
A.71 Pressure contour of Case C for p_{outlet} of 150 bar, constant p_c. 99
A.72 Temperature contour of Case C for p_{outlet} of 150 bar, constant p_c. 99

List of Tables

4.1 Geometric parameters of the geometry 29
4.2 k-ε turbulence model default coefficients [26] 30
4.3 Boundary conditions for the water case 31
4.4 Mesh quality parameters for the nine meshes used in the mesh independence study 33
4.5 Pressure drop measured across the orifice between the D and $D/2$ tappings 34
4.6 Post-processing results of the water case 40

5.1 Boundary conditions of the cases simulated 43
5.2 Inlet and outlet conditions for the CO_2 simulations of Case A_1 44
5.3 Post-processing results of Case A_1 45
5.4 Inlet and outlet conditions for the CO_2 simulations of Case A_2 47
5.5 Post-processing results of Case A_2 47
5.6 Inlet and outlet conditions of Case B 51
5.7 Post-processing results of Case B 51
5.8 Post-processing results of Case B, discharge coefficients 52
5.9 Inlet and outlet conditions for the CO_2 simulations, Case C with polynomial p_c . 56
5.10 Post-processing results of Case C with polynomial p_c 57
5.11 Post-processing results of Case C, discharge coefficients with polynomial p_c . . . 58
5.12 Inlet and outlet conditions for the CO_2 simulations, Case C with constant p_c . . . 63
5.13 Post-processing results of Case C with constant p_c 64
5.14 Post-processing results of Case C, discharge coefficients with constant p_c 64
5.15 Density comparison between the polynomial p_c and the constant p_c 66
5.16 Summary of discharge coefficient results 68

List of Acronyms

CFD	Computational Fluid Dynamics
FEUP	Faculty of Engineering of the University of Porto
ISO	International Organization for Standardization
LCO_2	Liquid Carbon Dioxide
PISO	Pressure Implicit with Splitting of Operators
SCF	Supercritical Fluid
sCO_2	Supercritical Carbon Dioxide
SS	Schnerr–Sauer
SST	Shear Stress Transport
VKI	von Karman Institute for Fluid Dynamics
VoF	Volume of Fluid

List of Symbols

Symbol	Description	Unit
C_1, C_2, C_3	k-ε turbulence-model coefficients	–
C_c	Condensation model coefficient	–
C_d	Discharge coefficient	–
C_p	Specific heat capacity at constant pressure	$\mathrm{J\,kg^{-1}\,K^{-1}}$
C_v	Vaporisation model coefficient	–
C_μ	Turbulent-viscosity model coefficient	–
Co	Courant number	–
D	Pipe diameter	m
d	Orifice diameter	m
D_k, D_ε	Effective diffusivities in the turbulence transport equations	$\mathrm{m^2\,s^{-1}}$
e	Orifice thickness	m
$\mathbf{F}_\sigma$	Surface-tension force per unit volume	$\mathrm{N\,m^{-3}}$
$\mathbf{g}$	Gravitational acceleration	$\mathrm{m\,s^{-2}}$
I	Turbulence intensity	–
k	Turbulent kinetic energy	$\mathrm{m^2\,s^{-2}}$
L	Length or reference length scale	m
$\dot{m}$	Mass flow rate	$\mathrm{kg\,s^{-1}}$
$\dot{m}_{pq}, \dot{m}_{qp}$	Mass transfer rate per unit volume from phase p to q, and from phase q to p	$\mathrm{kg\,m^{-3}\,s^{-1}}$
P	Turbulent kinetic energy production rate per unit volume	$\mathrm{kg\,m^{-1}\,s^{-3}}$
p	Static pressure	Pa
p_{sat}	Saturation Pressure	Pa
p_c	Pressure at the Widom line	Pa
R_b	Bubble radius	m
R_c, R_v	Condensation and vaporisation source terms	$\mathrm{kg\,m^{-3}\,s^{-1}}$
S_m	Mass source per unit volume	$\mathrm{kg\,m^{-3}\,s^{-1}}$
S_{α_q}	Source term for phase q in the volume-fraction equation	$\mathrm{kg\,m^{-3}\,s^{-1}}$
t	Time	s
T	Temperature	K
$\mathbf{u}, u, U$	Velocity	$\mathrm{m\,s^{-1}}$
x	Spatial coordinate	m
α	Volume fraction	–
β	Diameter ratio, d/D	–

Symbol	Description	Unit
ε	Turbulent kinetic energy dissipation rate	$m^2\,s^{-3}$
ε_{exp}	Expansibility factor in the discharge-coefficient equations	–
θ	Wedge angle	$^\circ$
κ	Isentropic exponent	–
μ	Dynamic viscosity	Pa s
ν_t	Turbulent kinematic viscosity	$m^2\,s^{-1}$
ρ	Density	$kg\,m^{-3}$
σ_k, σ_ε	Turbulence-model diffusivity parameters	–
ω	Specific turbulent dissipation rate	s^{-1}

Chapter 1

Introduction

This chapter introduces the dissertation by outlining its overall structure and providing context for the work carried out. The present thesis investigates numerical modelling approaches for supercritical CO_2 flow through an orifice geometry. Initially, a numerical study of orifice flow using water as a working fluid, available in the literature, was reproduced to establish a validated basis for the model. Following this, the modelling of CO_2 across various thermodynamic regimes, including subcritical and supercritical, was conducted.

This dissertation was conducted within the framework of a collaborative partnership between the Faculty of Engineering of the University of Porto (FEUP) and the von Karman Institute for Fluid Dynamics (VKI).

1.1 Motivation

Due to the increase in energy consumption and the search to improve sustainability, there is a growing demand for energy utilisation efficiency and reduced environmental impact. As a result, the search to improve energy utilisation and transformation efficiency, while ensuring the minimisation of environmental pollution, has been the focus of concern of many researchers [1], [2]. Therefore, there is a current need to propose more efficient energy conversion systems or power cycles in place of existing ones to improve energy utilisation. The supercritical carbon dioxide Brayton cycle, in recent years, has sparked some interest in the research fields of solar, nuclear and coal-fired power plants due to its promising advantages both in the traditional and renewable energy fields [1], [3], [4]. The Brayton cycle consists of a thermodynamic cycle that converts heat into work through four steps: compression, heat addition, expansion through a turbine, and heat rejection, with the goal of producing work [5]. The sCO_2 cycle consists of the Brayton cycle using carbon dioxide, above its critical point, which is given approximately at a temperature of 304.25 K, and a pressure of 7.39MPa, as the working fluid [3], [6]. When the sCO_2 power cycle is integrated in solar, nuclear and coal-fired power plants, these last act as the heat source during the heat addition process of the Brayton cycle [1]. Figures 1.1 and 1.2 illustrate the schematic of

a closed-loop sCO_2 Brayton cycle, including the operating points of each process, all of which sit above the critical point of CO_2, and the respective T-s diagram.

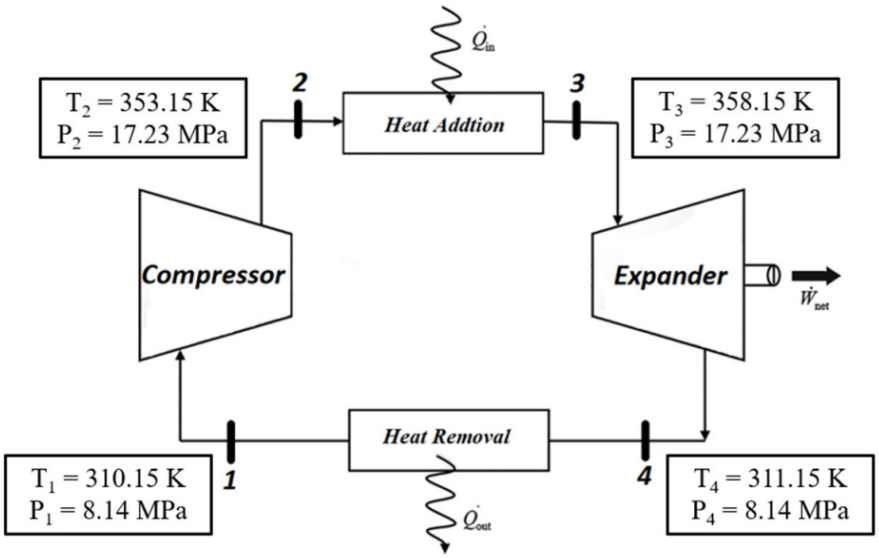

Figure 1.1: Schematic representation of a simple sCO_2 Brayton cycle [6].

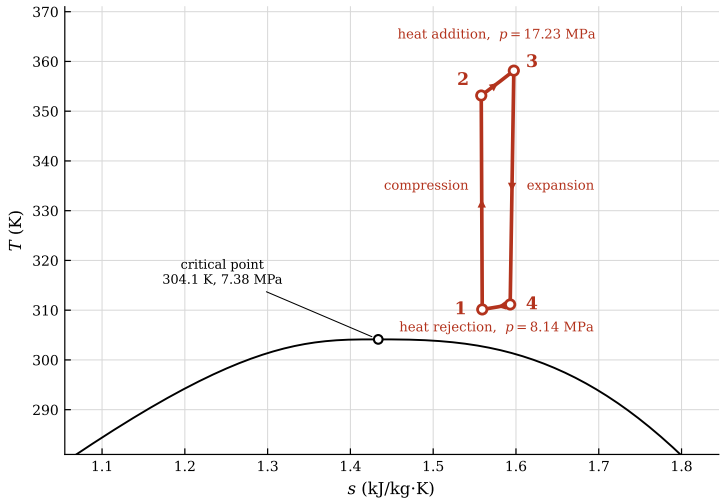

Figure 1.2: T-s diagram of the sCO_2 Brayton cycle.

According to published studies, the sCO_2 cycle has been characterised by its high thermal efficiency, smaller components and compact footprint [7]. These advantages arise from the particular thermophysical properties that characterise the behaviour of carbon dioxide in the supercritical state. The thermophysical properties of supercritical fluids exhibit a strong and non-linear dependence on both temperature and pressure, resulting in exceptionally steep property gradients that become more pronounced as the carbon dioxide approaches the vicinity of the critical point [3]. For instance, it was reported by [7] that there is a consensus that the properties of supercritical

CO_2, especially close to the critical point, play a vital role in reducing the compressor work and hence bringing relatively high cycle thermal efficiency. Among these, many other studies enumerate benefits that arise from using supercritical carbon dioxide as a working fluid.

However, achieving these efficiency and compactness gains in practise, depends on the ability to predict the dynamics of carbon dioxide in the supercritical state in the key components of the Brayton cycle. This has motivated a growing number of numerical studies with the goal of modelling the behaviour of supercritical carbon dioxide in different applications, all within the context of the Brayton cycle. For instance, [8] presented a methodology for the CFD simulation of sCO_2 through a restriction to study an accidental scenario such as a pipe break and [9] carried out an analysis of the critical flow of CO_2 in the nozzle tube with computational fluids dynamics. Another study was conducted by [10] which intended to numerically model supercritical carbon dioxide flow in see-through labyrinth seals to provide some guidelines for the design of labyrinth seals using sCO_2 for turbomachinery. Other studies carried out analysis on a more broad perspective, for example [11] presented a study on the enhancement of the accuracy in predicting the performance of a supercritical CO_2 compressor in closed Brayton Cycles using CFD. Furthermore, a previous study has been conducted at the von Karman Institute, which sought to model sCO_2 through the implementation of a methodology designated the pseudo-phase change model in a valve geometry, to model the crossing of the Widom line which divides the supercritical domain of CO_2 [12].

Although the presented literature reveals a growing interest in the use of CFD tools to predict the behaviour of supercritical carbon dioxide, the literature is still not yet very extensive due to the numerical difficulties encountered when trying to simulate sCO_2. As cited by [13], density and viscosity play a significant part in the momentum transport, and the thermal conductivity and specific heat in the energy transport. As mentioned previously, the thermophysical properties of supercritical carbon dioxide exhibits pronounced variations, particularly in the region near the critical point. This inherently poses challenges in maintaining both stability and precision when solving these equations. Indeed, most of the challenges encountered in modelling sCO_2 can be traced back to the dramatic and non linear variations in its thermophysical properties.

In the work presented in this dissertation, it is sought to develop a CFD model to numerically predict the behaviour of sCO_2, under a wide range of thermodynamic regimes, including the supercritical in an orifice geometry. This model is intended to model sCO_2 simplifying the previously adopted geometry and to support the sizing of an orifice to be tested at the von Karman Institute's sCO_2 facility.

1.2 Objectives

The main objective of this dissertation is to develop a CFD model for sCO_2 flow through an orifice geometry. Modelling supercritical CO_2 presents several sources of numerical instability, arising from the strong dependence of the properties on temperature and pressure. This sensitivity, as discussed in the previous section, makes CO_2 in a supercritical state a particularly interesting fluid to study, but also a particularly challenging one to model numerically.

To address this, the work first reproduces a CFD model of an orifice operating with water, based on previously published CFD results, to serve as a basis for the subsequent CO_2 model. This model is tested and adapted for CO_2 across a wide range of thermodynamic regimes, including subcritical and supercritical. Liquid conditions are the first to be considered in Case A, which is further divided into Case A_1, below the critical temperature and pressure, and Case A_2, below the critical temperature and above the critical pressure. Case A is conducted to validate the results of the model with CO_2 as the working fluid against those using water. Subsequently, Case B is considered, simulating carbon dioxide far from the critical point and without crossing the Widom line. Lastly, the model is tested in Case C, under supercritical conditions closer to the critical point, where the Widom line is crossed.

1.3 Dissertation Structure

In this section the structure of the present dissertation is outlined. This document is organised in seven chapters, containing the following information:

- **Chapter 1:** in the first chapter the motivation and objectives of the present dissertation are introduced;
- **Chapter 2:** a literature review on the characterisation of supercritical fluids, with particular attention to carbon dioxide is presented. Subsequently, the state of the art in modelling approaches for water and sCO_2 in flow-restricting geometries is detailed;
- **Chapter 3:** the necessary theoretical background and numerical concepts for the work conducted in the thesis in introduced in this chapter. First the pseudo-phase change model, Volume of Fluid (VoF) method, and the Schnerr-Sauer (SS) cavitation model are presented. Second, the equations of the k-ε turbulence model are introduced. Third, relevant parameters for the CFD model development are explained. Lastly, an explanation of the fluid mechanic principles behind the flow through a flow-restricting geometry is presented;
- **Chapter 4:** the methodology behind the development of the CFD model with water as working fluids is presented. Following this, a mesh sensitivity analysis was carried out and the results are compared against data from a CFD model present in the literature. The obtained results from the CFD model are further processed and analysed to serve as a baseline for comparison and analysis of all the thermodynamic regimes to be tested with CO_2;
- **Chapter 5:** in this section the thermodynamic regimes to be tested with the CFD model are outlined. For each case conducted, the alterations to the CFD model established in the pervious chapter are reported, and the obtained results are presented along with a detailed discussion;
- **Chapter 6:** the main conclusions drawn from the work conducted in the present dissertation are summarised and presented in this section;

- **Chapter 7:** this section outlines potential directions for future work building on the results and methodology presented in this dissertation.

Chapter 2

Literature Review

The purpose of this chapter is to provide the theoretical background necessary to contextualise the numerical work developed in this dissertation. First, the supercritical fluids (SCFs) are introduced, with particular attention to supercritical carbon dioxide, its thermophysical properties, and behaviour in the vicinity of the critical point. Subsequently, a review of the state of the art in computational fluid dynamics modelling of water and SCFs is presented.

2.1 Supercritical Fluids

A fluid can be defined as a substance capable of flowing that does not retain a fixed shape. Under this definition, both liquids and gases are classified as fluids. A liquid represents a condensed state of matter, that, upon heating, undergoes a phase transition into a gaseous phase [14].

This transformation can be represented on a pressure-temperature (p-T) diagram, as for example the one illustrated in Figure 2.1 for CO_2 [3]. Additionally, it is represented in the p-T diagram, the vapour-pressure curve, which delineates the boundary between the liquid and the gas regions and defines the conditions under which these two phases coexist [15]. The point at where this curve terminates is known as the critical point, defined by the corresponding critical pressure and critical temperature, which are characteristic to each fluid [14].

A fluid is said to be in a supercritical state when it is maintained at or above its characteristic critical pressure and critical temperature. Under these conditions, the liquid and gas phases become physically indistinguishable. This implies that when in a supercritical state, the fluid exists as a single homogeneous phase that may be conceptualised either as a liquid with reduced density or a highly compressed gas [3], [15], [16], [17]. This behaviour is illustrated in Figure 2.1 shows photographs of carbon dioxide held in a view cell at the conditions indicated, with (a) to (c) below both the critical temperature and the critical pressure, (d) to (g) at the critical point, (h) above both and therefore supercritical, (i) and (j) above the critical temperature but below the critical pressure, corresponding to a superheated vapour, and (k) and (l) below the critical temperature but above the critical pressure, corresponding to a compressed liquid [3].

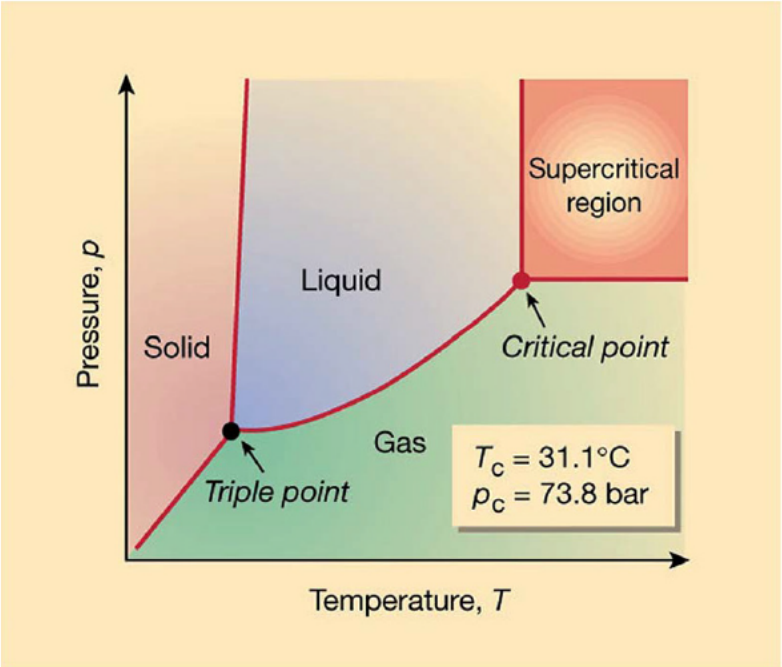

Figure 2.1: Carbon dioxide *p*-*T* diagram [3].

SCFs exhibit highly unique thermophysical properties [12] and, consequently, have attracted a growing research interest due to their unusual behaviour and wide range of potential applications. The *p*-*T* region in the vicinity of the critical point is, from a physical standpoint, the most interesting region, as mentioned in Section 1.1, since the majority of the thermophysical properties become strongly dependent on both pressure and temperature [14]. This sensitivity arises because, at the critical point, the distinction between the coexisting liquid and vapour phases vanishes, and the isothermal compressibility of the single-phase fluid diverges. In the supercritical region, a liquid-like density can transition continuously into a vapour-like density state by varying the pressure or temperature, without the appearance of a phase interface [15].

Despite all SCFs presenting highly interesting characteristics, supercritical CO_2 has received particular attention and stands as the leading candidate for industrial applications, due to the relative ease with which its critical point can be reached [18]. A dedicated literature review on sCO_2 is presented in the Subsection 2.1.1.

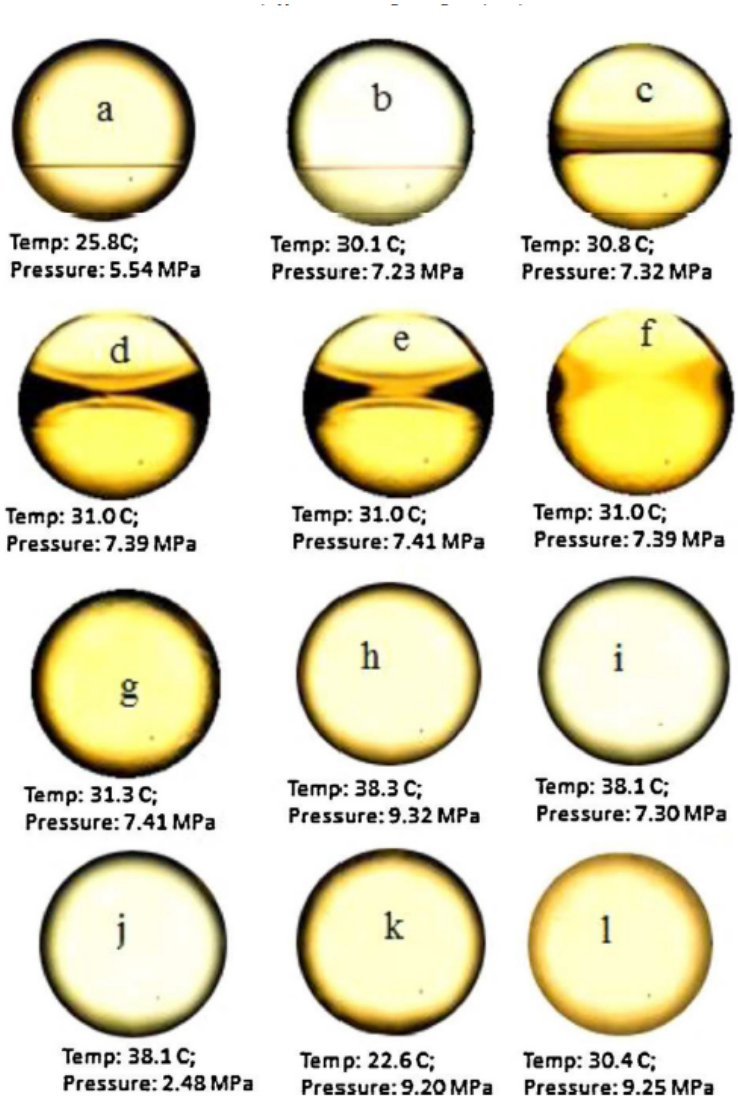

Figure 2.2: Transition of CO_2 through various phases: (a)–(c) sub-critical, (d)–(g) transition through the critical point, (h) supercritical fluid, (i) between supercritical fluid and superheated vapour, (j) superheated vapour, (k) compressed fluid and (l) between compressed fluid and supercritical fluid [3].

2.1.1 Supercritical Carbon Dioxide

As mentioned above, sCO_2 is one of the most attractive SCFs. Carbon dioxide reaches its critical point at a critical temperature of 304.25 K and a critical pressure of 7.39MPa [3] [15]. However, it should be noted that these values are not precisely fixed, as small discrepancies may be noticed between different literatures, which arise from the inherent difficulty in precisely measuring the critical point conditions. For instance, [15] reports values of 304.13 K and 7.377 MPa. Regardless of the values considered, both sets place the critical point of CO_2 within a range that is technically accessible under realist engineering conditions, which is one of the underlying causes of the widespread interest in its supercritical applications.

As introduced earlier, the thermophysical properties of supercritical fluids exhibit a strong and non-linear dependence on both temperature and pressure, resulting in exceptionally steep property gradients that become more pronounced as the carbon dioxide approaches the vicinity of the critical point. In the Figure 2.3 is illustrated the isobaric heat capacity (a), the density (b), dynamic viscosity (c), and thermal conductivity (d), as a function of the temperature and pressure [3].

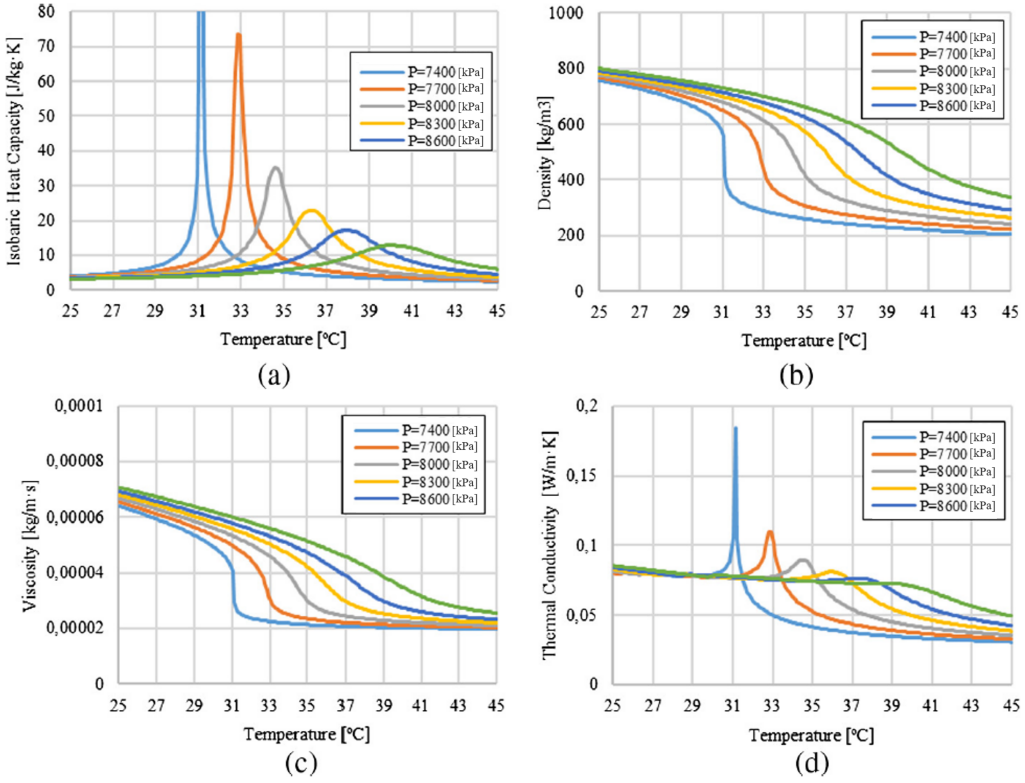

Figure 2.3: Properties of CO_2 as a function of temperature at different supercritical pressures: (a) heat capacity, (b) density, (c) dynamic viscosity, and (d) thermal conductivity [3].

For instance, this behaviour is most clearly illustrated by the isobaric heat capacity, C_p, shown in Figure 2.3 (a). At a constant pressure, increasing the temperature initially, there is a progressive rise in C_p, with the rate of increase accelerating substantially as the temperature approaches its critical value, illustrating the steep gradients noticeable in the vicinity of the critical point mentioned previously. Beyond reaching this point, as the temperature increases further from the critical point, the isobaric heat capacity values begin to decrease sharply, with the rate of decrease decelerating as the temperature increases. This trend can be observed at a wide range of pressures, however, as the pressure approaches the critical pressure, this peak becomes progressively sharper, with the C_p curve eventually reaching a divergent asymptote at the critical point. These peaks in the C_p curves delineate a separation between two characteristic zones of the p-T diagram, on the left of the peak, at lower temperatures, sCO_2 exhibits liquid-like thermophysical properties, such as high density and low compressibility, while to the right, at higher temperatures, the fluid takes on a gas-like

characteristic, including lower density and higher compressibility [3].

Although the other thermophysical properties are not characterised by as sharp a gradient as what happens in the case of isobaric heat capacity, they share the same underlying tendency for steep gradients near the critical and critical conditions. As illustrated for density, viscosity, and thermal conductivity in Figures 2.3 (b), (c), and (d), respectively, as the pressure values approach the critical pressure, the variation of both properties with the temperature variation becomes more pronounced [3].

Considering the peaks identified in the isobaric heat capacity graph across a range of pressures and temperatures, one can define a curve in the pressure-temperature diagram, as illustrated in Figure 2.4. This graph shows the *p*-*T* diagram of carbon dioxide, representing the liquid, gas, and supercritical regions [12]. This curve is known as the Widom line and is defined as the set of thermodynamic states at which the thermodynamic response functions attain local maxima [7], [14]. As illustrated in Figure 2.4, the Widom line marks the continuous crossover between liquid-like and gas-like behaviour in the supercritical region, playing a fundamental role in characterising thermophysical property variations [12].

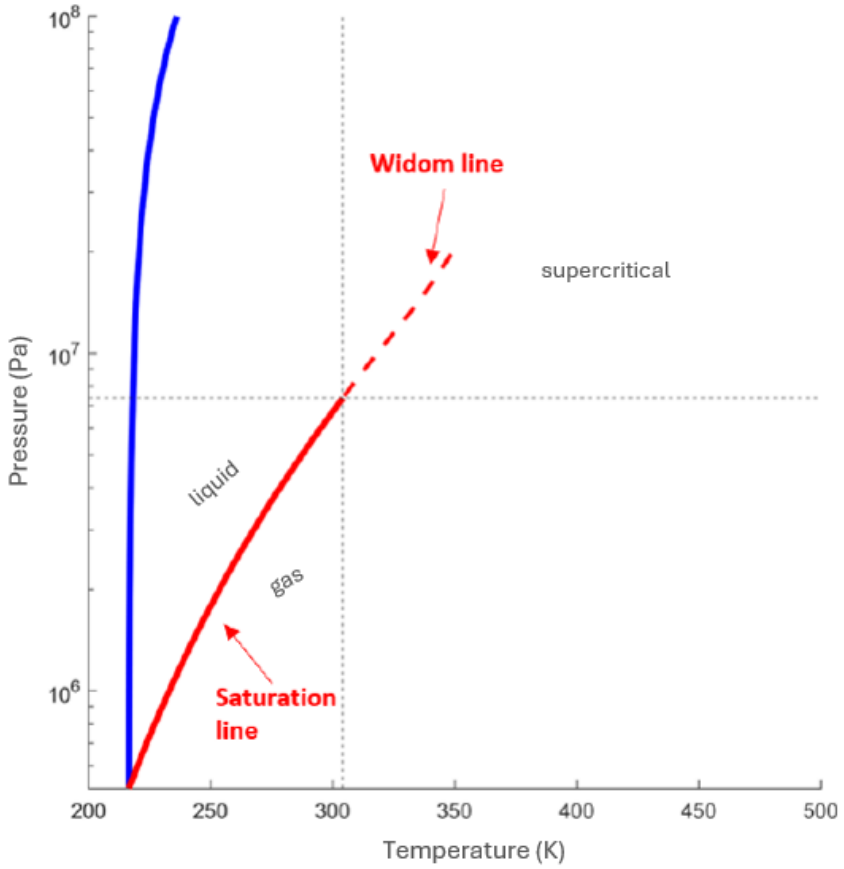

Figure 2.4: *p*-*T* diagram for CO_2 showing both the saturation line (solid line), which delineates the subcritical phase boundary between liquid and vapour, and the Widom line (dashed line), which marks the positions of specific heat capacity maxima [12].

2.2 Numerical Simulations of SCFs

The behaviour of supercritical fluids can be modelled using Computational Fluid Dynamics. However, due to the thermophysical characteristics of these fluids described in the 2.1.1, this modelling is a complex procedure with significant numerical challenges. This chapter provides a background literature review of the CFD models and numerical approaches relevant to the present study, including prior work conducted at the von Karman Institute in the project in which this dissertation is inserted.

2.2.1 Numerical Simulations of sCO_2

In this section, the state of the art in CFD modelling of supercritical carbon dioxide is reviewed. Initially, the prior work conducted at the von Karman Institute, within which this dissertation is framed, is presented. Subsequently, the existing literature on sCO_2 numerical modelling in flow-restricting geometries is reviewed. The purpose of this review is to identify which are the most commonly selected geometries, turbulence models, CFD softwares, and CO_2 thermodynamic regimes for modelling this supercritical fluid.

The previous work carried out at the institute focused on developing a CFD model of a valve operating with sCO_2, validating it, and analysing the valve's behaviour and performance under various thermodynamic conditions. The geometry implemented in the CFD is illustrated in Figure 2.5, and consists of a two-dimensional (2D) pseudo-axisymmetric representation of a valve [12]. In this work the simulations were conducted in OpenFOAM, implementing the k-ω SST turbulence model, without comparison to any other turbulence models available [12]. The flow was simulated across a wide range of conditions on the p-T diagram, including subcritical, supercritical far and across the Widom line.



Figure 2.5: Computational domain of the valve, 2D axisymmetric, used by [12].

To approach the sCO_2 modelling across the Widom line, a pseudo-phase change model was implemented. The underlying idea behind this model it that the supercritical fluid, which in this case is the CO_2, is treated as a two-phase system in the vicinity of the critical point, with the thermophysical properties split across the Widom line, which as mentioned previously conceptually separates the liquid-like and gas-like behaviour of the sCO_2. The objective of this approach is to overcome the limitations of simulating SCFs by treating the liquid-like and gas-like regions as separate phases which means the C_p function, which previously was non-monotonic, becomes

monotonic within each region. In Section 3.1 the pseudo-phase change model is explained in more detail.

Other numerical studies have also focused on modelling carbon dioxide in a supercritical state in flow-restricting geometries. For instance, the flow of sCO_2 through orifice geometries has been investigated in [8], where both circular and annular configurations were considered as illustrated in Figures 2.6 and 2.7, respectively.

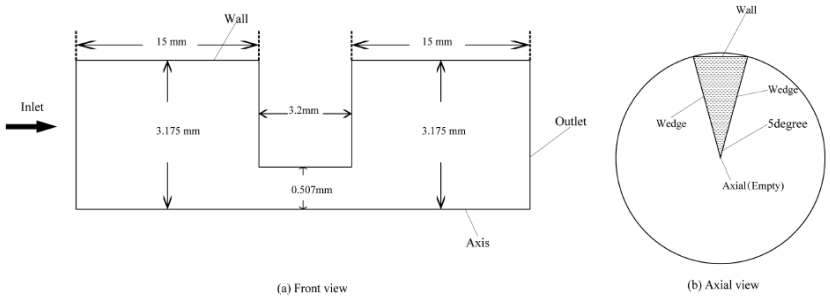

Figure 2.6: Computational domain of the circular orifice, 2D axisymmetric, used by [8].

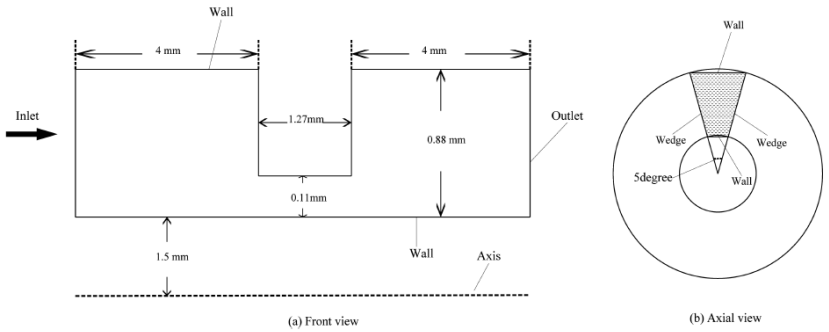

Figure 2.7: Computational domain of the annular orifice, 2D axisymmetric, used by [8].

In this work CFD simulations are carried out in OpenFOAM to model an accident scenario in an sCO_2 power cycle, such as a pipe break, where the inventory of sCO_2 leaks out of the system. For this scenario, the study models the CO_2 going supercritical conditions to subcritical where two phases may appear, both liquid and gas. The main goal is to identify the flow rate that goes through the orifice during the leakage. A comparison between the standard k-ε and k-ω SST turbulence models was performed to assess their influence on the predicted mass flow rate, with the results indicating minimal difference between the two approaches.

In following work conducted by the same authors using the same software, CFD modelling of sCO_2 in labyrinth seal geometries, with two-phase appearing at the outlet of the geometry was conducted [10]. The main objective of this work was to optimise the see-through labyrinth seal configuration to provide guidelines for see-through labyrinth seal in turbomachinery using sCO_2. Considering the minimal difference in results reported in [8], the authors opted to conduct the numerical simulations using the standard k-ε model. Although, the application is different

the resulting computational domain for the simulations is similar to that of the flow-restricting geometries mentioned in the previous section, as illustrated in Figure 2.8.

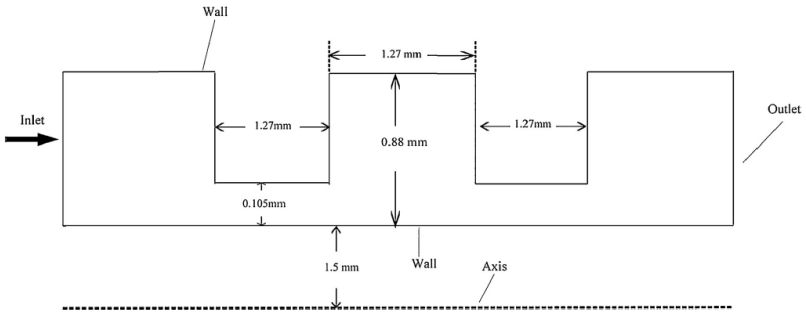

Figure 2.8: Computational domain of the two-tooth labyrinth seal, 2D axisymmetric, used by [10].

A comparable study was presented in [19], which similarly targeted the optimisation of a see-through labyrinth seal configuration through CFD. Similarly to the work reported in [10], the authors implemented the standard k-ε turbulence model, without carrying out a turbulence model analysis.

In a more detailed study conducted in a dissertation of one of the authors from the previous works presented [17], both the standard k-ε and the k-ω SST turbulence models were assessed for this classes of geometries, with the authors concluding that either model was suitable, with the standard k-ε model being preferred due to is superior numerical stability and roughness. The model was validated against experimental data available in the literature, as well as data obtained by the authors. In this study several geometries were taken into consideration such as valve, circular orifice, annular orifice and see-through labyrinth seal, similar to those illustrated in Figures 2.5, 2.6, 2.7, and 2.8, respectively.

Beyond orifice and labyrinth seal geometries, sCO_2 flow has been numerically investigated in other relevant configurations. In [9], the flow through a nozzle tube was simulated using the standard k-ε model, selected on account of the high Reynolds number characteristic of the case. Figure 2.9 illustrates the domain of the nozzle tube used in the CFD simulations conducted in Ansys FLUENT.

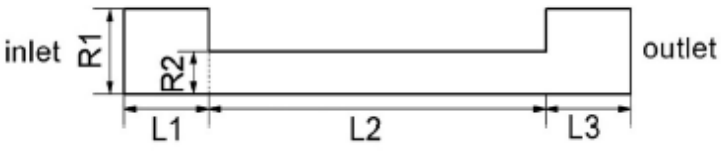

Figure 2.9: Computational domain of the test section, 2D axisymmetric, used by [9].

Other relevant work to be considered is the CFD model developed for modelling a laval nozzle, whose domain is shown in Figure 2.10, operating across conditions from the supercritical regime to a subcritical state where two-phases appear [11]. For this application the k-ω SST turbulence

model was employed, without any comparison to other existing models and an explicit justification on the reasoning behind the selection. The purpose of this work was to enhance the robustness and accuracy of a sCO_2 compressor, using the commercial solver NUMECA FINE/Turbo.

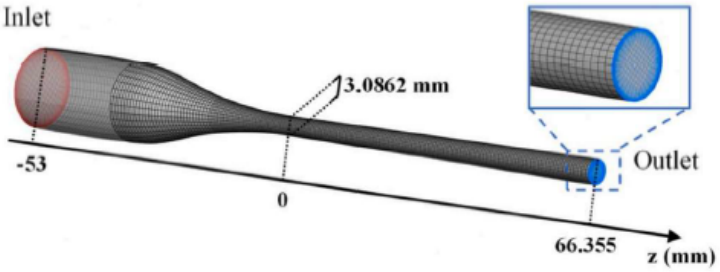

Figure 2.10: Computational domain of the laval nozzle, three-dimensional, used by [11].

Several conclusions can be drawn from the studies reviewed in this section. Regarding the turbulence model, the standard k-ε and k-ω SST were the most common choices. The works that compared the two models reported minimal differences and a preference for the k-ε due to its superior numerical stability. Two-dimensional axisymmetric domains are the main choice of these studies for this class of geometries, and OpenFOAM is the most widely adopted software.

2.2.2 Numerical Simulations of Water

In this section, a brief literature review on CFD modelling of water in orifice geometries is presented. Although the primary focus of this work concerns sCO_2 flow, before simulating the CO_2, the CFD model is developed using water as a working fluid. Hence, numerical studies involving water as the working fluid are also reviewed to identify the most common approaches to simulate water in an orifice geometry, and to identify a suitable study to reproduce as the basis of the CFD model for this dissertation.

The flow through orifice geometries has been numerically investigated using water as the working fluid in several studies. A study in the literature performed a CFD analysis of flow through an orifice meter, with the objective of predicting the flow pattern and the vena contracta position [20]. To achieve this, several simulations were carried out using both water and air as the working fluid, across a wide range of geometric parameters and thermodynamic regimes. The simulations were performed in OpenFOAM, implementing the standard k-ε turbulence model, which was chosen due to its simplicity and extensive validation in the literature for this type of application. A three-dimensional representation of the orifice was adopted for the computational domain, as illustrated in Figure 2.12.

A comparable study was carried out by [21], assessing the same quantities of interest, the flow pattern and the position of the vena contracta, through a similar numerical approach. Although the software used for the simulations is not disclosed, the standard k-ε model was implemented, for the same reasons of computational cost and extensive validation reported in the study described

above. In this study, a two-dimensional domain of the orifice geometry, illustrated in Figure 2.12, was adopted.

Both studies adopted the standard k-ε turbulence model, chosen for the same reasons of computational cost and extensive validation, indicating that this approach is widely applied for the simulation of flow through orifice geometries with water.

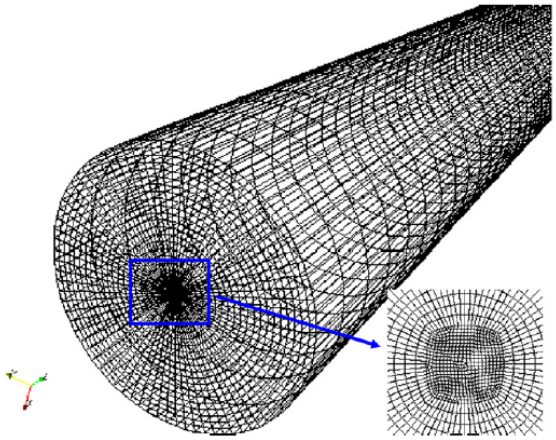

Figure 2.11: Computational domain of the test section, three-dimensional, used by [20].

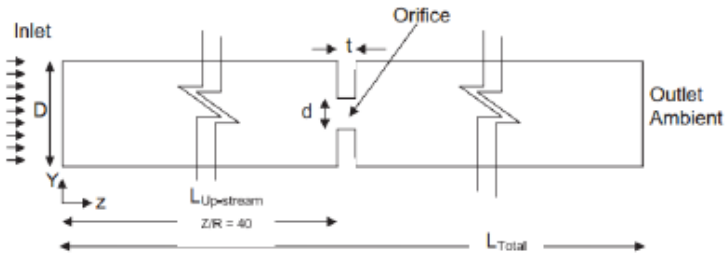

Figure 2.12: Computational domain of the test section, two-dimensional, used by [21].

Chapter 3

Numerical Framework & Theoretical Background

In this chapter, the numerical framework and theoretical background are presented. Initially, the pseudo-phase change model, VoF method, and the Schnerr-Sauer model are presented. Subsequently, the k-ε turbulence model is presented, followed by the introduction of relevant concepts for the CFD model. Lastly, a section detailing the flow physics and relevant parameters for post-processing are presented.

3.1 Pseudo-phase Change Model

The pseudo-phase change model consists of a modelling approach which treats SCFs as a two-phase system in the vicinity of the critical point by implementing a solver that is tailored for two-phase flow simulations, such as the compressibleVoF. The main concept behind adopting a two-phase flow modelling approach, although for a supercritical fluid is not physically possible to distinguish the liquid from the gas, and so the mixture is homogeneous, is to overcome the limitations encountered when simulating supercritical fluids.

In the pseudo-phase change model, thermodynamic properties are split according to the Widom Line. To the left of the Widom line, at lower temperatures, the supercritical CO_2 presents a more liquid-like behaviour, while to the right, at higher temperatures, it presents more gas-like behaviour. As discussed in Chapter 2, thermophysical properties such as the specific heat at constant pressure, C_p, exhibit a sharp, near-singular peak at the Widom line, as illustrated in Figure 3.1. By separating the liquid-like properties to the left of the Widom line from the gas-like properties to the right, a single non-monotonic property function is replaced by two monotonic functions. This separation helps mitigate the numerical difficulties that arise in CFD simulations of supercritical CO_2 [12].

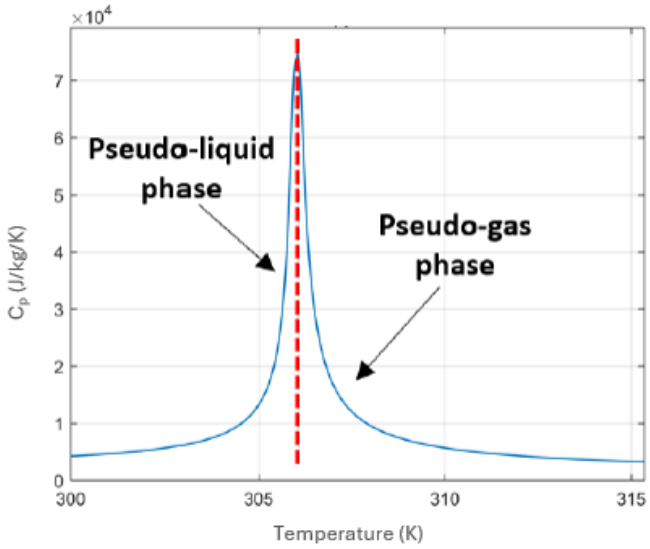

Figure 3.1: C_p as a function of temperature at 77 bar [12].

In order to handle this, a set of thermophysical properties is defined for each phase, liquid-like and gas-like. The interface between the phases must be accurately resolved, either by explicitly tracking its motion or by modelling the interaction between phases. A method commonly employed for this purpose is the Volume of Fluid method, which introduces an additional scalar field, typically denoted by the Greek letter α. If $\alpha = 1$, the cell contains one pure phase, and if $\alpha = 0$, it contains the other. A dedicated transport equation is solved for α , and advanced numerical techniques ensure accurate interface capturing. Once α is known, the mixture's thermophysical properties can be obtained cell-by-cell as a weighted average of the two phases, weighted by their local volume fractions. This formulation enables solving a single set of conservation equations for mass, momentum, and energy to be solved across the whole domain, rather than separate equations for each phase, while still accounting for the distinct nature of each phase. To implement the pseudo-phase change model to represent the crossing of the Widom line, it is necessary to adopt a model to impose the change between the liquid-like and gas-like phases based on the local pressure and temperature. For the present dissertation, the Schnerr-Sauer cavitation model was selected for the modelling of the pseudo-phase change, which will be presented in further detail in Section 3.3.

Although a cavitation model is being implemented to simulate sCO_2, in supercritical fluids the pseudo-phase change across the Widom line does not involve bubble nucleation or the presence of a physical interface. Therefore, no activation energy or time delay, which are imposed by the cavitation models, should be expected in the transition. Consequently, using a cavitation model to represent supercritical CO_2 near the critical point is not physically accurate, since cavitation is not a phenomenon that actually occurs in supercritical CO_2 when crossing the Widom line, it is used only as an approach to overcome the numerical instabilities inherent to SCFs modelling.

Nevertheless, it is believed that these effects do not produce a substantial effect on the predicted behaviour of the flow through the orifice, and thus it was considered that this approach was suitable for the current CFD model.

3.2 Volume of Fluid method

When modelling two-phase flows, there are two possible approaches: the two-fluid and the single-fluid formulation. In the two fluid formulation, the domain is split into individual subdomains filled with distinct fluids. In this formulation, the Navier-Stokes equations are solved in each subdomain, and the solutions are coupled at the interface. In the single-fluid formulation, instead of solving the governing equations for each phase separately, one can use one set of governing equations for the whole domain with phase properties abruptly changing across the interface [22].

The Volume of Fluid method is characterised as a single-fluid strategy, as it is a surface-tracking technique that only uses a single set of momentum equations shared by the fluids. The tracking method throughout the computational domain is done through the additional scalar field α, mentioned previously. This scalar field α consists of a sharp representation of the interface between immiscible fluids [22]. The compressibleVoF solver available in OpenFOAMv13 implements this methodology, meaning it is a single-fluid approach with shared properties weighted by the volume fraction.

For a compressible formulation, the governing equations of continuity, momentum for the mixture, and volume fraction equation defined for two phases, q and p, are given by,

$$\frac{\partial \rho}{\partial t} + \nabla \cdot (\rho \mathbf{u}) = S_m \tag{3.1}$$

$$\frac{\partial (\rho \mathbf{u})}{\partial t} + \nabla \cdot (\rho \mathbf{u}\mathbf{u}) = -\nabla p + \nabla \cdot \left[\mu \left(\nabla \mathbf{u} + \nabla \mathbf{u}^T\right)\right] + \rho \mathbf{g} + \mathbf{F}_\sigma \tag{3.2}$$

$$\frac{1}{\rho_q}\left[\frac{\partial}{\partial t}(\alpha_q \rho_q) + \nabla \cdot (\alpha_q \rho_q \mathbf{u})\right] = \frac{1}{\rho_q}\left[S_{\alpha_q} + \sum_{p=1}^{n} (\dot{m}_{pq} - \dot{m}_{qp})\right] \tag{3.3}$$

where ρ is the density of the mixture, $\mathbf{u}$ is the velocity vector, S_m is the global mass source term, p is the static pressure, μ is the dynamic viscosity of the mixture, $\mathbf{g}$ is the gravitational acceleration vector, $\mathbf{F}_\sigma$ is the surface tension force vector, α_q is the volume fraction of phase q, where $0 \leq \alpha_q \leq 1$, S_{α_q} is the source term for phase q, $\dot{m}_{pq}$ and $\dot{m}_{qp}$ are the mass transfer rates from phase p to phase q and from phase q to phase p, respectively [23], [24].

In this method, each cell is assigned a volume fraction for phase q, α_q, which can take any value between 0 and 1. A value of α_q = 0 indicates a cell filled entirely with the secondary phase, p, and α_q = 1 indicates a cell filled entirely with the primary phase, q, and intermediate values indicate a cell partially occupied by both. The diagram in Figure 3.2 shows, at the top the actual interface of the fluid passing through the cells with intermediate volume fractions, and at the bottom, shows how the VoF method reconstructs that same interface.

The interface tracking process follows three steps. Firstly, the model tracks the liquid volume fraction in each cell. Subsequently, the model reconstructs the interface geometry from the gradient of the volume fraction field, $\nabla\alpha$. The interface is assumed to be planar within each cell, positioned to satisfy the known volume fraction. Lastly, the interface is updated over time by solving the phase continuity equation.

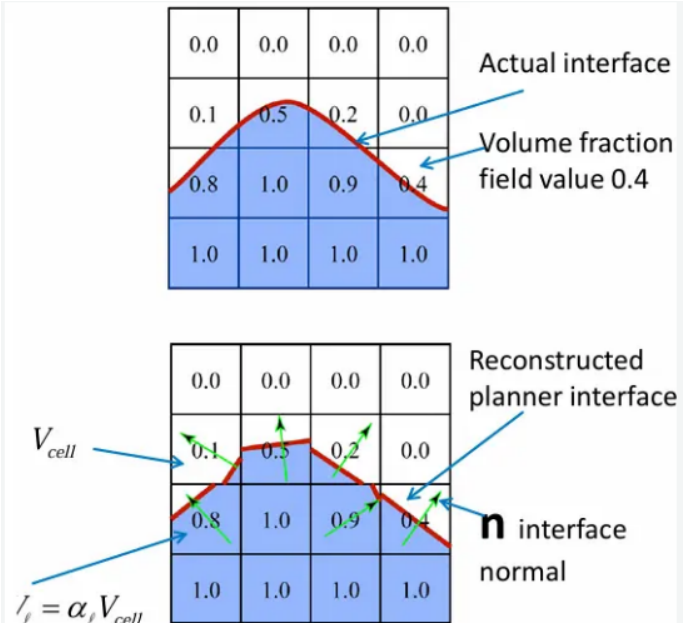

Figure 3.2: Interface tracking in VoF multiphase model [23].

3.3 Schnerr-Sauer Model Source Terms

In this section, the Schnerr-Sauer model, which was chosen for the pseudo-phase change transition, is presented. The role of the cavitation model during the simulation is to adjust the value of α throughout the domain by decreasing or increasing it, according to what is necessary. The regulation of this quantity is done through what are called the source terms of the model, which are characteristic of each cavitation model. These are responsible for quantifying how quickly mass is exchanged between the two defined phases. Considering the phases q and p as liquid, l, and gas, g, respectively, there is the vaporisation source term, R_v, responsible for controlling the liquid-to-gas transition, and a condensation source term, R_c, responsible for controlling the gas-to-liquid transition. The SS model source terms define the source term, S_{α_q}, through the relation $S_{\alpha_q} = R_c - R_v$. The condensation and vaporisation source terms, are given by,

$$R_c = 3C_c \frac{\rho_v \rho_l}{R_b \rho_m}(1-\alpha)\sqrt{\frac{2}{3}\frac{|p - p_{sat}(T)|}{\rho_l}} \tag{3.4}$$

$$R_v = 3C_v \frac{\rho_v \rho_l}{R_b \rho_m}\alpha(1+\alpha_{NUC}-\alpha)\sqrt{\frac{2}{3}\frac{|p - p_{sat}(T)|}{\rho_l}} \tag{3.5}$$

where R_c is the condensation rate, R_v is the vaporisation rate, C_c is the condensation constant, C_v is the vaporisation constant, ρ_v is the vapour density, ρ_l is the liquid density, ρ_m is the mixture density, R_b is the bubble radius, α is the liquid volume fraction, α_{NUC} is the nucleation site volume fraction, p is the local static pressure, and $p_{sat}(T)$ is the saturation pressure at the local temperature T. In the pseudo-phase change model this saturation pressure is actually representing the pressure at which the properties switch from the liquid-like side to the gas-like side.

According to the value of p relative to the local $p_{sat}(T)$, the bubble, that for this case is representing the gas-like phase, may increase or decrease its size. The source term R_c will be active and positive when $p > p_{sat}(T)$, driving "condensation", which in the pseudo-phase change model represents going from the gas-like side to the liquid-like side of the properties, crossing the Widom line, as there is not real condensation occuring. While, R_v will be active when $p < p_{sat}(T)$, driving "vaporisation", which in the pseudo-phase change model reflects as going grom the liquid-like to the gas-like side of the properties, hence crossing the Widom line. The coefficients C_c, for condensation, and C_v, for vaporisation, are the factors that allow to adjust independently the rate of condensation and vaporisation, respectively. In the pseudo-phase model this translates as the two factors that control the rate of changing between the liquid-like and gas-like phases.

3.4 k-ε Turbulence Model

For most engineering applications, when simulating a turbulent flow, it is unnecessary to resolve all the details of the turbulent fluctuations, as this substantially increases the computational time with little benefit. In most cases, information about the time-averaged properties of the flow is sufficient. For this reason, most simulations are based on the Reynolds-averaged Navier-Stokes equations, in which each quantity is decomposed into a mean and a fluctuating component, and the governing equations are then averaged in time. This transformation, however, introduces new unknown terms in the momentum equation, the Reynolds stresses. Since no equation is available to determine these terms, additional equations are required to close the system, which is the role played by the turbulence model [25].

The k-ε model is a two transport-equation linear eddy-viscosity turbulence model, which closes the system by introducing equations for the turbulent kinetic energy, k, and turbulent kinetic energy dissipation, ε. The model's equation for the turbulent kinetic energy is given by [26],

$$\frac{D}{Dt}(\rho k) = \nabla \cdot (\rho D_k \nabla k) + P - \rho \varepsilon \tag{3.6}$$

where k is the turbulent kinetic energy, D_k is the effective diffusivity for k, P is the turbulent kinetic energy production rate and ε is the turbulent kinetic energy dissipation rate.

The model's equation for the turbulent kinetic energy dissipation rate is given by [26],

$$\frac{D}{Dt}(\rho \varepsilon) = \nabla \cdot (\rho D_\varepsilon \nabla \varepsilon) + \frac{C_1 \varepsilon}{k}\left(P + C_3 \frac{2}{3} k \nabla \cdot \mathbf{u}\right) - C_2 \rho \frac{\varepsilon^2}{k} \tag{3.7}$$

where D_ε is the effective diffusivity for ε, C_1 and C_2 are model coefficients.

The turbulent viscosity, ν_t, is the quantity that then allows the Reynolds stresses to be determined, and it is obtained from k and ε through the following equation [26],

$$\nu_t = C_\mu \frac{k^2}{\varepsilon} \tag{3.8}$$

where ν_t is the turbulent viscosity, and C_μ is a model coefficient for the turbulent viscosity.

The initial conditions for the turbulent kinetic energy, k, and for its dissipation rate, ε, can be estimated from a turbulence intensity and a reference length scale, through the following equations [26],

$$k = \frac{3}{2}\left(I|\mathbf{u}_{ref}|\right)^2 \tag{3.9}$$

where I is the turbulence intensity and $\mathbf{u}_{ref}$ a reference flow speed,

$$\varepsilon = \frac{C_\mu^{0.75} k^{1.5}}{L} \tag{3.10}$$

where C_μ is a model coefficient and L a reference length scale.

3.5 Relevant Parameters for CFD

Some relevant parameters for the CFD simulation, which will later be referred to throughout the dissertation, are introduced in this section. Initially, the parameters most commonly adopted to assess the quality of a mesh are presented, followed by the definition of the dimensionless quantity, the Courant number.

3.5.1 Mesh Quality Parameters

In order to assess the quality of a mesh, there is a wide range of parameters that can be selected. For this study, the main parameters considered were the skewness, aspect ratio and non-orthogonality.

According to the ANSYS FLUENT User Guide [27], the skewness is defined as the difference between the shape of a cell and the shape of an equilateral cell of equivalent volume. Highly skewed cells are undesired as they can decrease accuracy and destabilise the solution. Therefore, the general recommended guideline is a maximum skewness for a triangular/tetrahedral mesh below 0.95, with an average value below 0.33.

Following the same guidelines, the ANSYS FLUENT User Guide defines the aspect ratio as a measure of the stretching of the cell. Usually, it is recommended to keep the values of the aspect ratio around 5 to 10 [27]. However, for elongated geometries, such as the case that is going to be presented, relatively high aspect ratios are considered acceptable, as the phenomena of interest occur close to the orifice region, with the inlet and outlet zones being less relevant. This use of high aspect ratios is generally acceptable in some situations, despite the general recommendations.

For instance, CFD Direct reports the case of an aerofoil in which a mesh with an aspect ratio of 1000 was used [28].

Lastly, non-orthogonality is the angle between the line connecting the centres of two neighbouring cells and the normal vector of the face between them, and it varies depending on the mesh generated. According to the OpenFOAM User Guide, non-orthogonality below 5º requires no correction, values up to 75º are handled well by the corrected scheme, above 75º, the limited scheme may be required for stability, and above 85º convergence is generally hard to achieve [29].

3.5.2 Courant Number

The Courant number, Co, is a dimensionless value that measures how many cells a fluid particle travels during a single time step within the computational domain, ensuring the correct propagation of information. The Courant number is defined as [30],

$$Co = \frac{u\Delta t}{\Delta x} \tag{3.11}$$

where u is the velocity of the fluid, Δt is the time step and Δx the spatial grid resolution, which is equivalent to the distance between the cell centres. Given the need for stability in the simulations of the present work, $Co < 1$ should be satisfied. In this way, information from one cell will reach the neighbour cell within one time step. Otherwise, information could reach a second or third neighbour cell within the same time step, which is undesirable for this case. In some cases, a higher Courant number is adopted to speed up computation time, but since the focus for this case is stability, that is not the chosen approach for this study.

3.6 Fundamentals of Flow Through an Orifice

Head-type flowmeters consist of a group of fluid flow measurement devices which include orifice plates, venturi tubes, weirs, flumes and others. They work by introducing changes in the velocity in the direction of the flow, generating a measurable differential pressure to keep the total energy balanced. The working principle of the head-type flowmeter devices is based on Bernoulli's theorem, which states that in a flowing stream, the sum of the pressure head, the velocity head and the elevation head at one point is equal to their sum at another point in the direction of the stream, plus the losses due to friction between the two points [31]. The majority of the flowmeters depend on a restriction in the flow stream to introduce these changes to the velocity. For these devices, when a circular orifice is placed in a circular pipe, the beta ratio, β, is used to define the ratio between the diameters of the restriction and the pipe [32].

This kind of restriction is the one utilised by the orifice plate, which introduces an increase in the flow velocity and a corresponding pressure drop with a circular restriction inserted in the pipe. This type of head flowmeter is the one that is most similar to the orifice geometry that is going to be adopted in this study. This is the underlying reason why ISO 5167-1 [32] for pressure differential devices and ISO 5167-2 [33] for sizing orifice plates will be used as a guideline to analyse

the results of the CFD model. It should be noted that these ISO standards were developed for geometries above the measurements considered for the domain of the CFD model. More precisely, the authors define the lower limit of the measurements as 50 mm for D and 12.5 mm for d. Nevertheless, after analysing several other options, the ISO 5167-1 and ISO 5167-2 documents were considered the most reliable sources of information available that were suitable for the geometry under study and were, therefore, considered the most adequate choice.

For the orifice plate geometry, Figures 3.3 and 3.4 illustrate the pressure profile and the flow pattern typical of this geometry. When the flow passes through the orifice, the imposed restriction causes an increase in velocity accompanied by a decrease in static pressure. The point of maximum velocity and minimum pressure occurs downstream of the restriction and is known as the vena contracta. Beyond this point, the velocity decreases, and the pressure recovers, although never returning to the value observed upstream, and this difference corresponds to the permanent pressure loss introduced by the orifice. This behaviour is also visible in the flow pattern, which shows the pathlines of the velocity contracting as the flow passes through the orifice and expanding again further downstream. Since the flow separates at the edges of the restriction, recirculation zones are formed adjacent to the walls immediately downstream of the orifice, and it is only after these zones that the flow reattaches and the pressure stabilises again.

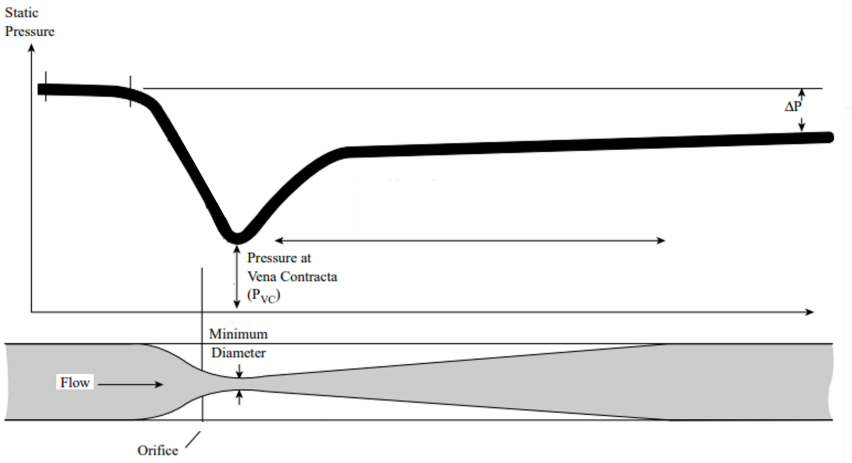

Figure 3.3: Static pressure distribution along an orifice plate, showing the position of the vena contracta [31].

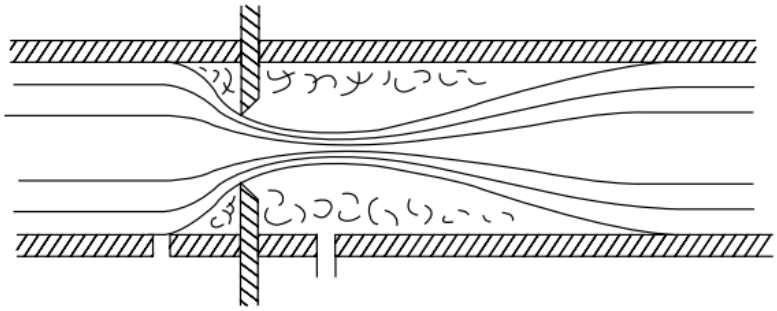

Figure 3.4: Flow pattern with an orifice plate [31].

3.6.1 Discharge Coefficient

In this section, the discharge coefficient, C_d, the parameter selected to assess the results, is presented. To evaluate whether the results obtained from a simulation were acceptable across the different simulations conducted, a parameter was required that would allow a direct comparison between cases. For the simulations of the present dissertation, the discharge coefficient, as defined by ISO 5167-1 for flow-restricting geometries, was selected.

The discharge coefficient is defined as the ratio between the actual mass flow rate and the ideal mass flow rate. It is mainly dependent on the geometric parameters, so under similar Reynolds numbers, fluid properties and pressure drops, it is expected to yield similar results. For this reason, it was chosen as the comparison parameter to first compare the water case with Case A. In the conditions tested for Case A, the fluid presents properties similar to those of water, which means that, using the same geometry, the discharge coefficient is expected to yield similar results. On this basis, the discharge coefficient can be used to assess whether the results remain reliable when switching from water to carbon dioxide.

For Cases B and C, the fluids are not as close to water as in Case A. The densities become further from that of water, the pressure drops tested are much higher than those tested for the water case, and the fluid presents a compressible behaviour. It is therefore expected that the discharge coefficients obtained will not be an exact match to that of water. Nevertheless, a substantially larger deviation would indicate that the results are not physically reasonable, and so this comparison allows an assessment of whether the results obtained are acceptable. If the discharge coefficient were to yield very different values, that would indicate a problem.

For these reasons, the discharge coefficient was selected as the primary parameter to assess the results, which were compared against the water case as a benchmark. According to the ISO 5167-1 [32] standards, for an orifice restricting geometry, the mass flow rate can be determined by the following equation [32],

$$\dot{m} = \frac{C_d}{\sqrt{1-\beta^4}}\,\varepsilon_{exp}\,\frac{\pi}{4}d^2\sqrt{2\Delta p\,\rho_1} \tag{3.12}$$

where $\dot{m}$ is the mass flowrate, C_d is the discharge coefficient, β is the diameter ratio, ε_{exp} is the expansibility or expansion factor, d is the orifice (throat) diameter, Δp is the differential pressure, and ρ_1 is the fluid density at the upstream tapping. This equation can be rewritten in order to the discharge coefficient, resulting in the following equation,

$$C_d = \frac{\dot{m}\sqrt{1-\beta^4}}{\varepsilon_{exp}\left(\frac{\pi}{4}\right) d^2 \sqrt{2\Delta p\, \rho_1}} \tag{3.13}$$

The expansion factor, ε_{exp}, presented in these equations is the coefficient used to take into account the compressibility of the fluid. When the fluid is considered incompressible, in the case of liquid, this coefficient takes the value of 1, whereas when the fluid's compressibility cannot be neglegible the expansibilty factor is given by [33],

$$\varepsilon_{exp} = 1 - \left(0.351 + 0.256\beta^4 + 0.93\beta^8\right)\left[1 - \left(\frac{p_2}{p_1}\right)^{1/\kappa}\right] \tag{3.14}$$

where p_1 and p_2 are the absolute static pressures at the upstream and downstream tappings respectively, and κ is the isentropic exponent of the fluid.

Chapter 4

H_2O Numerical Simulations: Methodology & Validation

This chapter presents an overall review of the methodology implemented in the present study and the methodology used for the development of the CFD model using water as the working fluid, which serves as the foundation for the subsequent CO_2 simulations. Figure 4.1 illustrates a diagram that presents all the phases of this project. Initially, the objectives of the dissertation were defined followed by a literature review. Subsequently the CFD model was developed using water as the working fluid. Following this, the model was implemented for Cases A, B and C adopting the necessary changes to the basis CFD model. The following section presents in detail the methodology implemented for the H_2O simulations.

4.1 Methodology of H_2O Simulations

As discussed in Chapter 1, the initial step towards the development of the CFD framework to be implemented for CO_2 across the thermodynamic regimes of interest consisted in recreating a model using water as the working fluid from the literature, and subsequently comparing the obtained results. The simulations were performed in OpenFOAM v13, a choice motivated by consistency with the previous work conducted at the institute and by the wide adoption of this software in the numerical studies reviewed in Chapter 2.

To validate the developed model, the first study presented in Section 2.2.2 was selected [20]. In this work, the authors performed simulations considering two working fluids, air and water, across a range of geometries and boundary conditions. For the present study, a single case using water as the working fluid was chosen, and the corresponding geometric parameters and boundary conditions were adopted from it.

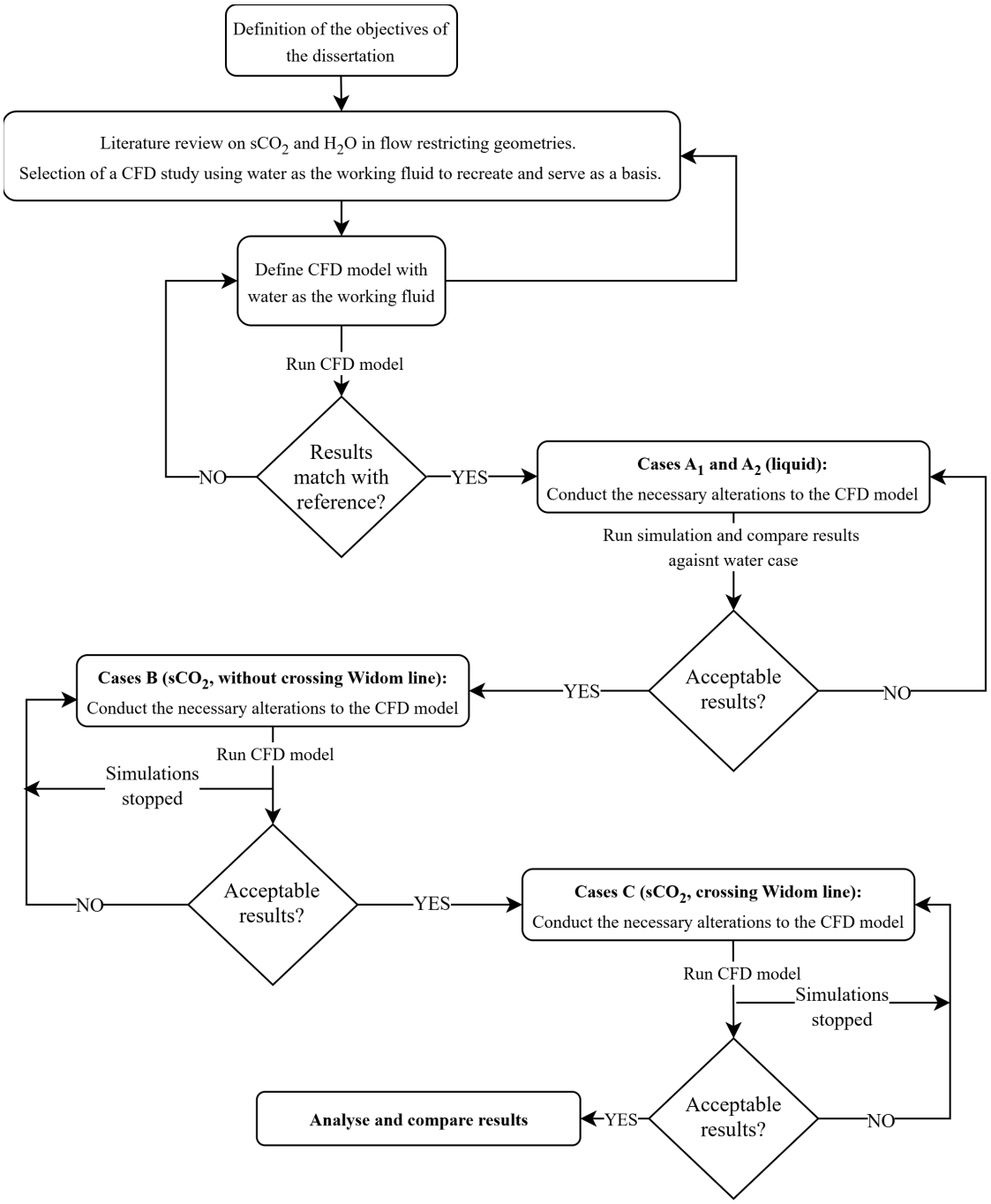

Figure 4.1: Diagram of the methodology of the dissertation.

4.1.1 Geometry

The reference study conducts its simulations using a three-dimensional geometry. However, the present work adopts a 2D axisymmetric representation of the 3D orifice, similar to the domain adopted by [8] in the circular orifice representation. This choice is motivated by the significantly lower computational effort associated with the two-dimensional geometry when compared to three-dimensional geometries, allowing computational time to be saved. However, it should be

noted that OpenFOAM does not have the ability to solve two-dimensional problems in cylindrical coordinates, as all terms of the Navier–Stokes equations within the solver are formulated in Cartesian coordinates. Consequently, the standard approach when using this software is to employ a pseudo-axisymmetric method for 2D axisymmetric problems [8], [29]. In this method, the computational domain is defined as a wedge, consisting of a sector of a small angle, θ, about the axis of the pipe, with the thickness of a single cell in the circumferential direction. The two lateral faces of this sector are assigned a wedge boundary condition, which allows the solver to reproduce the axisymmetric behaviour of the flow while all the equations remain formulated in Cartesian coordinates. Figures 4.2, 4.3 and 4.4 illustrate the resulting pseudo-axisymmetric geometry adopted in this study, similar to the one implemented by [8], illustrated in Figure 2.6. Figure 4.2 presents a side view of the domain, in which the lower edge corresponds to the axis of symmetry and the upper edge to the pipe wall, meaning that the domain extends over a radius, $D/2$, and not over a diameter. The inlet and the outlet are located at the left and right boundaries, respectively. Figure 4.3 presents the corresponding view along the axis, where the wedge angle, θ, is represented between the two lateral faces, which meet at the axis. Lastly, Figure 4.4 presents a detail of the orifice region to illustrate the final wedge geometry used in the simulations.

The geometry and mesh were developed using two OpenFOAM utilities: *blockMesh* and *extrudeMesh*. The first was utilised to develop the rectangular regions of the domain and the mesh, and the latter was employed to produce the triangular wedge section required by the pseudo-axisymmetric formulation. Table 4.1 summarises the parameters adopted for the geometry. The values of the upstream length, $L_{upstream}$, orifice thickness, e, total length, L_{total}, diameter ratio, β, outside diameter, D were taken from the reference study [20]. For the selected pipe diameter, D, of 12.3mm, and β, of 0.4065, the resulting orifice diameter, d, following the definition is approximately 5 mm. The value considered for the wedge angle, θ, represented in Figure 4.3, was of 5°, based on the studies [8] and [10].

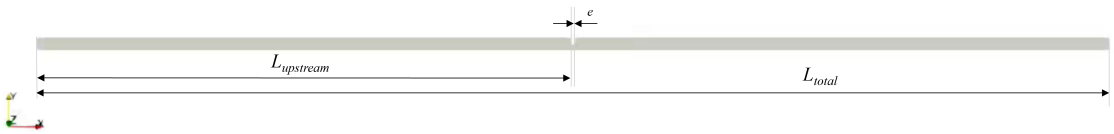

Figure 4.2: Side view of the pseudo-axisymmetric computational domain.

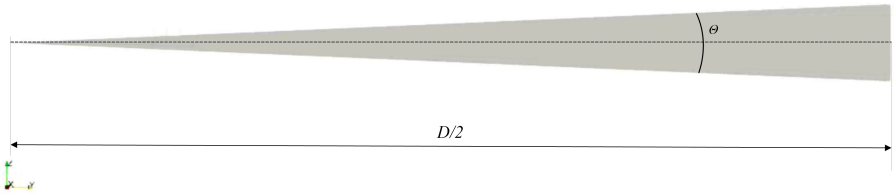

Figure 4.3: Cross-sectional view of the wedge-shaped domain.



Figure 4.4: Detail of the orifice region of the computational domain (side view).

Table 4.1: Geometric parameters of the geometry

Parameter	Value
$L_{upstream}$	246 mm
e	2 mm
L_{total}	494 mm
β	0.4065
D	12.3 mm
θ	5°

4.1.2 Numerical Solver

As discussed in Chapter 4, a two-phase modelling approach, denominated as the pseudo-phase change model, will be implemented in this work to overcome the numerical instabilities that arise when crossing the Widom line under supercritical conditions. The CFD model developed is designed to be applicable across all thermodynamic regimes of interest. Thus, the two-phase flow formulation will be applied to all the cases studied, however, only when required will the pseudo-phase change be activated, remaining single-phase elsewhere.

In order to implement the pseudo-phase change methodology, it is necessary to select a solver developed for two-phase flows. Therefore, the compressibleVoF solver presented in Section 3.2 was selected. The compressible version of the solver was chosen instead of the incompressible

version, as CO_2 presents compressible behaviour above the critical temperature and pressure. For the cases in which it is not necessary to activate the pseudo-phase change model, the liquid volume fraction, α, is set to 1 throughout the whole domain. Since the Widom line is not crossed during the simulations, the pseudo-phase change is not triggered and the simulation is solved as a single-phase flow.

The compressibleVoF solver is inherently transient, and the steady-state formulation is not available, however, the cases studied in the present work correspond to steady conditions. Therefore, the approach adopted was to run the simulations in time until the solution stabilised, taking the steady-state reached as a result. Considering this, the temporal discretisation was performed using a first-order implicit Euler scheme. For the convective terms, a second-order linear-upwind scheme was adopted for the momentum equation, while a first-order upwind scheme was used for the energy and turbulence equations. With the objective of maintaining the solution stable, the Courant number was kept below one so that the flow does not cross more than one cell per time step. Since $Co < 1$, only one outer loop was considered, meaning the PISO formulation was adopted. The systems were solved to tolerances of 10^{-4} for the pressure equation and 10^{-6} for the remaining equations.

4.1.3 Turbulence Model

Considering the literature review on the turbulence models commonly chosen for modelling sCO_2, presented in Section 2.2.1, the k-ε turbulence model was chosen. To solve the k-ε model equations, the default model coefficients were selected, which are presented in Table 4.2, where σ_k and σ_ε are the parameters used to obtain the effective diffusivities D_k and D_ε. Additionally, a turbulent intensity of 5% was specified for the turbulent kinetic energy, and a mixing length of 0.005 m for the turbulent kinetic energy dissipation rate, for both the boundary and initial conditions.

Table 4.2: k-ε turbulence model default coefficients [26]

Coefficient	Value
C_μ	0.09
C_1	1.44
C_2	1.92
C_3	0.00
σ_k	1.00
σ_ε	1.30

4.1.4 Boundary Conditions

The boundary conditions for the water case were defined in accordance with the reference study selected [20]. At the inlet, a temperature of 300 K and a uniform velocity of 0.755 m/s were imposed, meaning the mass flow rate for the simulation is defined by the boundary conditions. At the outlet, a pressure of 10^5 Pa is imposed. Since the quantities being defined are the inlet velocity and the outlet pressure, the quantity obtained is the inlet pressure. The reference study presented a

wide range of thermodynamic regimes tested, however it did not present the results for all of them. Considering this, for the reproduction of the study the case selected was the one that presented the post-processing information.At the wall, the no-slip condition was applied, and it was defined as adiabatic.

Table 4.3: Boundary conditions for the water case

Boundary	U **(m/s)**	p **(Pa)**	T **(K)**
Inlet	0.755	Calculated	300
Outlet	Calculated	10^5	Calculated
Wall	No-slip	Calculated	Adiabatic

4.1.5 Convergence Criteria

As previously stated, the simulations were advanced in time until the solution stabilised, with the steady-state reached being taken as the result. Considering this, although the residuals were monitored throughout all the simulations conducted, to confirm that the solution remained stable and no abnormality was reported, they were not considered as the convergence criterion. Unlike a steady-state formulation, in which the simulation is terminated once the residuals fall below a specified level, a transient simulation advances until the prescribed end time, and the assessment of whether a steady-state cannot be done through the monitoring of the residuals alone. The standard and recommended selected convergence criteria for a steady-state simulation run under transient conditions is the monitoring of a physical quantity, depending on what was defined as the boundary conditions.

In the case of water presented below, the physical quantity monitored was the pressure at the D tapping location, which progressively evolved towards a constant value. The pressure solution was checked at intervals of 0.1 s, and the solution was considered to have reached steady-state once the variation between successive readings remained below 0.1%, after which the simulation was terminated.

4.2 Mesh Independence Study

Subsequently, once the complete case had been established, a mesh independence study was conducted to determine the optimal cell division for the domain. The underlying principle of this study is that beyond a certain level of cell division, the results of the simulation become insensitive to further refinement of the mesh, and therefore increasing cell count no longer meaningfully affects the results, and the solution can be considered mesh-independent. Identifying this limit allows us to select a mesh that produces accurate results at the minimum possible computational cost.

The mesh independence study was carried out for the CFD model using water as the working fluid, employing nine meshes of increasing cell count, ranging from 563 to 52644 cells, looking to keep to proportionality of the cell distribution. Figure 4.5 shows an example of one of the meshes

used in this study, illustrating the general cell structure and distribution within the domain. The more refined zones were the orifice, and close downstream and upstream of the orifice, where the most relevant gradients take place. For the mesh of a 2D pseudo-axisymmetric geometry in the 3D spatial domain, one cell should be set in the third dimension. All simulations were performed under identical conditions, with the cell division being the only variable parameter.

While carrying out the mesh independence study, it is also important to check and analyse the quality of the meshes generated. Table 4.4 summarises the obtained values for the parameters that were chosen to analyse, which were obtained using the utility *checkMesh* available in OpenFOAM. As introduced in Section 3.5.1 these consist of skewness, non-orthogonality quality, and aspect ratio. The maximum skewness reported remained constant at 0.3308 across all the meshes used, as a consequence of the proportional refinement strategy adopted. According to what was mentioned in Section 3.5.1, the maximum skewness should be kept below 0.95, and thus the values obtained respect the recommended limit. Non-orthogonality was zero, for both the maximum and average values, in every mesh, which was expected given the structured, axis-aligned nature of the mesh. Lastly, the maximum aspect ratio remained consistent, with slight changes within the range of 182.6 and 187.26. These relatively high values result from the elongated geometry of the domain, as the cells are stretched in the streamflow direction, where flow gradients are not so pronounced, while the cross-section of the pipe, where the steepest gradients occur, is resolved by the short cell dimension. Overall, it can be considered that the mesh quality was verified and maintained across all levels of refinement tested.

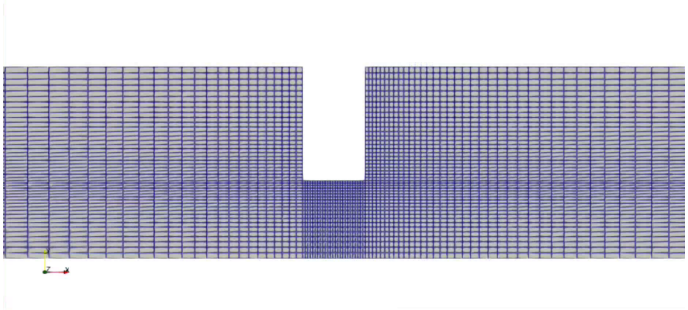

Figure 4.5: Example of mesh structure near the orifice for 8375 cells.

Table 4.4: Mesh quality parameters for the nine meshes used in the mesh independence study

Cells	Max Aspect Ratio	Max Skewness	Non-Orthogonality (Max/Avg)
563	183.76	0.3308	0 / 0
2034	186.99	0.3308	0 / 0
4739	184.95	0.3308	0 / 0
8375	183.93	0.3308	0 / 0
13169	187.26	0.3308	0 / 0
18956	184.54	0.3308	0 / 0
25793	182.63	0.3308	0 / 0
32500	183.62	0.3308	0 / 0
52644	183.08	0.3308	0 / 0

In order to assess mesh convergence, it is necessary to select parameters that allow the changes in the results to be analysed as the cell division of the domain increases. For this study, the pressure drop across the orifice and the velocity profile at three different locations were selected. To evaluate the pressure drop, the D and $D/2$ tapping locations measured upstream and downstream, respectively, from the upstream face of the orifice were selected in accordance with ISO 5167-2 recommendations for orifice plates [33]. Figure 4.6 illustrates the pressure measurement locations.

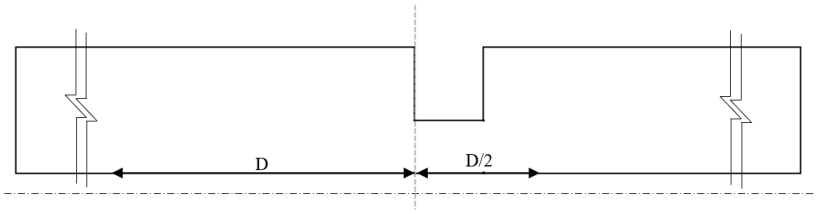

Figure 4.6: Scheme of D and $D/2$ tappings (not to scale).

For the velocity profiles, the distances selected for analysis were 0.2 m, 0.25 m and 0.3 m from the inlet patch, corresponding to 47 mm upstream from the middle of the orifice and 3 mm and 53 mm downstream from the middle of the orifice, respectively. These locations are identified by (a), (b) and (c), respectively, in Figure 4.7. At each location, the velocity profile is obtained by taking the value of the axial velocity component along the radial direction, from the axis of symmetry to the wall, as indicated by the arrow in Figure 4.7.

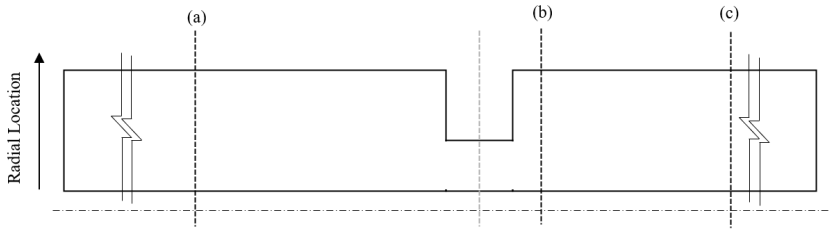

Figure 4.7: Scheme of the locations of the velocity profiles (not to scale).

The pressure drop results obtained for each mesh are summarised in Table 4.5 and represented in Figure 4.8. As the number of cells increased, the differential pressure measured between the D and $D/2$ tappings decreased, from a Δp of 21.6 kPa on the coarsest mesh to 17.7 kPa on the finest. The relative deviation reported in Table 4.5 was obtained by the difference obtained in the mesh more refined relative to the previous one. The rate of change of pressure drop measured across the orifice diminished as the level of refinement increased. A deviation of 5% between the first two meshes was obtained, the highest value reported. Beyond 18956 cells, all variations obtained are below 1.5%, reaching the smallest deviation between the two finest meshes, which was 0.04%, indicating that the solution has reached its asymptotic value. However, as the number of cells increased, the computational time required also increased, becoming significant beyond 18956 cells.

Table 4.5: Pressure drop measured across the orifice between the D and $D/2$ tappings

Number of Cells	Δp **(kPa)**	**Relative Deviation (%)**
563	21.6	—
2034	20.5	5.09
4739	19.5	4.81
8375	18.9	3.15
13169	18.6	2.01
18956	18.3	1.58
25793	18.0	1.37
32500	17.7	1.47
52644	17.7	0.04

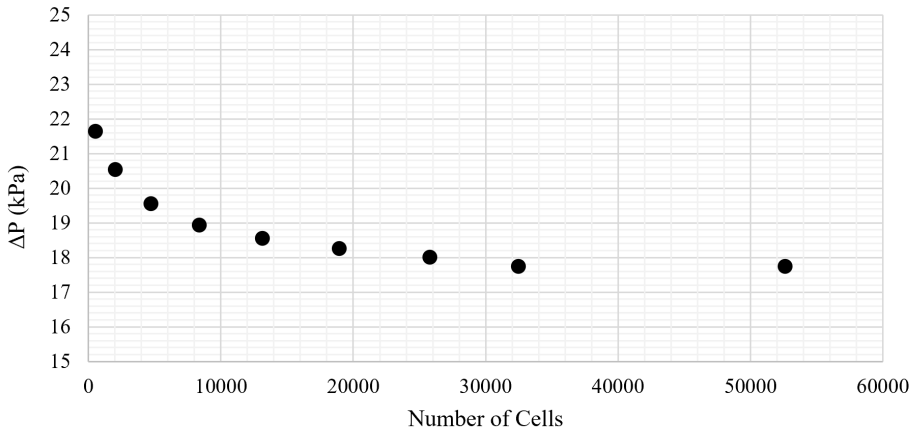

Figure 4.8: Pressure drop measured across the orifice, for D and $D/2$ tappings.

The plots in Figures 4.9, 4.10 and 4.11 illustrate the velocity profiles at 47 mm upstream, 3 mm downstream and 53 mm downstream from the middle of the orifice, respectively. The analysis of these profiles shows that, as the number of cells increases, the profiles progressively converge, with the curves for the finest meshes eventually overlapping at all three locations, at a faster rate than the pressure drop results. Starting from the mesh with 13169 cells, the profiles exhibit minimal variation, which becomes negligible beyond 18956 cells. The largest deviation between the velocity profiles of the different meshes occurs at 53 mm downstream, as can be seen in Figure 4.11. On the contrary, Figure 4.10, shows the smallest deviation within the profiles for the different refinement levels.

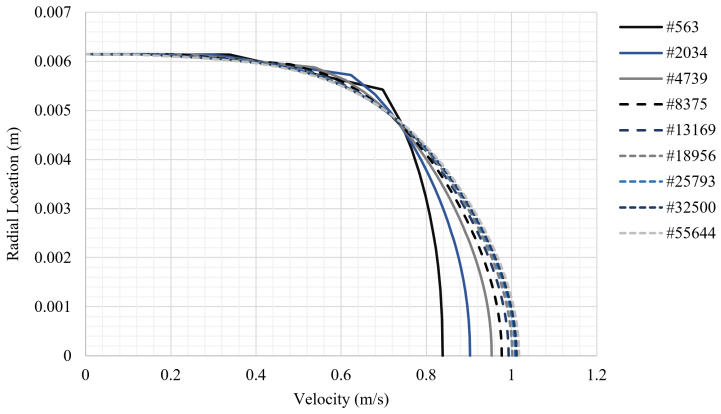

Figure 4.9: Velocity profile 47 mm upstream from the middle of the orifice (a).

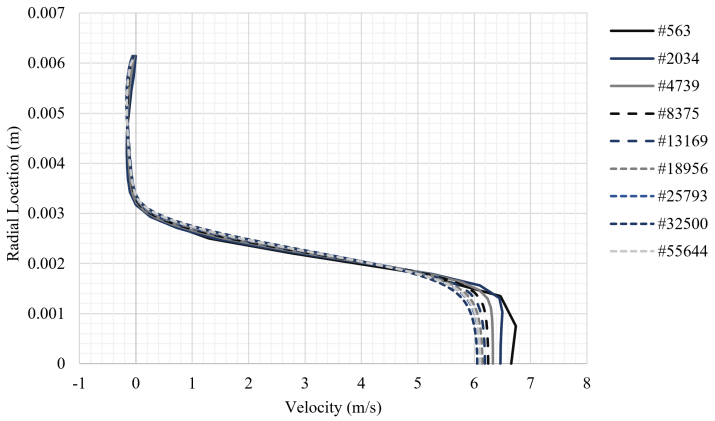

Figure 4.10: Velocity profile 3 mm downstream from the middle of the orifice (b).

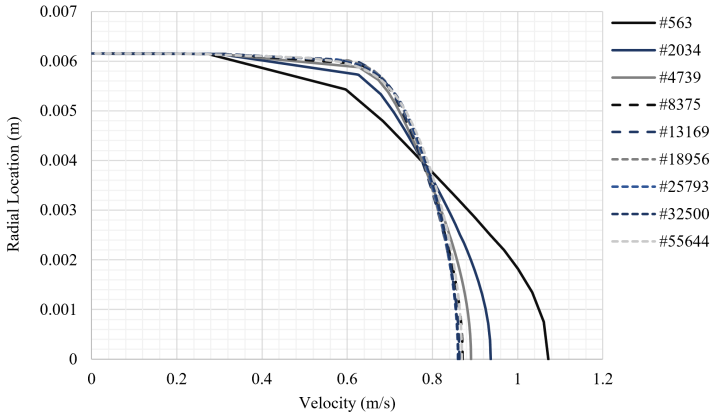

Figure 4.11: Velocity profile 53 mm downstream from the middle of the orifice (c).

Considering the pressure drop measured across the orifice, the velocity profile results, and the computational effort, the mesh of 25793 cells was selected for the CFD model. From the simulations conducted, as mentioned previously, the computational time starting from the mesh of 18956 cells became more significant. Considering that the velocity profiles become mesh-independent at approximately 18956 cells, and the pressure results only differ by 1.47% between the 25793-cell mesh and 32500-cell mesh, it was considered that the deviation between the results of these two meshes did not justify the increase in computational time, which was notorious. Therefore, the selection of the 25793-cell mesh allowed for the best compromise between accuracy and computational effort. Subsequently to the mesh independence study, the results from the selected mesh were compared against the CFD data from the reference study selected to recreate [20].

4.2.1 Comparison of Results Against Reference Study

As discussed in Chapter 1, the motivation for recreating the CFD model from the reference study was to have a reliable basis for the subsequent simulations. Therefore, it is necessary to compare the results obtained against those of the CFD from the selected paper. In the reference study [20], however, the precise location of the points selected for the pressure in the CFD data were not clearly specified, making it infeasible to extract pressure drop data for direct comparison. Therefore, the velocity profiles were selected as the basis for comparison, as these are explicitly reported in the reference study. To obtain the points of the CFD data from the literature to compare against the results presented in Section 4.2, the website WebPlotDigitizer was utilised. As the extraction of the points is done manually by the user, it is necessary to take into consideration the inherent error in extracting these plots with this methodology.

Figures 4.12, 4.13, and 4.14 present a comparison between the velocity profiles obtained in the present CFD simulations and those reported in [20], at three different axial locations, 47 mm upstream, and 3 mm and 53 mm downstream of the middle of the orifice, respectively.

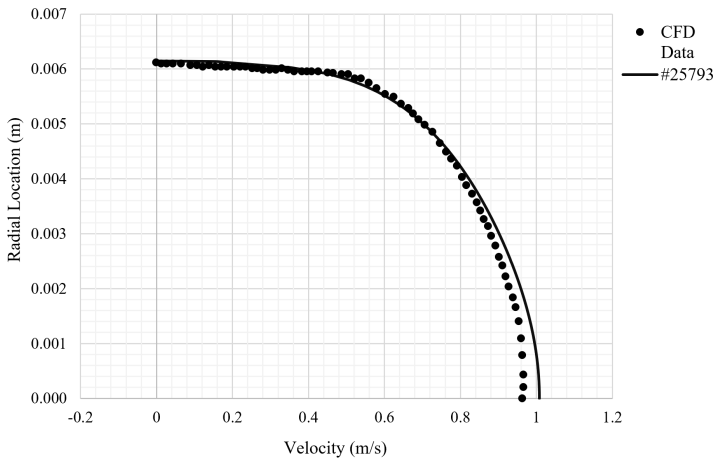

Figure 4.12: Comparison of velocity profiles at 47mm upstream.

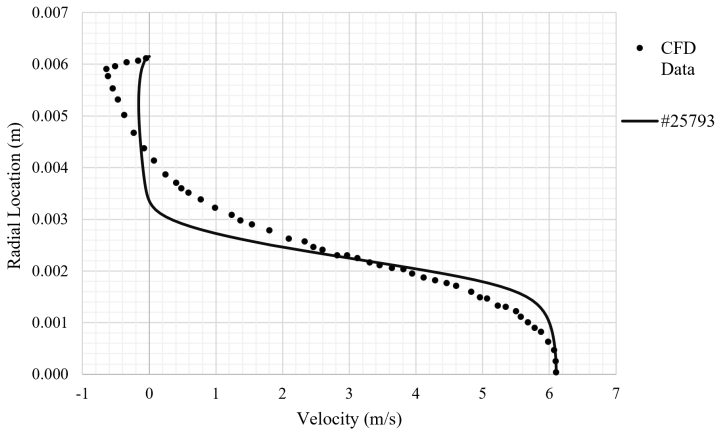

Figure 4.13: Comparison of velocity profiles at 3mm downstream.

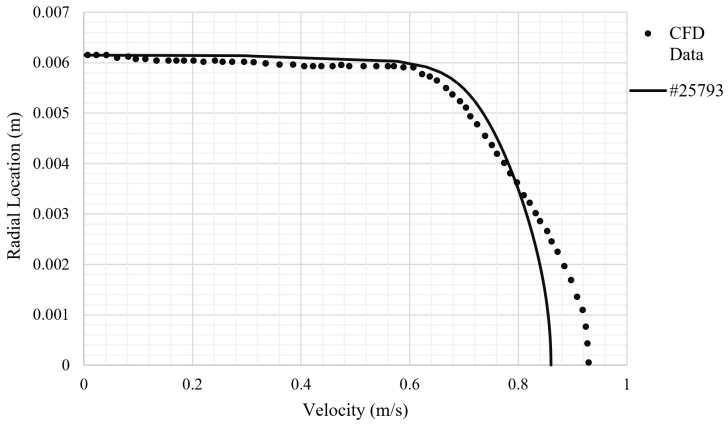

Figure 4.14: Comparison of velocity profiles at 53mm downstream.

The results show good agreement at 47 mm upstream of the middle of the orifice, as can be seen in Figure 4.12, where the flow is fully developed. Immediately downstream of the orifice at 3 mm, a more pronounced discrepancy is noted, as shown in Figure 4.13. Since this zone is right after the orifice, where the velocity gradients are steeper, and as some modelling settings may not be in accordance with the reference study, since there is no information on all the parameters, it is expected that some discrepancies may arise. Further downstream at 53 mm from the middle of the orifice, as can be seen in Figure 4.14, agreement with the reference results improves again as the flow recovers. Thus, it can be noted that the present model correctly reproduces the expected qualitative features of the flow at all three locations, namely the fully developed upstream profile, the jet and recirculation downstream of the orifice, and the subsequent recovery further downstream, despite the local discrepancies noted. It is important to highlight that the reference data originated from a CFD study, and as such, exact numerical agreement cannot be expected. Moreover, since

the reference results are also CFD data, these are subject to considerations made by the authors and may not be regarded as an absolute representation of the physical flow.

Additionally, the velocity contour and vectors between the obtained results and the reference data were compared. Figures 4.15 and 4.16 illustrate the velocity contour and vectors, respectively, for an inlet velocity of 0.755 m/s. Figure 4.17, taken from the reference study, shows the corresponding velocity contour and vectors obtained by the authors.

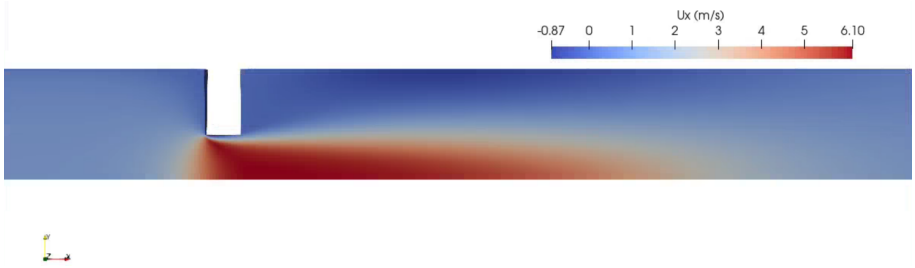

Figure 4.15: Velocity contour of water case for U_{inlet} of 0.755 m/s.

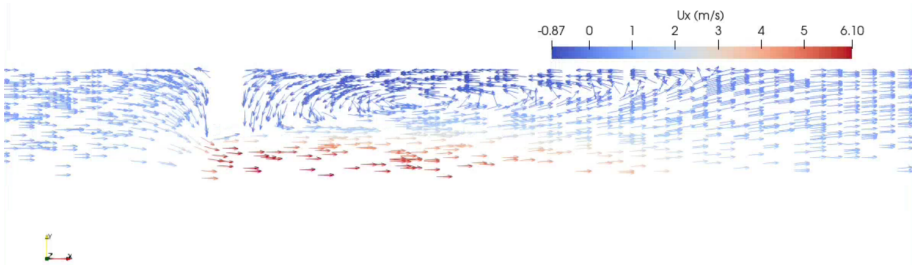

Figure 4.16: Velocity vectors of water case for U_{inlet} of 0.755 m/s.

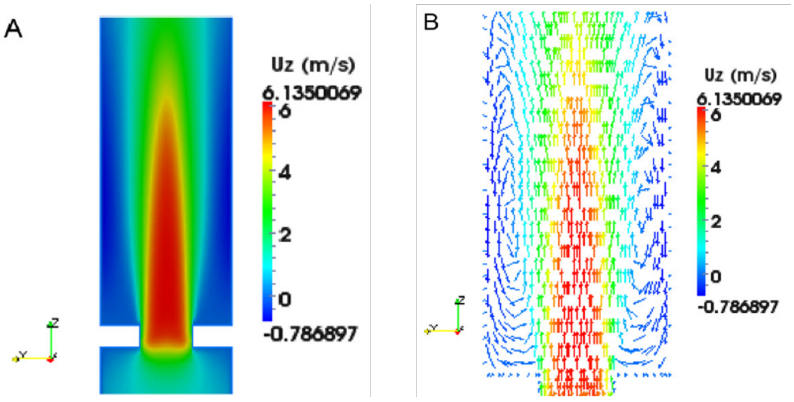

Figure 4.17: (A) Velocity contour and (B) velocity vectors obtained by the reference study [20].

Analysing Figure 4.15, it can be seen that the flow accelerates sharply through the restriction, increasing from the inlet velocity of 0.755 m/s up to a maximum of approximately 6.1 m/s, forming a jet. As discussed in Section 3.6, this is the expected behaviour of a flow through a restriction geometry. Figure 4.16 illustrates the same phenomenon of acceleration of the flow through the restriction, and additionally shows the reversed flow near the wall downstream of the orifice in

accordance with the recirculation region described in Section 3.6. Comparing these profiles against those illustrated in Figure 4.17, the flow fields exhibit similar profiles, with the jet forming at the beginning of the restriction and a singular recirculation zone close to the wall downstream of the orifice. The maximum velocity obtained, approximately 6.1 m/s, deviates only slightly from the value of 6.135 m/s reported in the reference study.

4.2.2 Results of the Water Case

Following the comparison of the results obtained with the CFD model developed, the obtained results for the water case were further post-processed and analysed. For the boundary conditions mentioned previously, an inlet velocity of 0.755 m/s and ambient outlet pressure, the mass flow rate was obtained using the data from the inlet patch. Additionally, considering the measured pressure drop between the D and $D/2$ tappings, the discharge coefficient was determined using Equation 3.13 presented in Section 3.6.1, to serve as a benchmark value for the following simulations with CO_2 as the working fluid. In order to ensure a reliable discharge coefficient, two additional simulations were run, maintaining all simulation settings identical and altering only the inlet velocity to 0.5 m/s and 1 m/s. The same post-processing procedure applied to the first simulation was applied to these two cases. Table 4.6 summarises the conditions and results for all three cases. From the C_d values obtained, an average of 0.748 was obtained, which will serve as the benchmark for comparison with CO_2 simulation results.

Table 4.6: Post-processing results of the water case

U **(m/s)**	Δp **(kPa)**	$\dot{m}$ **(kg/s)**	C_d **(-)**	**Deviation (%)**
0.500	7.79	0.0591	0.754	+0.85
0.755	18.25	0.0893	0.744	−0.49
1.000	31.87	0.1183	0.745	−0.36
Average	—	—	0.748	—

Figures 4.18 and 4.19 illustrate, for an inlet velocity of 0.755 m/s, the pressure contour of the whole domain, and the static pressure values along the axis of symmetry of the geometry, respectively. The pressure field shows the expected pressure drop across the orifice. Although in the pressure contour of Figure 4.18 the lowest pressure, of approximately 84.2 kPa, is captured at the sharp upstream edge of the restriction, as a result of the strong streamline curvature around the sharp 90° corner, Figure 4.19 reveals that the flow follows the classical evolution described in Section 3.6, which is a gradual pressure decrease upstream, followed by an accelerated drop beginning a few millimetres before the restriction, reaching a minimum of approximately 97.1 kPa at the vena contracta, located approximately 5 mm downstream of the plate, and followed by a partial pressure recovery. Regarding the temperature field, Figure 4.20 shows that the temperature remains essentially uniform, with variations of the order of millikelvins, following the pattern of the velocity contour shown in Figure 4.15. This is the expected result for water, since the flow

is effectively incompressible. For the remaining water simulations, the velocity, pressure and temperature profiles are presented in Annex A.1.

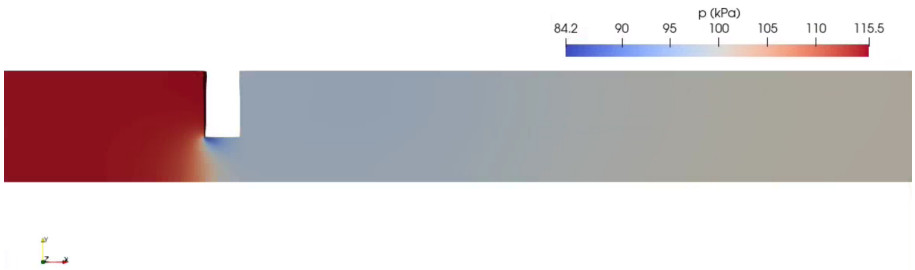

Figure 4.18: Pressure contour of water case for U_{inlet} of 0.755 m/s.

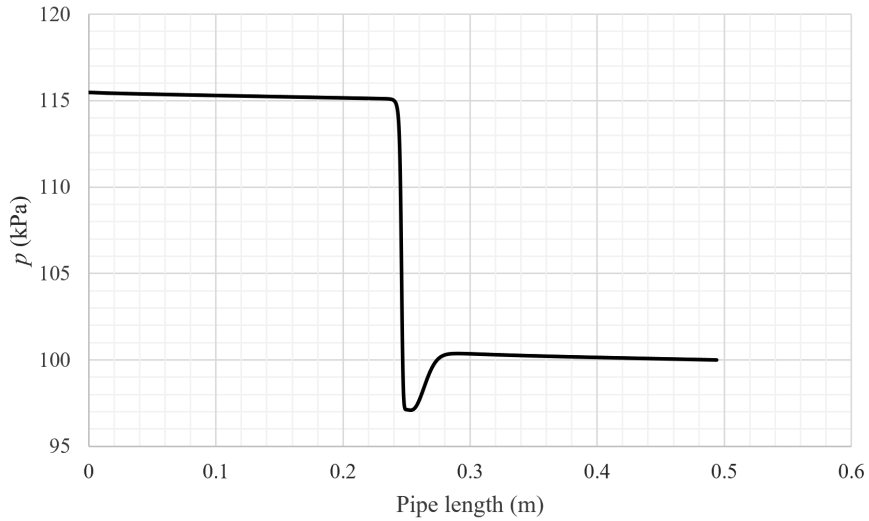

Figure 4.19: Pressure along the axis of symmetry of water case for U_{inlet} of 0.755 m/s.

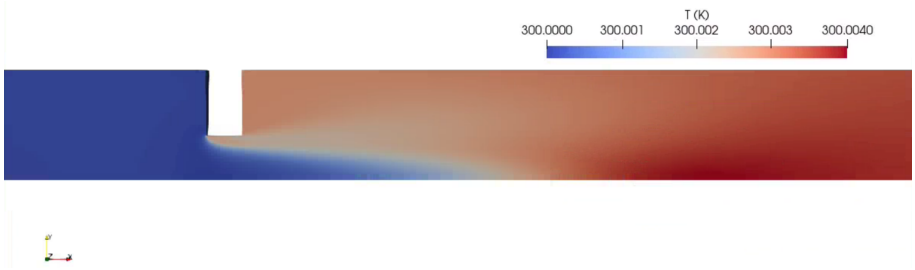

Figure 4.20: Temperature contour of water case for U_{inlet} of 0.755 m/s.

.

Chapter 5

CO_2 Numerical Simulations

In this section, the results obtained from the numerical simulations using carbon dioxide as a working fluid are presented. Initially, an overview of all the thermodynamic regimes that will be modelled are presented. Subsequently, the cases are detailed, along with their specific boundary conditions, the alterations conducted to the CFD model, and the results obtained.

5.1 Thermodynamic Regimes

To investigate the behaviour of carbon dioxide in an orifice geometry, a series of thermodynamic regimes were selected, spanning a broad range of temperatures and pressures, including the liquid subcritical, liquid supercritical, and supercritical regions. Figure 5.1 presents the simulation matrix on a p-T diagram, providing a visual representation of the thermodynamic conditions with respect to the CO_2 critical point and the Widom line.

The first case presented, Case A, consists of CO_2 in the liquid state and is divided into Cases A_1 and A_2. In Case A_1, the liquid CO_2 is below the critical temperature and pressure, whereas in Case A_2, the liquid CO_2 is below the critical temperature and above the critical pressure. Subsequently, Case B is presented, which simulates sCO_2, far from the critical point and not crossing the Widom line. Hence, although this point is situated at supercritical conditions, which requires attention due to the significant gradients, the pseudo-phase change model is not yet required, and thus the approach of setting α to 1 across all domain is applied. Lastly, Case C is presented, which seeks to simulate sCO_2 closer to the critical point and crossing the Widom line. Therefore, for this last case, the use of the pseudo-phase change model is required. Table 5.1 summarises all the boundary conditions for all the modelled cases.

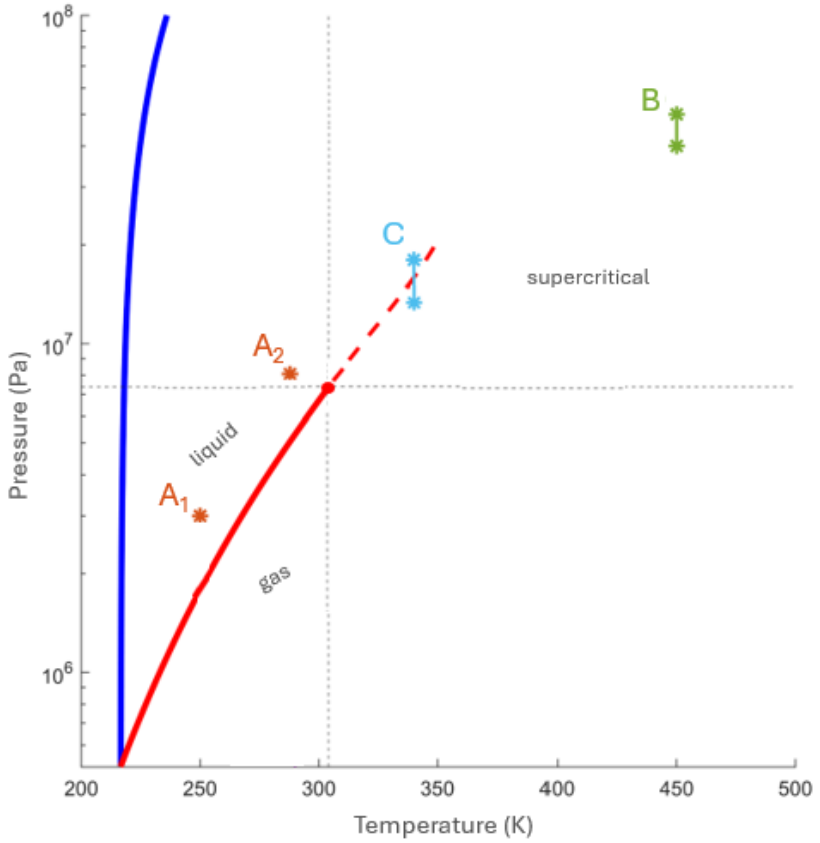

Figure 5.1: Representations of the cases simulated in the CO_2 p-T diagram.

Table 5.1: Boundary conditions of the cases simulated

Case	**Type**	T_{inlet} **(K)**	P_{inlet} **(bar)**	p_{outlet} **(bar)**	U_{inlet} **(m/s)**
A_1	LCO_2-LCO_2	250	-	27	0.5/ 0.755/ 1
A_2	LCO_2-LCO_2	280	-	81	0.5/ 0.755/ 1
B	sCO_2-sCO_2	450	500	490 – 380	–
C	sCO_2-sCO_2	340	180	170 – 140	–

5.2 Case A - Liquid CO_2

In this section, simulations were conducted using the developed CFD model with liquid CO_2 as the working fluid, corresponding to thermodynamic conditions within the subcritical domain. Two different cases were analysed, one far from the critical point, denominated Case A_1, and Case A_2, closer to it, while still remaining within the liquid domain.

As discussed previously, the idea behind conducting simulations under these conditions is to assess whether the developed model using water as a working fluid yields reasonable results when switching to CO_2, before entering thermodynamic regimes which are more challenging from the

numerical point of view. Therefore, to analyse Cases A_1 and A_2, it was defined that the inputs to the simulations would be the same as those of the water case, namely the inlet velocity, outlet pressure and inlet temperature. For each case the discharge coefficient was determined, which is expected to be the similar to that of the water, as explained in Section 3.6.1. Additionally, the velocity contours were analysed, and are expected to be similar to those of the water case, as the density of CO_2 under these conditions is similar to that of water.

As indicated in Table 5.1, for Case A_1, the inlet velocity was maintained at 0.755 m/s, the outlet pressure was set to 27 bar, and the temperature to 250 K. In the case A_2, closer to the critical point, the inlet velocity was also maintained at 0.755 m/s, however the outlet pressure was raised to 81 bar, above the critical pressure, and the temperature raised to 280 K, below the critical pressure. Similar to the case of the water, two additional simulations were conducted, for both Cases A_1 and A_2, maintaining all the parameters except for the inlet velocity which was set to 0.5 m/s and 1 m/s.

Contrary to what was done in the water case, where the fluid's thermophysical properties were retrieved directly from OpenFOAM's built-in property library, the properties of carbon dioxide were provided through an external tabulated property files. These files define the thermophysical properties of the fluid within the imposed range, including the density, specific heats, sensible enthalpy, sensible internal energy, dynamic viscosity, and thermal conductivity. These lookup tables were generated using a MATLAB code developed at the von Karman Institute, which retrieves the properties from the CoolProp library.

5.2.1 Case A_1 Results

In this section the results for the Case A_1 are presented. Table 5.2 summarises the inlet and outlet conditions of each simulation conducted.

Table 5.2: Inlet and outlet conditions for the CO_2 simulations of Case A_1

U_{inlet} **(m/s)**	p_{inlet} **(bar)**	T_{inlet} **(K)**	ρ_{inlet} **(kg/m^3)**	p_{outlet} **(bar)**	T_{outlet} **(K)**	ρ_{outlet} **(kg/m^3)**
0.500	27.07	250.0	1049.9	27.00	250.0	1049.8
0.755	27.16	250.0	1049.8	27.00	250.0	1049.9
1.000	27.28	250.0	1049.9	27.00	250.0	1049.9

Table 5.3 presents the obtained results, including the measured pressure drop for the D and $D/2$ tappings, as well as the pressure, temperature and density for the D tapping location. The conditions at this location are reported because the density there, corresponding to the upstream location of the pressure measurement, is the one used to determine the discharge coefficient. Additionally, the mass flow rate, computed from the inlet conditions, and the resulting discharge coefficient are reported. Since the fluid is in liquid subcritical conditions, the fluid presents an incompressible behaviour, and therefore in order to determine the discharge coefficient the Equation 3.13, presented in the Section 3.6.1, was used, considering an expansion factor, ε_{exp}, of 1.

Table 5.3: Post-processing results of Case A_1

U_{inlet} (m/s)	$\Delta p_{D\&D/2}$ (bar)	T_1 (K)	p_1 (bar)	ρ_1 (kg/m^3)	$\dot{m}$ (kg/s)	C_d (-)	Deviation (%)
0.500	0.09	250.0	27.07	1049.8	0.062	0.737	+0.56
0.755	0.20	250.0	27.16	1049.9	0.094	0.731	−0.27
1.000	0.35	250.0	27.28	1049.9	0.125	0.731	−0.29
Average	—	—	—	—	—	0.733	−2.01

Analysing the results obtained, they show that increasing the inlet velocity, and thus the imposed mass flow rate, leads to a corresponding increase in the pressure drop across the orifice. The pressure and temperature conditions measured at the D tapping location are similar to those at the inlet patch across all points tested, resulting in similar densities. The average C_d obtained was 0.733, with a maximum deviation between the individual points of +0.56%, at an inlet velocity of 0.5 m/s. Comparing the average discharge coefficient to the benchmark value of 0.748, determined in the water case, the resulting deviation is -2.01%.

Figures 5.2 and 5.3 illustrate the velocity contour and vectors in the vicinity of the orifice for Case A_1, with an inlet velocity of 0.755 m/s. Figures 5.4 and 5.5 show the pressure and temperature contours for the same conditions.

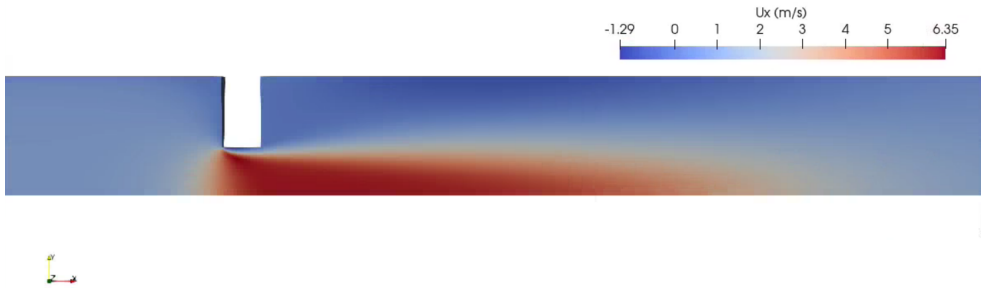

Figure 5.2: Velocity contour of Case A_1 for U_{inlet} of 0.755 m/s.

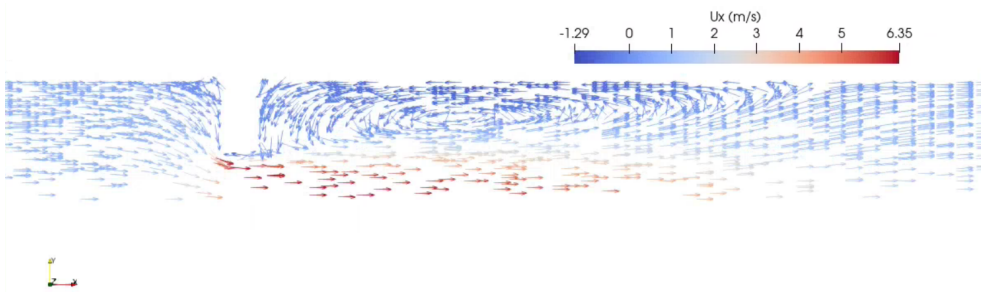

Figure 5.3: Velocity vectors of Case A_1 for U_{inlet} of 0.755 m/s.

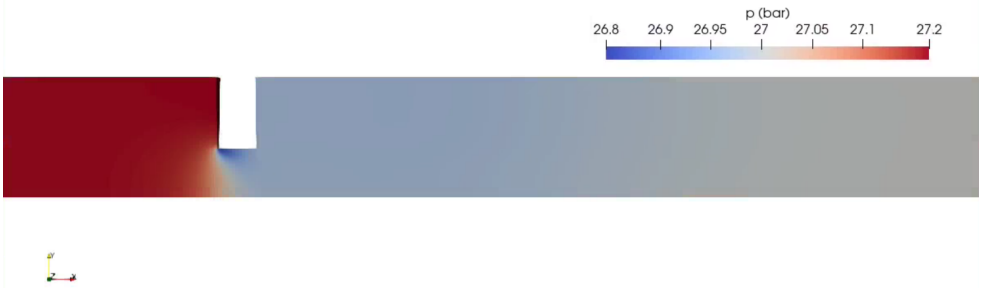

Figure 5.4: Pressure contour of Case A_1 for U_{inlet} of 0.755 m/s.



Figure 5.5: Temperature contour of Case A_1 for U_{inlet} of 0.755 m/s.

Analysing the velocity contour in Figure 5.2, the acceleration of the flow stream can be noted, from the inlet velocity of 0.755 m/s up to a maximum of 6.35 m/s, creating a jet. The velocity vectors, in Figure 5.3, capture the same phenomenon and additionally show the occurrence of recirculation downstream of the orifice. Both the jet and the recirculation pattern are essentially identical to those observed in the water case, with the maximum velocity increasing slightly from 6.10 m/s to 6.35 m/s. This behaviour is in line with what was predicted, since the properties of liquid CO_2 under these conditions are similar, but not identical, to those of water, it was expected to obtain similar velocity profiles with small deviations. The pressure contour, in Figure 5.4, shows a clear pressure decrease across the orifice, which is later partially recovered, without, however, returning to the upstream values due to losses. Similar to what was reported in the discussion of the water case results, the lowest pressure point is not reported after the orifice but rather in the orifice section, where there is a localised pressure drop, as discussed in Section 4.2.2. The temperature profile, described in Figure 5.5, illustrates a uniform temperature distribution, with slight variations of around 0.03 K that follow the same pattern as the velocity profile presented in Figure 5.2, similar to what was observed in the water case. The velocity, pressure and temperature contours, and velocity vectors for the other two simulations carried out are presented in Annex A.2.

5.2.2 Case A_2 Results

In this section, the results obtained for the working conditions of Case A_2 are presented. As mentioned previously, the idea behind modelling this case is to analyse the behaviour closer to

the critical point, while remaining below the supercritical zone, which is given over critical temperature and pressure. The thermophysical regime selected for this case sits above the critical pressure and below the critical temperature, falling in the designated supercritical liquid. Table 5.4 summarises the inlet and outlet conditions.

Table 5.4: Inlet and outlet conditions for the CO_2 simulations of Case A_2

U_{inlet} **(m/s)**	p_{inlet} **(bar)**	T_{inlet} **(K)**	ρ_{inlet} **(kg/m^3)**	p_{outlet} **(bar)**	T_{outlet} **(K)**	ρ_{outlet} **(kg/m^3)**
0.500	81.06	280.0	923.9	81.00	280.0	923.8
0.755	81.14	280.0	923.8	81.00	280.0	923.8
1.000	81.25	280.0	924.0	81.00	280.0	923.8

Table 5.5 presents the results obtained from the post-processing of all the simulations conducted for Case A_2. Under the thermodynamic regime of this case, the CO_2, due to its closeness to the critical point, is expected to present some compressibility. However, since the pressure drop across the orifice is not significant and the temperature remains approximately uniform, there is no significant variation in the density of the fluid. Therefore, the discharge coefficients were determined with Equation 3.13 considering an expansion factor of 1.

Table 5.5: Post-processing results of Case A_2

U_{inlet} **(m/s)**	$\Delta p_{D\&D/2}$ **(bar)**	T_1 **(K)**	p_1 **(bar)**	ρ_1 **(kg/m^3)**	$\dot{m}$ **(kg/s)**	C_d **(-)**	**Deviation (%)**
0.500	0.08	280.0	81.06	923.8	0.055	0.736	+0.50
0.755	0.18	280.0	81.14	923.9	0.083	0.731	−0.21
1.000	0.31	280.0	81.25	924.0	0.110	0.730	−0.29
Average	—	—	—	—	—	0.733	−2.01

These results indicate the expected increasing pattern in pressure drop and mass flow rate as the inlet velocity increases identified in Case A_1. Moreover, the fluid conditions at the D tapping location do not deviate significantly from those at the inlet, as expected, since this location is upstream of the restriction, and the Δp between the inlet and outlet is not significant. The discharge coefficient resulted in an average value of 0.733, the same obtained in Case A_1, with a maximum deviation between individual points of +0.50% at an inlet velocity of 0.5 m/s. Relative to the C_d of the water case of 0.748 the reported deviation of the discharge coefficient for Case A_2 shows a deviation of -2.01%.

Figures 5.2 and 5.3 illustrate the velocity contour and velocity vectors, for an inlet velocity of 0.755 m/s. Figures 5.4 and 5.5 present the pressure and temperature contours obtained, for the same conditions.

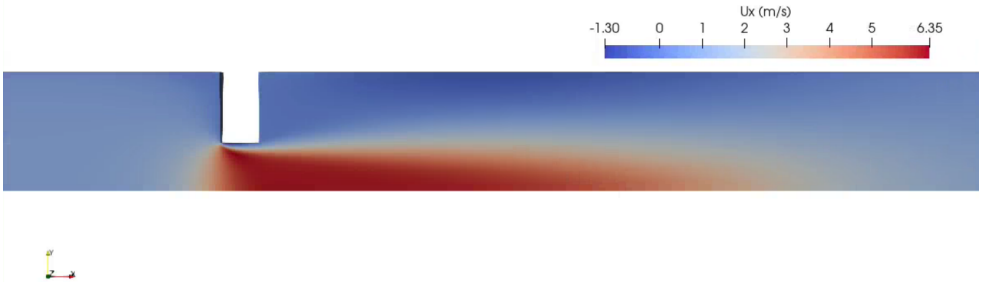

Figure 5.6: Velocity contour of Case A_2 for U_{inlet} of 0.755 m/s.

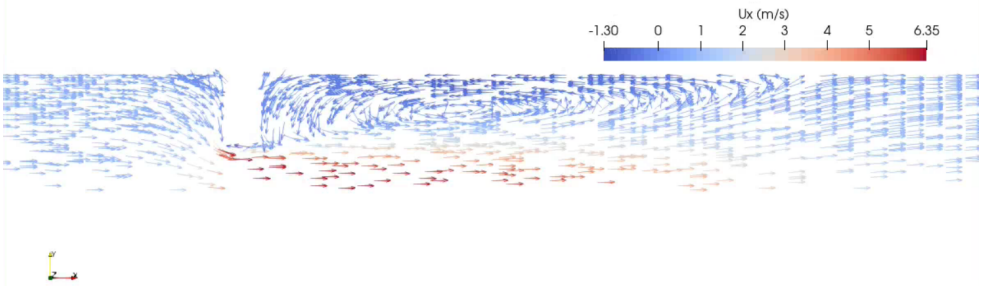

Figure 5.7: Velocity vectors of Case A_2 for U_{inlet} of 0.755 m/s.

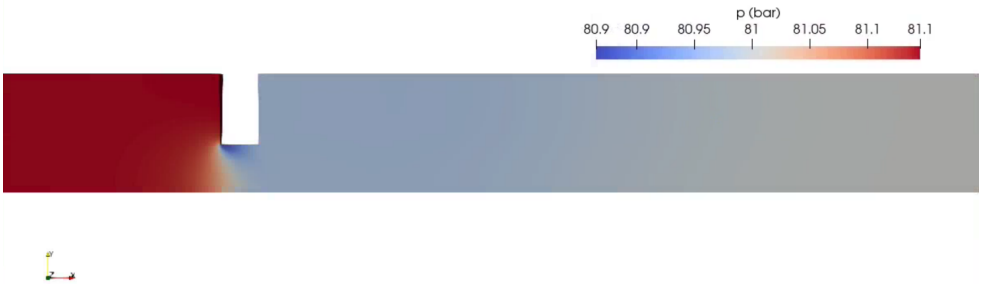

Figure 5.8: Pressure contour of Case A_2 for U_{inlet} of 0.755 m/s.



Figure 5.9: Temperature contour of Case A_2 for U_{inlet} of 0.755 m/s.

The results of Case A_2 exhibit the same behaviour as reported for Case A_1. Figure 5.6 shows the flow accelerating through the restriction, from the 0.755 m/s imposed at the inlet up to approximately 6.35 m/s, and the velocity vectors in Figure 5.7 show the recirculation pattern observed

in the previous cases. Moreover, the pressure contour, illustrated in Figure 5.8, shows the pressure decrease across the restriction, and the temperature contour, in Figure 5.9, shows an almost uniform distribution with slight variation of around 0.02 K, following the velocity pattern. The velocity, pressure and temperature contours, and velocity vectors for the other two simulations carried out are presented in Annex A.3.

From the results obtained for Cases A_1 and A_2, it can be seen that the discharge coefficients determined are very close to the benchmark value obtained for the water case, with a deviation of 2.01% obtained for both cases. These results show that the CFD model developed produces reliable results when the working fluid is changed from water to CO_2.

5.3 Case B - Supercritical without Crossing the Widom Line

This section details the thermodynamic regime of Case B, the alterations made to the CFD model, and the results obtained from the simulations carried out. Having validated with Cases A_1 and A_2, that the model's results remain reliable when the working fluid is switched from water to CO_2, the objective in this case is to simulate carbon dioxide at supercritical conditions far from the critical point, where the thermophysical property gradients are less steep than near the critical point. In these simulations, it is sought to evaluate how the imposed pressure drop affects the resulting mass flow, therefore, instead of imposing the inlet velocity, which fixes the flow rate, the inlet and outlet pressures are imposed. In the previous simulations, the imposed inlet velocity and outlet pressure boundary conditions were adopted in accordance with the reference study [20]. Since the imposed boundary conditions were altered, the quantity monitored to assess the convergence of the solution was altered accordingly. In the previous cases the pressure at the *D* tapping location was the variable monitored, however, since in this case the imposed conditions are the inlet and outlet pressures, the physical quantity selected for monitoring was the volumetric flow rate.

In Case B, the inlet pressure is set to 500 bar and the inlet temperature to 450 K. The outlet pressure ranges from 490 bar to 380 bar. Under these conditions, the evolution of CO_2 remains in a supercritical state without crossing the Widom line. Therefore, for these simulations, the pseudo-phase change model is not yet required, and the thermophysical properties of the fluid are read from a single property table file, which was developed with the same MATLAB code mentioned in Section 5.2. Since the pseudo-phase change model will not be triggered, the volume fraction α is set to 1 throughout the entire domain and will not change throughout the simulation, meaning the simulation is being solved as a single-phase, similar to what was conducted in the previous cases.

5.3.1 Case B - Alterations to CFD Model

When running the simulations for the present case, some changes had to be made to the CFD settings. The first approach to model Case B was to switch the thermophysical properties file used in Cases A_1 and A_2, which ranged the liquid region to another which covered the supercritical region at high temperatures and pressures. However, although the thermophysical properties file

was switched, during the simulations under these conditions, the pressure values of some cells close to the inlet patch were diverging, and the pressure was jumping to values much higher than that of the upper limit established in the properties file. The first approach considered to solve this issue was broadening the temperature and pressure ranges, however, the pressure remained diverging to much higher values, unrealistic for the physics of the flow and thus it was concluded that this solution was not feasible and some alterations were necessary to make the CFD model more robust. Therefore, the first change applied was to the mesh developed.

Typically, when dealing with orifice geometries with a predominant length in the flow direction, the focus of the refinement of the mesh is done in the vicinity of the orifice, and less attention is paid to the length close to the inlet and outlet patches, with sometimes even being that in these areas the aspect ratio is much higher than usual, but usually acceptable for these applications. However, since the divergence was noted to be in cells close to the inlet patch of the orifice, it was chosen to further refine the mesh, focusing on increasing the number of cells of the length both on the inlet and outlet to keep some proportionality. This further refinement increased the number of cells from 25793 to 77000, a considerable increase due to the fact that the pipe length is much higher to that of the orifice length, as observed in Figure 4.2. Ideally, a second mesh sensitivity analysis should have been conducted to assess the new mesh, however, due to time constrains such was not possible. Nevertheless, considering the new mesh is a further refinement from the previous one, to which a mesh sensitivity analysis was conducted, it is believed that this limitation does not impact the obtained results.

Furthermore, some changes were applied to the *fvSchemes* and *fvSolution* files of OpenFOAM, in order to increase the robustness of the model relative to the initial configuration. The pressure equation tolerance was reduced from 10^{-4} to 10^{-8}, and the tolerance of the remaining equations was reduced from 10^{-6} to 10^{-8} as well. The energy convection scheme was altered from first-order upwind to second-order linear-upwind with a limiter, which allows a more accurate solution to be obtained, while the limiter watches for overshoots and blends the scheme back towards first order wherever necessary. The momentum convection scheme was also limited for the same reason. The maximum Courant number was lowered from 0.8 to 0.7 for additional stability of the solution. These changes allowed a much more robust CFD model to be obtained, however, the simulation times increased substantially compared to the previous cases. Considering the alterations conducted, the results presented from this case, and those that will be presented in Case C, were not obtained with the exact CFD model as those of the water and A cases.

5.3.2 Case B Results

In this section, the result of the Case B are presented. Table 5.6 summarises the inlet and outlet conditions of the six points simulated. Contrary to what was reported in the previous cases, as the outlet pressure decreases, there is a noticeable decrease of the outlet density comparative to the density at the inlet, reflecting the compressible nature of CO_2 in this thermodynamic regime.

Table 5.6: Inlet and outlet conditions of Case B

p_{inlet} (bar)	T_{inlet} (K)	ρ_{inlet} (kg/m^3)	p_{outlet} (bar)	T_{outlet} (K)	ρ_{outlet} (kg/m^3)
500.0	450.0	626.2	490.0	449.9	619.1
500.0	450.0	626.2	460.0	449.4	597.1
500.0	450.0	626.2	440.0	448.4	582.8
500.0	450.0	626.2	420.0	448.3	565.5
500.0	450.0	626.2	400.0	447.4	548.6
500.0	450.0	626.2	380.0	446.4	531.1

Table 5.7 presents the pressure drop between the inlet and outlet, and between the D and $D/2$ tappings. Additionally, it presents the temperature, pressure and density at the D tapping location and the mass flow rate obtained from the inlet conditions. The mass flow rate is also presented in Figure 5.10 as a function of the square root of the imposed differential pressure between the inlet and outlet.

Table 5.7: Post-processing results of Case B

p_{outlet} (bar)	$\Delta p_{inlet/outlet}$ (bar)	$\Delta p_{D\&D/2}$ (bar)	T_1 (K)	p_1 (bar)	ρ_1 (kg/m^3)	$\dot{m}$ (kg/s)
490.0	10.0	11.9	450.0	499.8	626.1	0.56
460.0	40.0	47.6	450.0	499.2	625.7	1.10
440.0	60.0	71.4	450.0	498.8	625.4	1.33
420.0	80.0	95.2	450.0	498.4	625.1	1.51
400.0	100.0	119.0	450.0	498.1	624.9	1.66
380.0	120.0	142.7	450.0	497.8	624.6	1.79

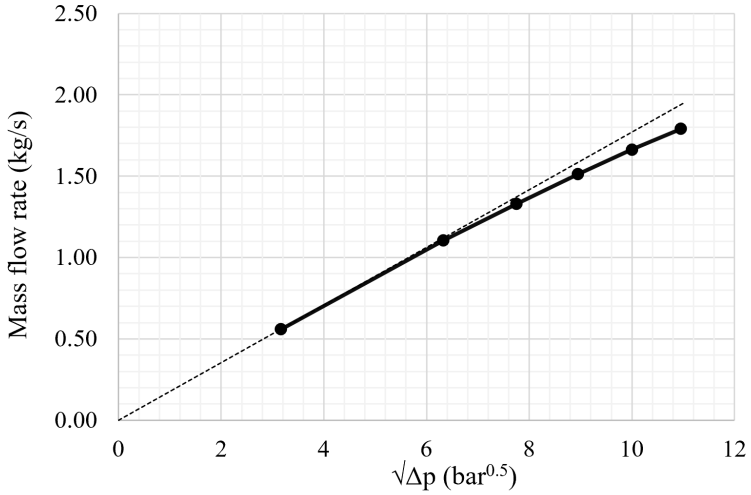

Figure 5.10: Mass flow rate as a function of $\sqrt{\Delta p}$ between the inlet and outlet.

From the results presented in Table 5.7, we can observe that as the outlet pressure decreases, the density reported for the D tapping location, which is used to determine the C_d, also decreases. At an outlet pressure of 380 bar, it reaches a value of 624.62 kg/m^3, a decrease of 1.58 kg/m^3 relative to the inlet. Although this difference is small, it highlights the compressible behaviour of CO_2, since even a slight change in temperature and pressure produced this variation. Analysing these results further, we can verify that the mass flow rate increases as the pressure drop across the orifice increases. Figure 5.10 shows that as the square root of the pressure drop increases, the rate of mass flow rate increase diminishes. For an incompressible fluid, the expected trend is that this dependence remains strictly linear. From the plot presented it can be noticed that as the square root of the pressure drop increases the fluid deviated slightly from the linear trend, indicating an intermediate behaviour between what is usually reported for liquids and gases.

From the data presented in Table 5.7, the discharge coefficients were determined. Initially, the C_d was determined with Equation 3.13, considering the expansion factor as 1. Equation 3.14 was then used to determine the expansion factor, introduced to account for the compressible behaviour of the fluid. Table 5.8 presents the C_d values obtained for incompressible conditions, the determined ε_{exp} and the corrected C_d results.

Table 5.8: Post-processing results of Case B, discharge coefficients

p_{outlet} **(bar)**	$C_{d,inc}$ **(-)**	**Deviation (%)**	ε_{exp} **(-)**	$C_{d,comp}$ **(-)**	**Deviation (%)**
490.0	0.728	+3.74	0.997	0.730	+1.93
460.0	0.719	+2.52	0.989	0.727	+1.61
440.0	0.706	+0.72	0.983	0.719	+0.43
420.0	0.696	−0.73	0.976	0.713	−0.38
400.0	0.685	−2.30	0.970	0.706	−1.30
380.0	0.674	−3.96	0.963	0.699	−2.29
Average	0.701	−6.28	—	0.716	−4.30

The incompressible discharge coefficient resulted in an average value of 0.701, with the highest deviation from the individual points of -3.96% reported for the outlet pressure of 380 bar. Comparing the C_d values obtained after introducing the expansion factor correction, it can be seen that as the pressure drop increases, which, as shown previously, corresponds to a larger change in density, the correction introduced by this factor becomes more noticeable. The C_d at the smallest pressure drop changed the least, and that at the largest pressure drop changed the most. After introducing the correction the average C_d increases from 0.701 up to 0.716. Comparing the incompressible C_d with the value of 0.748 obtained for the water case, a deviation of -6.28 % is reported, which decreases to -4.30% once the expansion factor is introduced. These results indicate that accounting for compressibility is necessary to correctly characterise the discharge coefficient under supercritical conditions of this case.

Figures 5.11 and 5.12 illustrate the velocity contour and vectors in the vicinity of the orifice for Case B for an outlet pressure of 490 bar. The Figures 5.13 and 5.14 show the pressure and temperature contours for the same conditions.

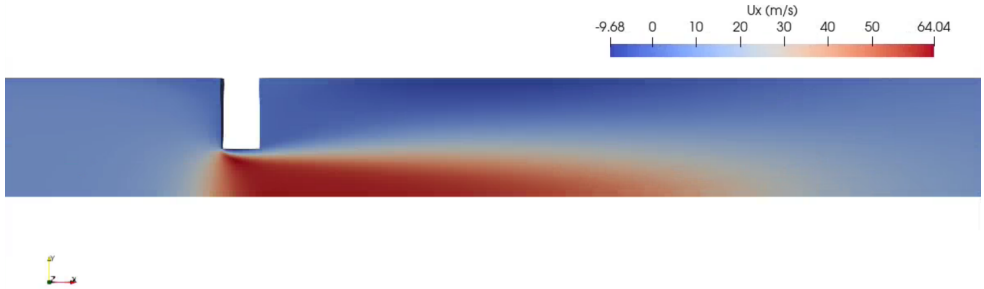

Figure 5.11: Velocity contour of Case B for p_{outlet} of 490 bar.

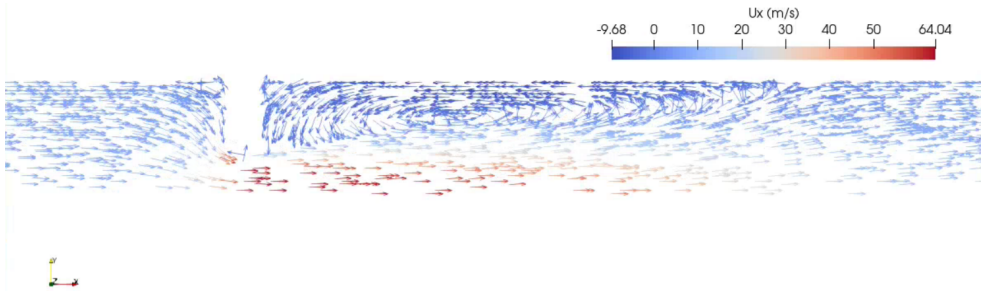

Figure 5.12: Velocity vectors of Case B for p_{outlet} of 490 bar.



Figure 5.13: Pressure contour of Case B for p_{outlet} of 490 bar.

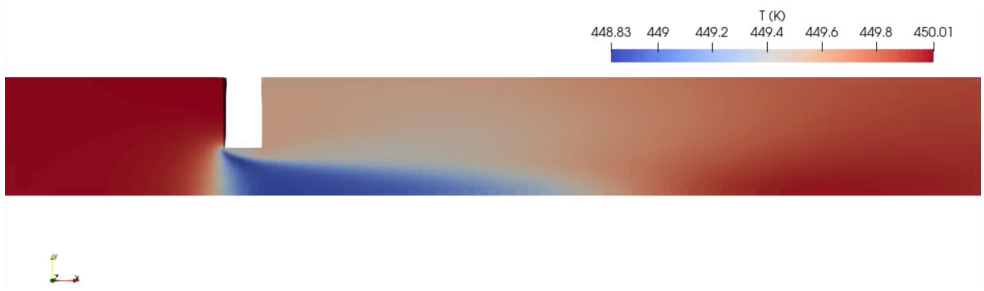

Figure 5.14: Temperature contour of Case B for p_{outlet} of 490 bar.

For Case B at an outlet pressure of 380 bar, the velocity contour and velocity vectors are presented in Figures 5.15 and 5.16, and the pressure and temperature contours in Figures 5.17 and 5.18.

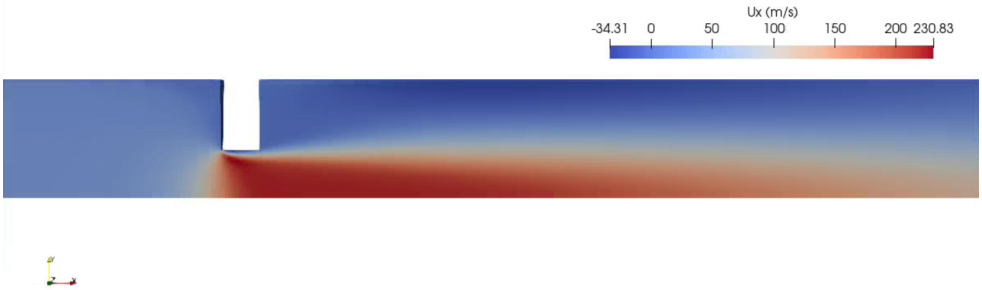

Figure 5.15: Velocity contour of Case B for p_{outlet} of 380 bar.

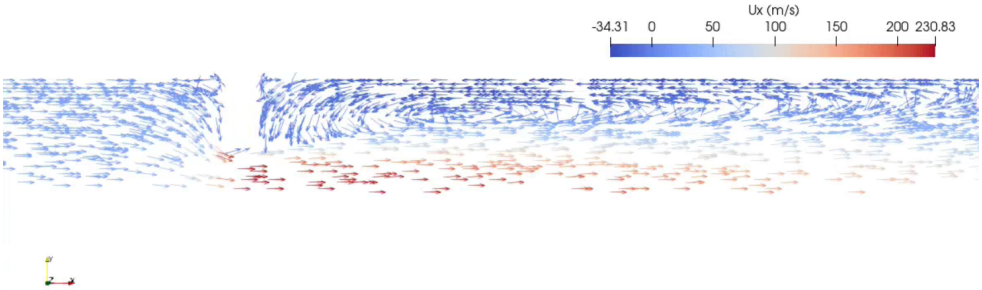

Figure 5.16: Velocity vectors of Case B for p_{outlet} of 380 bar.



Figure 5.17: Pressure contour of Case B for p_{outlet} of 380 bar.

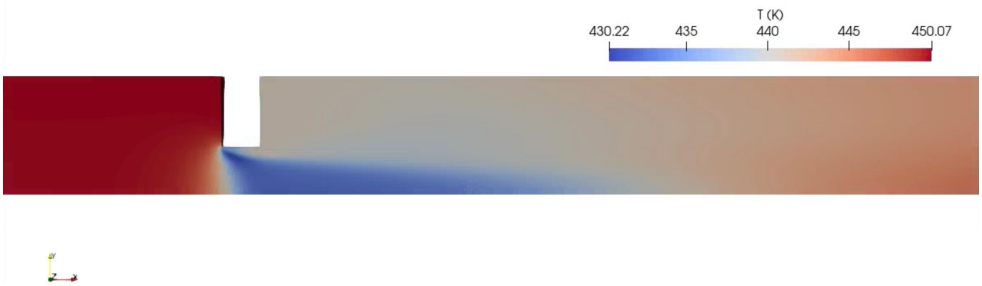

Figure 5.18: Temperature contour of Case B for p_{outlet} of 380 bar.

Comparing the velocity contours of the two simulations, presented in Figures 5.11 and 5.15, it is observed that the maximum velocity increases significantly as the pressure drop across the orifice increases, from a maximum of approximately 64.04 m/s for a pressure drop of 10 bar between the inlet and outlet, to a maximum of approximately 230.83 m/s for a pressure drop of 120 bar between the inlet and outlet. The velocity vectors, shown in Figures 5.12 and 5.16, present the expected recirculation just downstream of the orifice, occurring at approximately the same location in both cases. Regarding the pressure results, both cases show a localised decrease across the orifice followed by a partial recovery further along the channel, as seen in the previous cases, more pronounced for the 380 bar case, consistent with its larger pressure drop. Comparing Figures 5.14 and 5.18, it can be seen that although both temperature gradients follow the same pattern as the vena contracta, the temperature decreases more in the case of the highest pressure drop, indicating that the cooling reported is driven by the local acceleration and pressure drop of the flow. At an outlet of 490 bar the temperature contour shows a variation of approximately 1 K, which increases up to approximately 20 K when the outlet pressure is lowered down to 380 bar.

5.4 Case C - Supercritical Crossing the Widom Line

In this section, the results obtained for the Case C are presented. In this case, the thermodynamic regime defined was of fixed inlet pressure and temperature at 180bar and 340 K, respectively, and an outlet pressure ranging from 170 bar down to 140 bar, progressively increasing the pressure drop. At a temperature of 340 K the crossing of the Widom line is given at 159.3 bar, indicating that in the conditions simulated in Case C the Widom line is crossed and thus we need to implement the pseudo-phase change model.

5.4.1 Case C - Alterations to CFD Model

When moving closer to the critical point, as mentioned previously, the thermophysical property gradients get steeper and thus more care is necessary in the simulations. The first change applied was the activation of the pseudo-phase change model.

Since the Widom line is crossed in this case, it is necessary to define the conditions at which the pseudo-phase change should be triggered. As a cavitation model is being used to represent this transition, the point at which the properties switch from being read from the liquid-like thermophysical property table to the gas-like thermophysical property table is defined through the variable saturation pressure, p_{sat}. As mentioned in Section 3.1, however, this is not a real saturation pressure, but rather the pressure at which the properties switch from the liquid-like to the gas-like side. Because of this reason, this variable is identified as p_c throughout the document, and was defined on the CFD model as a polynomial dependent on the temperature, which was developed in previous work conducted at the von Karman Institute and adopted for the present study.

Contrary to the previous cases, since this thermodynamic regime involves the use of the pseudo-phase change, it is necessary to define two different thermophysical property tables, one

for each pseudo-phase. The lookup tables for this case were generated using the same MATLAB code mentioned previously. In order to prevent the simulations from stopping, the tables were built in a way that defines the properties beyond their true domain. This is necessary because, during the run, a cell may momentarily reach a temperature and pressure corresponding to the gas-like domain while the phase in the simulation is defined as liquid-like, or vice versa. For example, the gas-like table defines the gas-like thermophysical properties within the range in which they exist, and beyond the conditions at which the transition to liquid-like occurs, the values are held constant. The same procedure is applied to the liquid-like table.

The first problem encountered was the definition of the constants C_c and C_v, which control the rate at which mass is transferred between the two phases. Considering what these represent, it is intuitive that they should have high values, as the rate should be instantaneous. However, when doing so the simulation would crash immediately, without even starting, and so they had to be reduced. Commonly, the typical default values employed are of 1 for both coefficients, however, given the instability of the simulations, a more conservative value of 0.5 was adopted, which allowed to simulations to run. With these constants defined, the first point simulated, corresponding to an outlet pressure of 170 bar, presented no issues, since the pressure does not cross the Widom line and therefore the configuration applied to Case B was suited to this point.

For the following points, the same problem observed in Case B started to occur, with the pressure values diverging to unfeasible solutions. Since the mesh was considered to have been sufficiently refined, the solution adopted was to reduce the maximum Courant number to 0.3. Another change implemented was the removal of the artificial term of compression in the phase equation implemented in OpenFOAM, which was eliminated by the settings in the files. In the previous cases the pseudo-phase change model was not active and the domain was treated as single phase, and thus this had no influence on the solution. This term is not physical, being added to the phase equation to keep the boundary between two immiscible fluids sharp, however, in the present case there is no such interface, since it is one continuous fluid.

5.4.2 Case C Results

The results obtained in Case C, considering the polynomial pressure, are presented in this section. Table 5.9 summarises the inlet and outlet conditions of the six points simulated.

Table 5.9: Inlet and outlet conditions for the CO_2 simulations, Case C with polynomial p_c

p_{inlet} **(bar)**	T_{inlet} **(K)**	ρ_{inlet} **(kg/m^3)**	p_{outlet} **(bar)**	T_{outlet} **(K)**	ρ_{outlet} **(kg/m^3)**
180.0	340.0	636.1	170.0	338.6	620.5
180.0	340.0	636.1	165.0	337.8	612.3
180.0	340.0	636.1	160.0	336.9	603.8
180.0	340.0	636.1	155.0	336.0	595.0
180.0	340.0	636.1	150.0	335.0	585.9
180.0	340.0	636.1	145.0	333.9	577.2

Table 5.7 presents the pressure drop between the inlet and outlet, and between the D and $D/2$ tappings, for this case. As in the previous cases, the temperature, pressure and density at the D tapping location and the mass flow rate obtained from the inlet conditions are reported. Figure 5.19 presents the mass flow rate as a function of the square root of the pressure drop between the inlet and outlet of the channel.

Table 5.10: Post-processing results of Case C with polynomial p_c

p_{outlet} **(bar)**	$\Delta p_{inlet/outlet}$ **(bar)**	$\Delta p_{D\&D/2}$ **(bar)**	T_1 **(K)**	p_1 **(bar)**	ρ_1 **(kg/m^3)**	$\dot{m}$ **(kg/s)**
170.0	10.0	11.82	340.0	179.75	635.5	0.562
165.0	15.0	17.83	340.0	179.55	635.1	0.678
160.0	20.0	23.78	340.0	179.63	635.2	0.782
155.0	25.0	29.73	340.0	179.48	634.9	0.866
150.0	30.0	35.66	340.0	179.39	634.7	0.940
145.0	35.0	41.60	340.0	179.31	634.5	1.005

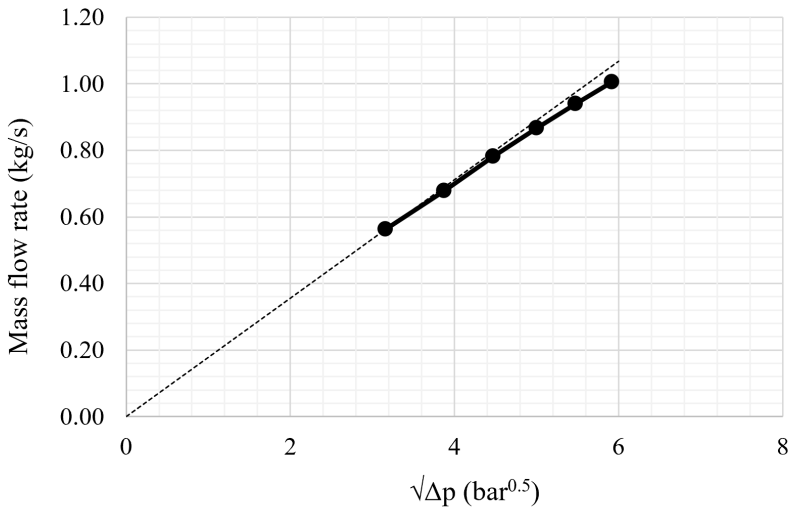

Figure 5.19: Mass flow rate as a function of $\sqrt{\Delta p}$ between the inlet and outlet.

These results indicate that as the differential pressure increases, so does the difference between the density at the inlet conditions and the D tapping location, reaching it maximum at the highest pressure drop. Similar to what was reported in all previous cases, from the results of Table 5.7 and Figure 5.19 it is noted an increase in the mass flow rate with the increase of Δp. The mass flow rate in the plot, in Figure 5.19, presents a slight deviation from the linear trend indicating a compressible behaviour. When compared against the same plot obtained for Case B, illustrated in Figure 5.10, it can be seen that from the same pressure drop, case C shows a higher deviation from the linear trend, aligned with what is expected since the conditions of this case are closer to the critical point.

Table 5.11 summarises the values of the C_d obtained. Similarly to Case B, first the discharge coefficients without taking into consideration the compressibility are presented, followed by the obtained expansion factor for each point and the discharge coefficients with the correction introduced.

Table 5.11: Post-processing results of Case C, discharge coefficients with polynomial p_c

p_{outlet} **(bar)**	$C_{d,inc}$ **(-)**	**Deviation (%)**	ε_{exp} **(-)**	$C_{d,comp}$ **(-)**	**Deviation (%)**
170.0	0.729	+2.57	0.994	0.733	+1.77
165.0	0.716	+0.75	0.991	0.722	+0.27
160.0	0.714	+0.49	0.988	0.723	+0.33
155.0	0.708	−0.32	0.985	0.719	−0.16
150.0	0.701	−1.30	0.982	0.714	−0.82
145.0	0.695	−2.20	0.978	0.710	−1.39
Average	0.711	−4.95	—	0.720	−3.74

The discharge coefficient determined without accounting for the compressibility of the CO_2 resulted in an average value of 0.711, corresponding to a deviation of −4.95% from the benchmark value of 0.748 obtained for the water case. Among the individual points, the highest deviation from the average C_d was +2.57%, at an outlet pressure of 170 bar. When the expansion factor was introduced to correct for the compressibility of the fluid, the C_d increased from 0.711 up to 0.720. After the introduction of this factor, the discharge coefficient that changed the least was the first, at an outlet pressure of 170 bar, and the one that changed the most was the last one, at an outlet pressure of 145 bar. These results are consistent with what was expected as for the highest pressure drop, the compressibility effect of the fluid is more pronounced. The deviation within the C_d values of the simulated points decreased, as well as the deviation from the benchmark value of water, which went from a deviation of -4.95 % to -3.74%.

Figure 5.20 illustrates the velocity contour for an outlet pressure of 170 bar, and Figures 5.21, 5.17 and 5.18 show the α, pressure and temperature contours for the same conditions. The velocity contour presents the same pattern reported in all the previous cases, with the jet forming through the restriction. For a differential pressure of 10 bar between the inlet and outlet faces of the geometry, the velocities achieved are similar to those observed in Figure 5.11 for Case B. For the same pressure drop, in case B a maximum velocity of approximately 64.04 m/s was obtained, and in this case a value of approximately 61.56 was observed. At an outlet pressure of 170 bar, the pressure in the domain does no reach p_c yet and, therefore, the pseudo-phase change model is not yet triggered, as can be seen in the α contour shown in Figure 5.21. The pressure and temperature profiles show slightly more pronounced gradients than those of the 10 bar pressure drop tested in Case B, while maintaining the same pattern reported in the other cases. For instance, the temperature shows variations of approximately 3 K compared with the 1 K reported in Case

B for the same pressure drop. This difference arises from the proximity of Case C to the critical point and Widom line compared to the conditions of Case B.

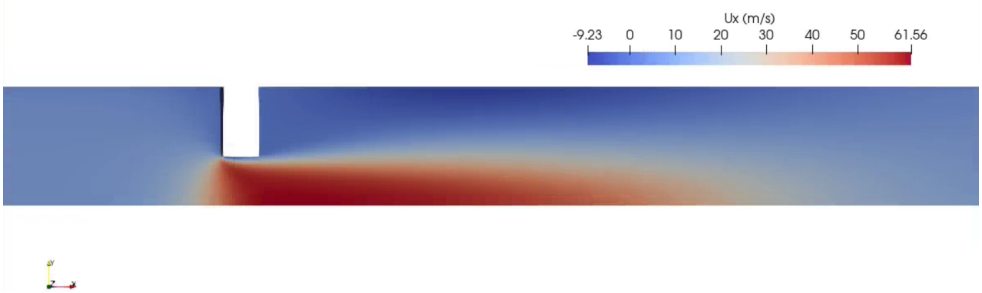

Figure 5.20: Velocity contour of Case C for p_{outlet} of 170 bar, polynomial p_c.

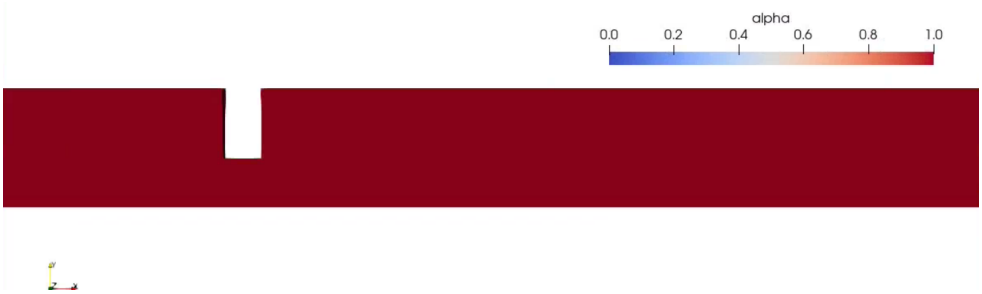

Figure 5.21: α contour of Case C for p_{outlet} of 170 bar, polynomial p_c.

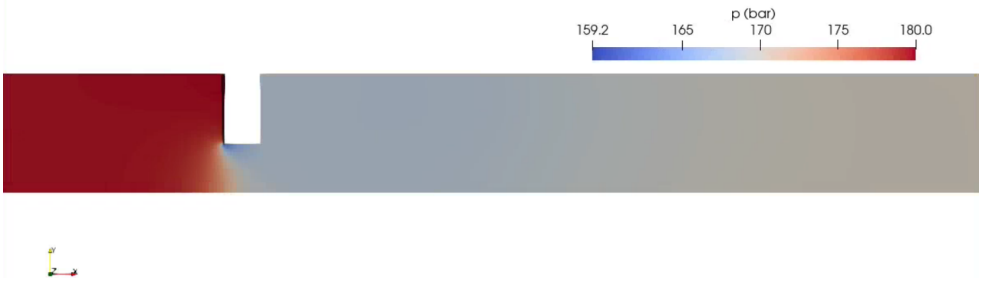

Figure 5.22: Pressure contour of Case C for p_{outlet} of 170 bar, polynomial p_c.

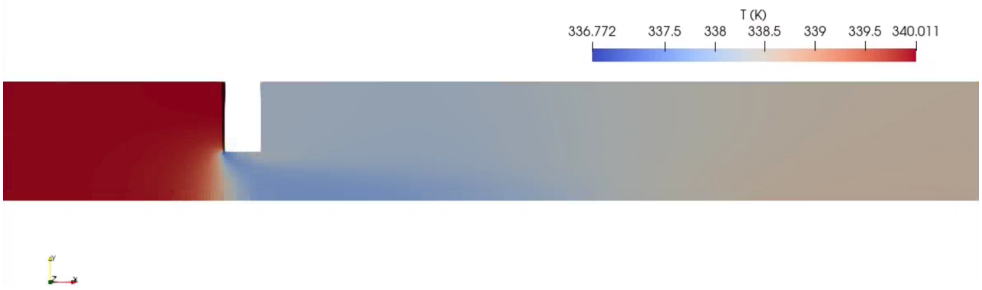

Figure 5.23: Temperature contour of Case C for p_{outlet} of 170 bar, polynomial p_c.

Figure 5.24 illustrates the velocity contour for an outlet pressure of 160 bar, and Figures 5.25, 5.26 and 5.27 show the α, pressure and temperature contours for the same conditions. The velocity contour shows that the velocities obtained for an outlet pressure of 160 bar, corresponding to a 20 bar pressure drop, increased when compared with the previous case of 10 bar. The maximum velocity reported increased from approximately 61.56 m/s to 90.70 m/s. The α contour shows that near the orifice the pressure reaches a value below the local value of p_c and thus the pseudo-phase change is triggered in that corner. This location is consistent with the pressure contour of Figure 5.26, since it is in this region of the orifice that the lowest local pressure is reached. However, it can be noted that only in a very small zone the pseudo-phase change model is triggered. Observing the temperature contour in Figure 5.27, it can be noticed that the temperature decrease is becoming more pronounced, reaching for this conditions a decrease of approximately 6 K. This higher magnitude compared to the previous cases is due to the increased proximity to the Widom line and critical point. Since p_c is defined as a function of temperature, this local cooling results in a lowering of the value of p_c. So, although around the orifice region the pressure is the lowest, since the p_c was lower, only that small region was triggered.

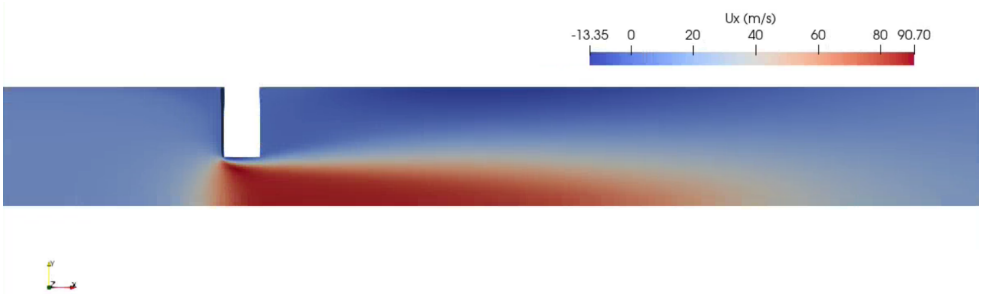

Figure 5.24: Velocity contour of Case C for p_{outlet} of 160 bar, polynomial p_c.

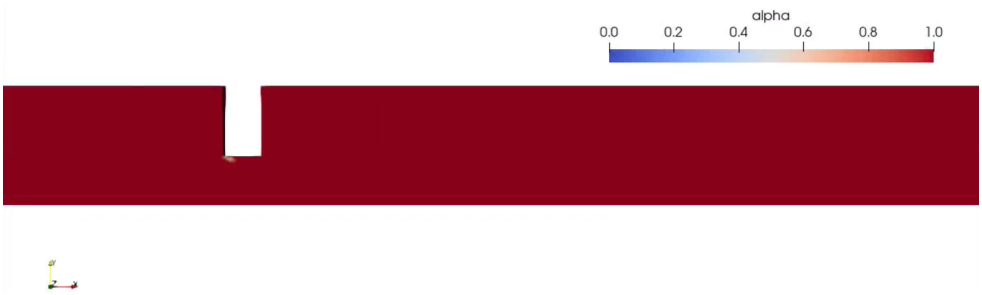

Figure 5.25: α contour of Case C for p_{outlet} of 160 bar, polynomial p_c.

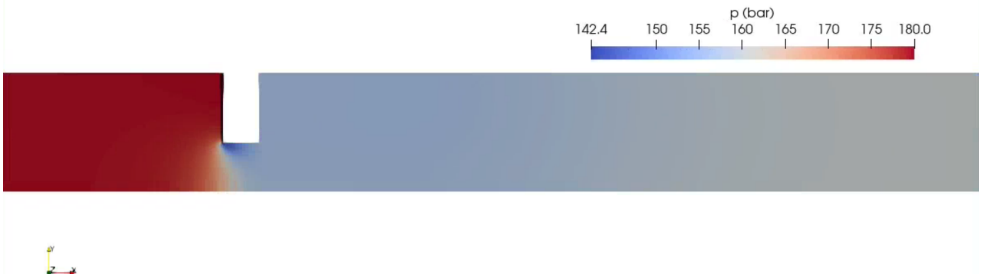

Figure 5.26: Pressure contour of Case C for p_{outlet} of 160 bar, polynomial p_c.

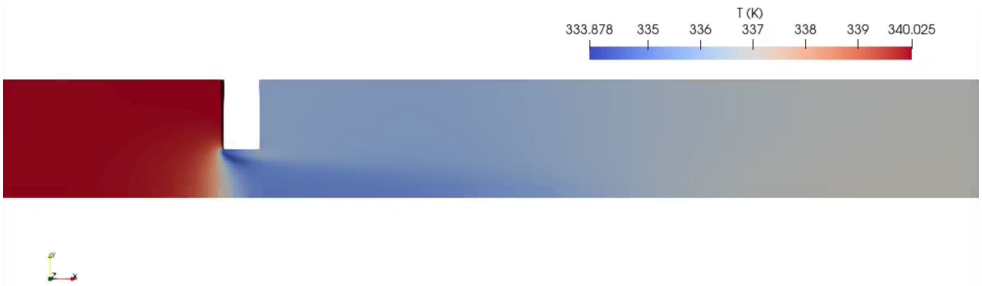

Figure 5.27: Temperature contour of Case C for p_{outlet} of 160 bar, polynomial p_c.

For an outlet pressure of 145 bar, the velocity contour is presented in Figure 5.28, and the α, pressure and temperature contours in Figures 5.29, 5.30 and 5.31.

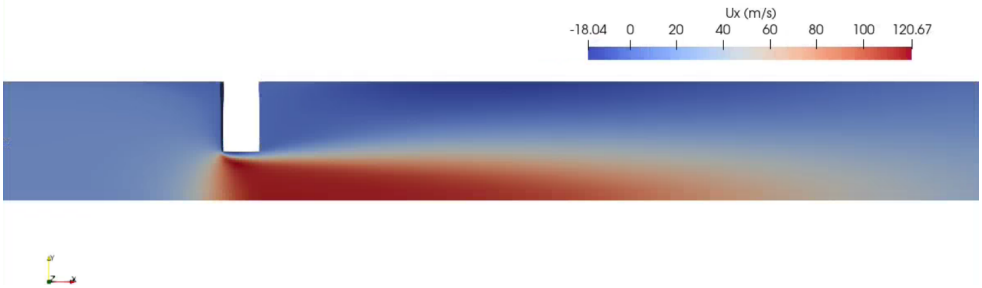

Figure 5.28: Velocity contour of Case C for p_{outlet} of 145 bar, polynomial p_c.

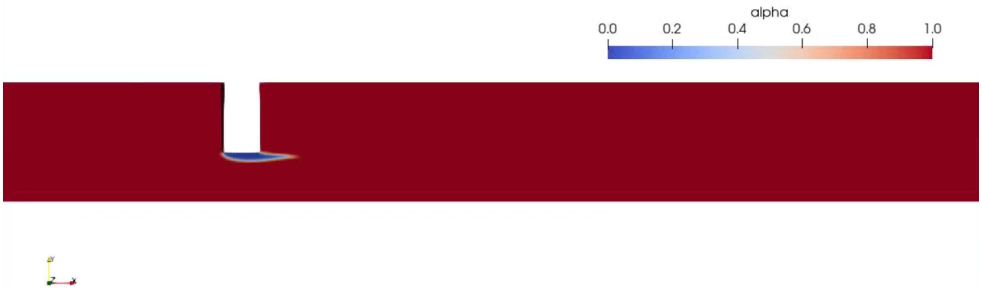

Figure 5.29: α contour of Case C for p_{outlet} of 145 bar, polynomial p_c.

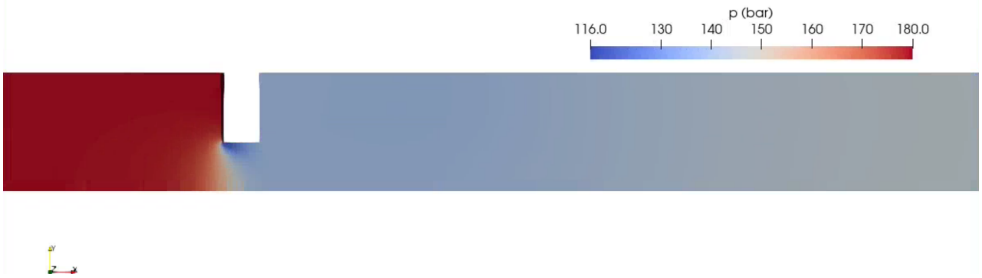

Figure 5.30: Pressure contour of Case C for p_{outlet} of 145 bar, polynomial p_c.

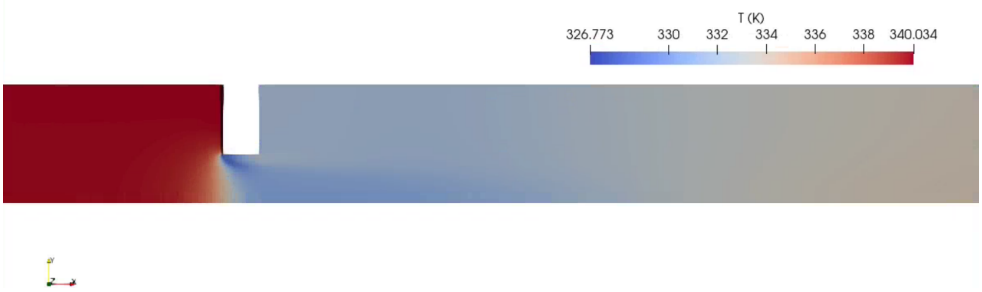

Figure 5.31: Temperature contour of Case C for p_{outlet} of 145 bar, polynomial p_c.

Comparing these results with those previously reported in Case B, the velocities increased significantly, with a maximum of approximately 120.67 m/s, for a pressure drop between the inlet and outlet of 35 bar. It can therefore be seen that, as the pressure drop across the orifice increases, the maximum velocity reported increases accordingly. The α contour shows that the pseudo-phase change is triggered over a larger domain, following the pattern of the pressure contour, although the region remains small. As the Δp increases, the temperature contour presents more pronounced gradients, reaching a temperature drop of approximately 15 K. Comparing to the obtained results in Case B, only at a Δp of 100 bar between the inlet and outlet, is a temperature drop of 15 K reported, as can be seen in Figure A.40. As explained for the previous two simulations, this more pronounced cooling effect compared to Cases A and B is due to the proximity to the Widom line. Although this temperature decrease takes place exactly because we are crossing the Widom line, its decrease makes it so that the p_c is lowered, and the pseudo-phase change is only triggered within the region near the orifice, as shown in Figure 5.29.

It is believed, based on the results presented in the following section, that this behaviour was the underlying issue when trying to simulate outlet pressures under 145 bar. Essentially, as the pressure was dropped, the temperature decreased, which would decrease the p_c, at a higher rate than the pressure of the domain. As a result, the pseudo-phase change would not be triggered, and so the pressure values kept decreasing to much lower values than expected and not reasonable, which fell outside of the range of the thermophysical properties file and eventually led the simulation to terminate. Consequently, broadening the range of the property tables would allow the simulation to continue running, but would not obtain a physically meaningful solution.

Given this issue, the proposed approach was to adopt a constant value for p_c. With this methodology, it is expected to trigger the pseudo-phase change earlier, as the p_c will not be decreased from the temperature drop. Having the pseudo-phase change trigger earlier than in this case means the thermophysical properties for the local points will be read from the extended range of gas-like tables, and not from the physically correct thermophysical properties of the liquid-like table. Since near the Widom line the thermophysical properties of the liquid-like side and gas-like side do not fall that far off from each other, it is expected that the error introduced by reading from the extended gas-like instead of the liquid-like is acceptable. It should be considered that there is no actual phase change happening, and therefore if the error introduced falls under what is considered acceptable, the results can be considered satisfactory.

Therefore, the following section presents the results obtained considering the constant p_c at the inlet conditions. To assess the error introduced by this assumption, prior to present the results for an outlet pressure of 140 bar, the C_d for the same points will be determined as well as a direct comparison between the contours for an outlet pressure of 145 bar between both cases will be presented. Additionally, a direct comparison between the density in three locations, for the outlet pressure of 145 bar, using the polynomial p_c or the constant p_c will be carried out.

5.4.2.1 Results with Constant Pressure

For the simulations with the constant p_c, a value of 159.3 bar was defined, which corresponds to pressure at which the Widom line is crossed at 340 K, the inlet temperature. In this section, the results obtained for these cases are presented. Initially, the inlet and outlet conditions, the obtained results from post-processing, a comparison between the discharge coefficients obtained, the contour for an outlet pressure of 140 bar, a comparison between the densities between these simulations and those considering the polynomial p_c at an outlet pressure of 140 bar, and lastly the profiles obtained for an outlet pressure of 140 bar. Table 5.12 summarises the inlet and outlet conditions for this case.

Table 5.12: Inlet and outlet conditions for the CO_2 simulations, Case C with constant p_c

p_{inlet} **(bar)**	T_{inlet} **(K)**	ρ_{inlet} **(kg/m^3)**	p_{outlet} **(bar)**	T_{outlet} **(K)**	ρ_{outlet} **(kg/m^3)**
180.0	340.0	636.1	170.0	338.6	620.5
180.0	340.0	636.1	165.0	337.8	612.3
180.0	340.0	636.1	160.0	336.9	603.8
180.0	340.0	636.1	155.0	335.6	566.0
180.0	340.0	636.1	150.0	334.6	559.4
180.0	340.0	636.1	145.0	333.6	552.5
180.0	340.0	636.1	140.0	332.4	546.0

Table 5.13 presents the values of pressure drop measured, the conditions of the D tapping location and the obtained mass flow rate. Comparing these results to those presented in Table 5.10

it can be seen that the mass flow rate values decreased slightly to those reported for the polynomial p_c.

Table 5.13: Post-processing results of Case C with constant p_c

p_{outlet} **(bar)**	$\Delta p_{inlet/outlet}$ **(bar)**	$\Delta p_{D\&D/2}$ **(bar)**	T_1 **(K)**	p_1 **(bar)**	ρ_1 **(kg/m^3)**	$\dot{m}$ **(kg/s)**
170.0	10.0	11.82	340.0	179.75	635.5	0.562
165.0	15.0	17.83	340.0	179.61	635.2	0.673
160.0	20.0	23.80	340.0	179.59	635.1	0.774
155.0	25.0	29.67	340.0	179.54	635.0	0.859
150.0	30.0	35.63	340.0	179.44	634.8	0.929
145.0	35.0	41.57	340.0	179.23	634.3	0.992

Table 5.14: Post-processing results of Case C, discharge coefficients with constant p_c

p_{outlet} **(bar)**	$C_{d,inc}$ **(-)**	**Deviation (%)**	ε_{exp} **(-)**	$C_{d,comp}$ **(-)**	**Deviation (%)**
170.0	0.729	+3.39	0.994	0.733	+2.59
165.0	0.710	+0.76	0.991	0.717	+0.28
160.0	0.707	+0.31	0.988	0.716	+0.14
155.0	0.703	−0.27	0.985	0.714	−0.12
150.0	0.694	−1.55	0.982	0.707	−1.08
145.0	0.686	−2.63	0.978	0.702	−1.82
Average	0.705	−5.70	—	0.715	−4.42

For the incompressible C_d, the average value obtained was 0.705. The deviation from the water benchmark value is -5.70%, which increased compared to -4.95% obtained with the polynomial p_c. Comparing the obtained discharge coefficient with the one reported for polynomial pressure, without considering compressibility, of 0.711, the deviation obtained is -0.84%. After introducing the expansion factor, the average value obtained was 0.715, which, compared to the benchmark, resulted in a deviation of -4.42%, which increased compared to the -3.74% obtained with the polynomial p_c. Against the C_d for polynomial p_c, which was 0.720, the deviation obtained is -0.69%. Thus, it can be seen that this assumption results in a higher deviation from the benchmark value but still yields reasonable results with small deviations from the previous Case C results. Additionally, it can be noticed that the values obtained for an outlet pressure of 170 bar are the same for both the constant and the polynomial p_c formulations, which was expected since in neither case is the pressure at which the Widom line is crossed reached, and therefore the pseudo-phase change is not triggered.

Figure 5.32 illustrates the velocity contour for an outlet pressure of 145 bar. Figures 5.33, 5.34 and 5.35 show the α, pressure and temperature contours for the same conditions. Comparing this profiles against those reported for Case C for an outlet pressure of 145 bar in Figures 5.28, 5.29,

5.30, and 5.31, the most noticeable change is in the α contour, which now shows the entire region downstream of the orifice has $\alpha = 0$, meaning it is set as the gas-like phase.

This was expected, since the imposed p_c of 159.3 bar is higher than the local pressure throughout this region, and therefore the pseudo-phase change is triggered across the whole downstream domain rather than only near the orifice. It should be noted that this does not mean this whole domain in reality presents gas-like properties, these are being read from the gas-like file, which was extended past the true gas-like domain by holding the value at the transition constant for each pressure level, as explained previously. The error introduced by this will be assessed below. The remaining contours present smaller but still visible differences, with the constant p_c case reaching a slightly lower minimum temperature and minimum pressure, and a slightly higher maximum velocity.

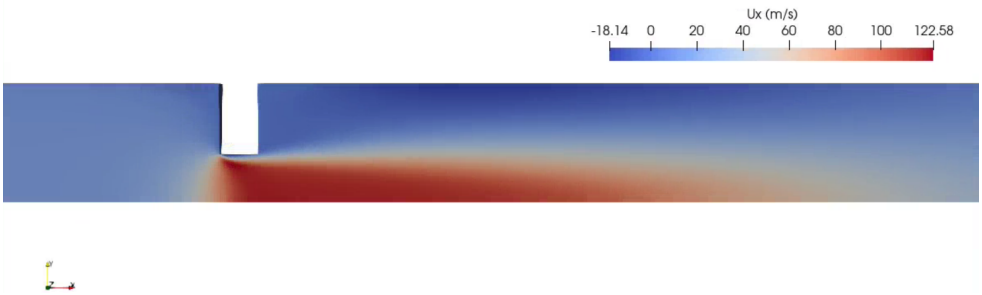

Figure 5.32: Velocity contour of Case C for p_{outlet} of 145 bar, constant p_c.

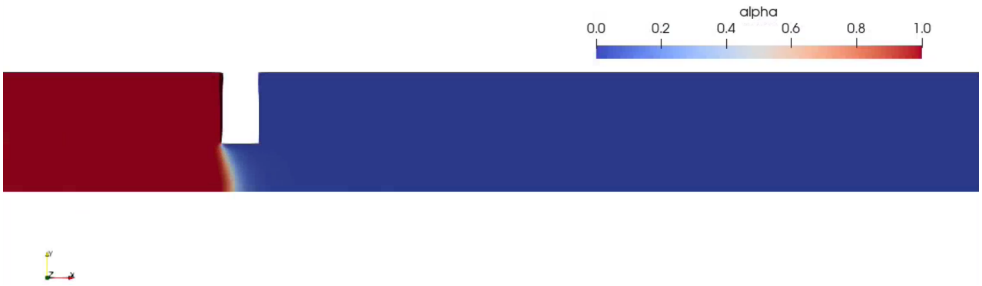

Figure 5.33: α contour of Case C for p_{outlet} of 145 bar, constant p_c.

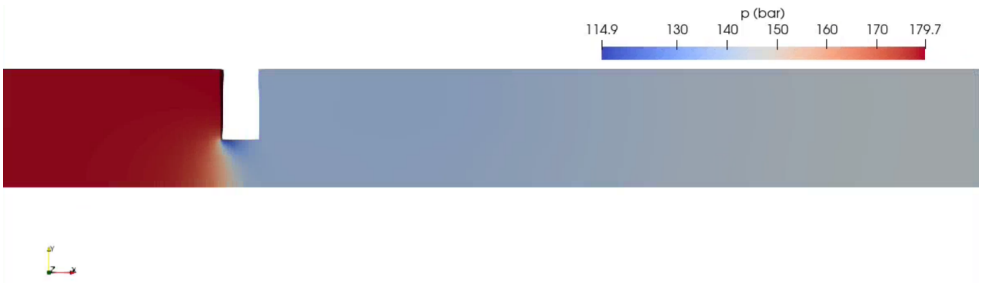

Figure 5.34: Pressure contour of Case C for p_{outlet} of 145 bar, constant p_c.



Figure 5.35: Temperature contour of Case C for p_{outlet} of 145 bar, constant p_c.

To further assess this difference, the density was evaluated at three different locations. As mentioned previously, the gas-like tables were extended beyond the actual gas-like limits by extrapolation, so that the simulation does not terminate when the local conditions fall outside the tabulated range. The purpose of this comparison is to assess what is the difference in densities by reading from the extended gas-like table rather than from the liquid-like one. Table 5.15 presents the values of density taken at three different locations for both formulations, and the deviation obtained from this assumption at these points. The locations selected were 0.25 m, 0.3 m, and 0.35 m, which correspond to 2mm, 52mm and 102 mm downstream from the downstream face of the orifice.

Table 5.15: Density comparison between the polynomial p_c and the constant p_c

Location (m)	ρ **(polynomial** p_c**) (kg/m**^{3}**)**	ρ **(constant** p_c**) (kg/m**^{3}**)**	**Deviation (%)**
0.25	583.1	542.8	-6.91
0.30	576.9	552.5	-4.24
0.35	577.3	552.5	-4.29

From the values of deviation obtained, the highest reported was of -6.91 % in the location of 0.25m, which corresponds to 2 mm downstream from the orifice. Near the orifice region is where the temperature presents the lowest values, meaning it is the locations where the properties are the furthest from the transition point, meaning higher discrepancies are noticeable. Further downstream, at 0.30 and 0.35 m, the deviations are considerably smaller and nearly identical, at -4.24% and -4.29%, respectively, indicating that the effect of the assumption is more notourious at the region close to the restriction. It should be noted that these deviations reflect not only the difference in which property table is used, but may also be affected by the small differences between the two solutions, since the pressure and the velocity differ slightly between the two cases. Based on these results, together with the comparison of the contours and of the discharge coefficient values, which differ by less than 1%, the error introduced by this assumption was considered acceptable. Therefore the simulations, considering a constant value of p_c, were extended up to a lower outlet pressure of 140 bar.

Figures 5.36 illustrate the velocity contour for an outlet pressure of 140 bar. The Figures 5.37, 5.38 and 5.39 show the α, pressure and temperature contours for the same conditions. For this case, the velocity, pressure and temperature present the highest variations of all the simulations

conducted, which aligns with expectations, as we are in the presence of the highest pressure drop from this case. The velocity reached a maximum of approximately 131.93 m/s, the pressure a minimum of 106.2 bar, and the temperature a minimum of 323.19 K. The α contour shows in the zone downstream of the orifice, the thermophysical properties are being read from the gas-like property file.

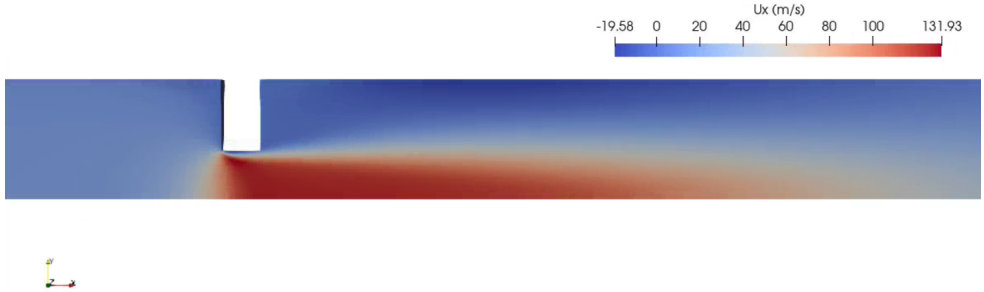

Figure 5.36: Velocity contour of Case C for p_{outlet} of 140 bar, constant p_c.

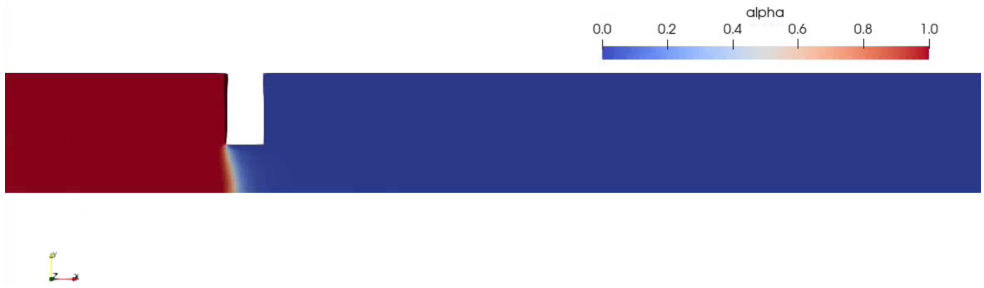

Figure 5.37: α contour of Case C for p_{outlet} of 140 bar, constant p_c.

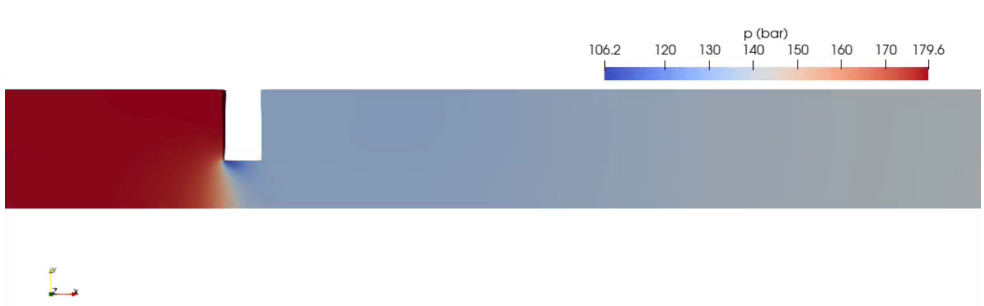

Figure 5.38: Pressure contour of Case C for p_{outlet} of 140 bar, constant p_c.



Figure 5.39: Temperature contour of Case C for p_{outlet} of 140 bar, constant p_c.

5.5 Summary of Results

Having presented and discussed all the results obtained for each case conducted, in this section all the discharge coefficient values obtained, and their respective deviation from the benchmark value, are summarised. The C_d considered for the benchmark was 0.748, obtained and presented in Chapter 4 for the CFD model using water as a working fluid. Table 5.16 summarises all the coefficient results obtained for each case.

Table 5.16: Summary of discharge coefficient results

Case	$C_{d,inc}$ **(-)**	**Deviation (%)**	$C_{d,comp}$ **(-)**	**Deviation (%)**
Water	0.748	—	—	—
Case A_1	0.733	−2.01	—	—
Case A_2	0.733	−2.01	—	—
Case B	0.701	−6.28	0.716	−4.30
Case C (polynomial p_c)	0.711	−4.95	0.720	−3.74
Case C (constant p_c)	0.705	−5.70	0.715	−4.42

Analysing these results, it can be seen that Cases A_1 and A_2 present the lowest deviations from the benchmark C_d, of approximately 2% below it. This was expected, since under the conditions tested the CO_2 behaves as an essentially incompressible fluid, and therefore no correction factor is required. The deviation from the benchmark increases for Case B, which presents the highest deviation of all the cases. The value obtained assuming incompressibility is −6.28%, which reduces to −4.30% once the expansion factor correction is applied. This is consistent with what was expected, given the compressible behaviour of the CO at the conditions tested, and confirms that accounting for compressibility is necessary to correctly characterise the discharge coefficient. Lastly, Case C reports four different values. With the polynomial p_c and without accounting for compressibility, the deviation is −4.95%, reducing to −3.74% with the introduction of the expansion factor, again reflecting the compressible behaviour of the fluid at these conditions. The results obtained with the constant p_c assumption present slightly higher deviations, of −5.70% and −4.42% for the incompressible and compressible formulations, respectively. Comparing the results within each other, they align with the expected behaviour, with the Case A presenting the lowest deviation from the water case. Between Cases B and C, although the CO_2 has a higher

compressibility due to its closeness to the critical point, since for the case B a much larger pressure drop was tested, the compressibility showed a higher impact on the results, and the deviation of Case B was higher than that of Case C.

Chapter 6

Conclusions

The present dissertation had as a main objective to develop a CFD model capable of predicting the behaviour of CO_2 flowing through an orifice geometry across a wide range of thermodynamic regimes, including subcritical and supercritical. To achieve this objective, an initial model was developed and validated using water as the working fluid. A mesh independence study was carried out, and a mesh of 25,793 cells was selected, offering a compromise between accuracy and computational cost. The results were validated against CFD data available in the literature, showing good agreement, and a discharge coefficient of 0.748 was obtained, which served as a reference benchmark value for all subsequent simulations with CO_2. The model was subsequently applied in three different cases, namely to liquid CO_2 in Cases A_1 and A_2, to supercritical conditions far from the critical point in Case B, and lastly to supercritical conditions closer to the critical point, where the Widom line is crossed, in Case C.

Firstly, Case A, which tested liquid CO_2 at various conditions, was presented. For both Cases A_1 and A_2, a deviation of -2.01% was obtained. These results demonstrated that the switch from the working fluid of water to liquid CO_2 had no issues since the obtained discharge coefficients were very similar to those of the benchmark value for water. This outcome was expected, since the properties of liquid CO2 under these conditions are similar, although not identical, to those of water, and the discharge coefficient is a characteristic of the geometry and of the flow regime rather than of the working fluid. The behaviour of the flow confirmed this expectation, with the jet and the recirculation pattern being essentially identical to those observed in the water case, the maximum velocity increasing only from 6.10 m/s to 6.35 m/s, and the temperature field remaining uniform, with variations of around 0.03 K following the same pattern as the velocity contour.

In Case B, CO_2 was simulated at supercritical conditions far from the critical point, and without crossing the Widom line. During the simulations for these conditions, some instabilities were encountered, and some alterations had to be applied to the CFD model, namely increasing the refinement of the mesh focusing on the length of the geometry, lowering the Courant number, reducing the pressure equation tolerance from 10^{-4} to 10^{-8}, for the remaining quantities, the tolerance was reduced from 10^{-6} to 10^{-8}, and the energy convection scheme was altered from

first-order upwind to second-order linear-upwind. After the implementation of these changes, the results were obtained and showed that the average discharge coefficient, without accounting for compressibility, presented a deviation of -6.28% from the water benchmark. Once the expansion factor correction was introduced, this deviation improved to -4.30 %, confirming that accounting for compressibility is necessary to correctly characterise CO_2 flow in this regime. The compressible behaviour of the fluid in this regime was reported in the outlet density, which decreased noticeably relative to the inlet as the outlet pressure was lowered, and in the mass flow rate, which deviated from the linear dependence on the square root of the imposed differential pressure expected for an incompressible fluid. The effect of the expansion factor was found to increase with the pressure drop, the discharge coefficient at the smallest pressure drop being the least affected by the correction and that at the largest pressure drop the most. Regarding the thermal behaviour, a temperature variation of approximately 1 K was reported for an outlet pressure of 490 bar, which increased up to approximately 20 K when the outlet pressure was lowered down to 380 bar, indicating that the cooling reported is driven by the local acceleration and pressure drop of the flow.

Case C, at supercritical conditions closer to the critical point and crossing the Widom line, produced the most significant findings. Due to the proximity to the critical point, compared to Case B, some other alterations had to be conducted to the CFD model once again. Namely, the Courant number was lowered to a much more conservative value, which resulted in a significant increase in computational effort, and the artificial term of compression in the phase equation was not considered. After these alterations, the model was able to capture the transition of the CO_2 from an inlet pressure of 180 bar down to an outlet pressure of 145 bar, resulting in deviations of -4.95% and -3.74% for the incompressible and compressible behaviour, respectively. However, it was found that below this outlet pressure, the simulations would terminate since the pressure would jump to values below the lower limit of the thermophysical property tables. The cooling of the fluid after the restrictions, which was more pronounced due to the proximity to the Widom line, would lower the value of p_c at a higher rate than the pressure of the domain. It is believed that this was the underlying reason why the pressure in the simulations was lowering abruptly to infeasible solutions. To overcome this, a constant p_c value of 159.3 bar, corresponding to the inlet temperature of 340 K, was adopted, which allowed the simulations to be extended past 145 bar. The error introduced by this assumption was assessed and found to be acceptable, as the discharge coefficients deviated by -0.84% and -0.69% from those obtained with the polynomial formulation, with a maximum local density deviation reported of -6.91% between the simulations considering the polynomial and constant p_{sat}, tested at an outlet pressure of 145 bar.

Considering the results presented, it is important to take into consideration the limitations of the present model. It should be emphasised, once again, that the evolution being modelled does not involve actual cavitation, and the adoption of the cavitation model was done as a strategy to overcome the numerical difficulties encountered when simulating SCFs. More specifically, the adoption of a two-phase flow formulation aims to capture the crossing of the Widom line, which conceptually divides the liquid-like from the gas-like behaviour of the sCO_2. In reality, this crossing of the Widom line is instantaneous, and the cavitation model introduces coefficients which

regulate the rate of cavitation, since cavitation is not an instantaneous phenomenon. Nonetheless, it is believed that this does not have a significant impact on the results obtained. Moreover, the present model adopted a constant reference pressure, independent of the temperature, for the crossing of the Widom line to overcome the difficulties encountered, whereas in reality this pressure is dependent on the local temperature. Nevertheless, the error introduced by this assumption was assessed and found to be within an acceptable range. Lastly, due to time constraints, a mesh sensitivity check was not repeated for the refined mesh adopted in Cases B and C. However, considering this mesh was a refinement of the previous mesh for the same geometry, which was subjected to the mesh independence study, it is believed that it does not have an impact on the results presented.

Thus, it can be concluded that the objective of developing a CFD model capable of predicting the behaviour of CO_2 through an orifice geometry across subcritical and supercritical regimes was achieved, with the discharge coefficients obtained presenting a deviation of 2.01% from the benchmark value for the liquid region, and under 4.42% for the supercritical cases once the compressibility was accounted for. Additionally, the results show that the pseudo-phase change approach is a good methodology that allows the crossing of the Widom line to be simulated, overcoming the numerical instabilities that arise from the sharp variation of the thermophysical properties in this region, within the thermodynamic regime tested in this study.

Chapter 7

Future Work

The work conducted in the present dissertation developed a CFD model capable of representing the flow of CO_2 through an orifice geometry across subcritical and supercritical conditions. Nevertheless, the CFD model constructed relies on a set of assumptions and presents the limitations reported in Chapter 6. Therefore, in this chapter, recommendations for future work are proposed:

- Carrying out a sensitivity analysis of the model coefficients. The cavitation model introduces coefficients which regulate the rate of cavitation. However, since the process being represented is not an actual phase change and is instantaneous, these coefficients introduce a delay which should not exist. A sensitivity study, in which these coefficients are varied and the results obtained with the CFD model are compared, would allow the influence to be assessed the influence of these coefficients on the results, and to identify the most appropriate values to be considered for simulating the behaviour of the CO_2 under these conditions;
- The results obtained from the CO_2 simulations were compared against the water case, which was recreated based on a CFD study available in the literature. A comparison with experimental data obtained for CO_2 under the same thermodynamic regimes, flowing through an orifice geometry of comparable dimensions, would allow the results of the CFD model to be validated directly for the fluid and the conditions of interest, rather than comparing to the CFD model using water as a working fluid;
- The simulations conducted covered a limited range of inlet conditions and pressure drops. Extending the study to other inlet temperatures and pressures, and to larger pressure drops, would be an interesting work to conduct, in particular for conditions closer to the critical point, where the property gradients are even steeper;

References

[1] Jia-Qi Guo et al. “A Systematic Review of Supercritical Carbon Dioxide (S-CO_2) Power Cycle for Energy Industries: Technologies, Key Issues, and Potential Prospects”. In: *Energy Conversion and Management* 258 (2022), p. 115437. DOI: 10.1016/j.enconman.2022.115437.

[2] Gaoliang Liao et al. “Effects of Technical Progress on Performance and Application of Supercritical Carbon Dioxide Power Cycle: A Review”. In: *Energy Conversion and Management* 199 (2019), p. 111986. DOI: 10.1016/j.enconman.2019.111986.

[3] Luisa F. Cabeza et al. “Supercritical CO_2 as heat transfer fluid: A review”. In: *Applied Thermal Engineering* 125 (2017), pp. 799–810. ISSN: 1359-4311. DOI: 10.1016/j.applthermaleng.2017.07.049.

[4] AbdElRahman AbdElDayem, Martin T. White, and Abdulnaser I. Sayma. “Comparison of CFD Predictions of Supercritical Carbon Dioxide Axial Flow Turbines Using a Number of Turbulence Models”. In: *Proceedings of the ASME Turbo Expo 2021: Turbomachinery Technical Conference and Exposition*. Volume 10: Supercritical CO_2. American Society of Mechanical Engineers, 2021, V010T30A010. DOI: 10.1115/GT2021-58883.

[5] Yunus A. Çengel, Michael A. Boles, and Mehmet Kanoğlu. *Thermodynamics: An Engineering Approach*. 9th ed. McGraw-Hill Education, 2019. ISBN: 978-1-259-82267-4.

[6] Raj C. Patel et al. “Analysis and Development of a Small-Scale Supercritical Carbon Dioxide (sCO_2) Brayton Cycle”. In: *Energies* 15.10 (2022), p. 3580. DOI: 10.3390/en15103580.

[7] Gaoliang Liao et al. “Widom Line of Supercritical CO_2 Calculated by Equations of State and Molecular Dynamics Simulation”. In: *Journal of CO_2 Utilization* 62 (2022), p. 102075. DOI: 10.1016/j.jcou.2022.102075.

[8] Haomin Yuan et al. “Simulation of Supercritical CO_2 Flow Through Circular and Annular Orifice”. In: *Journal of Nuclear Engineering and Radiation Science* 1.2 (2015), p. 021003. DOI: 10.1115/1.4029337.

[9] Yuan Zhou et al. “Numerical Simulation of Supercritical Carbon Dioxide Critical Flow in the Nozzle Tube”. In: *Journal of Nuclear Engineering and Radiation Science* 4.1 (2018), p. 011018. DOI: 10.1115/1.4037896.

[10] Haomin Yuan et al. “Numerical Modeling of Supercritical Carbon Dioxide Flow in See-Through Labyrinth Seals”. In: *Nuclear Engineering and Design* 293 (2015), pp. 436–446. DOI: 10.1016/j.nucengdes.2015.08.016.

[11] Enrico Rinaldi, Rene Pecnik, and Piero Colonna. “Enhancing Robustness and Accuracy of Supercritical CO_2 Compressor Computational Fluid Dynamics Simulations Using Tabular Thermodynamic Properties-Based Numerical Method”. In: *Energy* 305 (2024), p. 132332. DOI: 10.1016/j.energy.2024.132332.

[12] A. Cantiani and J. Pinho. *SURPRISE – Supercritical Carbon Dioxide: Exploration of Modelling Challenges Test Cases*. Tech. rep. von Karman Institute for Fluid Dynamics, Environmental and Applied Fluid Dynamics Department, Sept. 25, 2025.

[13] Teng Wan et al. "Challenges in the Modeling and Simulation of Turbulent Supercritical Fluid Flows and Heat Transfer". In: *Propulsion and Energy* 1 (2025), p. 6. DOI: 10.1007/s44270-024-00005-3.

[14] V. V. Brazhkin et al. "Where is the supercritical fluid on the phase diagram?" In: *Physics-Uspekhi* 55.11 (2012), pp. 1061–1079. ISSN: 1063-7869. DOI: 10.3367/UFNe.0182.201211a.1137.

[15] Erdogan Kiran, Pablo G. Debenedetti, and Cor J. Peters, eds. *Supercritical Fluids: Fundamentals and Applications*. Vol. 366. NATO Science Series E: Applied Sciences. Dordrecht: Kluwer Academic Publishers, 2000. ISBN: 0-7923-6235-7.

[16] Sanford Klein and Gregory Nellis. *Thermodynamics*. 1st ed. Cambridge University Press, 2011. ISBN: 9780511994883.

[17] Haomin Yuan. "Simulations of Supercritical Fluids Flow through Complex Geometries". PhD thesis. University of Wisconsin–Madison, 2015.

[18] Sahil Gupta et al. "Developing empirical heat-transfer correlations for supercritical CO_2 flowing in vertical bare tubes". In: *Nuclear Engineering and Design* 261 (2013), pp. 116–131. DOI: 10.1016/j.nucengdes.2013.02.048.

[19] Sandeep Pidaparti. "A Computational Study on the Leakage of Supercritical Carbon Dioxide Through Labyrinth Seals". Thesis. 2013.

[20] Manish S. Shah et al. "Analysis of Flow Through an Orifice Meter: CFD Simulation". In: *Chemical Engineering Science* 71 (2012), pp. 300–309. DOI: 10.1016/j.ces.2011.11.022.

[21] M. M. Tukiman et al. "CFD Simulation of Flow Through an Orifice Plate". In: *IOP Conference Series: Materials Science and Engineering* 243.1 (2017), p. 012036. DOI: 10.1088/1757-899X/243/1/012036.

[22] Elsevier. *Volume of Fluid Method: An Overview*. ScienceDirect Topics. URL: https://www.sciencedirect.com/topics/engineering/volume-of-fluid-method (visited on 08/07/2026).

[23] Kiarash Kord. *The Volume of Fluid (VOF) Method in CFD: A Guide to Interface Tracking*. CFDLAND, 2024. URL: https://cfdland.com/comprehensive-guide-on-volume-of-fluid-vof-model-in-multiphase-cfd-simulation/ (visited on 08/07/2026).

[24] ANSYS, Inc. *ANSYS FLUENT 12.0 Theory Guide: 16.3.2 Volume Fraction Equation*. 2009. URL: https://www.afs.enea.it/project/neptunius/docs/fluent/html/th/node299.htm.

[25] H. K. Versteeg and W. Malalasekera. *An Introduction to Computational Fluid Dynamics: The Finite Volume Method*. 2nd ed. Pearson Education Limited, 2007. ISBN: 9780131274983.

[26] OpenCFD Limited. *k–ε Turbulence Model*. OpenFOAM Documentation, Version 2312. 2023. URL: https://doc.openfoam.com/2312/tools/processing/models/turbulence/ras/linear-evm/rtm/kEpsilon/ (visited on 08/17/2026).

[27] ANSYS, Inc. *ANSYS FLUENT 12.0 User's Guide: Mesh Quality*. 2009. URL: https://www.afs.enea.it/project/neptunius/docs/fluent/html/ug/node167.htm (visited on 08/18/2026).

[28] Chris Greenshields and Henry Weller. *Notes on Computational Fluid Dynamics: General Principles—Aspect Ratio*. Updated 11 July 2026. CFD Direct. Apr. 11, 2022. URL: https://doc.cfd.direct/notes/cfd-general-principles/aspect-ratio (visited on 08/18/2026).

[29] OpenCFD Limited. *OpenFOAM User Guide*. 2011. URL: http://www.openfoam.org/docs/user/ (visited on 08/17/2026).

[30] Ali Abbaspur. *Courant Number (CFL Number) in CFD: Formula & CFL Condition*. CFDLAND. URL: https://cfdland.com/what-is-a-courant-number-cfl-number/ (visited on 09/08/2026).

[31] Béla G. Lipták, ed. *Instrument Engineers' Handbook, Volume One: Process Measurement and Analysis*. 4th ed. Boca Raton: CRC Press, 2003. ISBN: 978-0-8493-1083-6. DOI: 10.1201/9781420064025.

[32] International Organization for Standardization. *Measurement of Fluid Flow by Means of Pressure Differential Devices Inserted in Circular Cross-Section Conduits Running Full—Part 1: General Principles and Requirements*. June 2003.

[33] International Organization for Standardization. *Measurement of Fluid Flow by Means of Pressure Differential Devices Inserted in Circular Cross-Section Conduits Running Full—Part 2: Orifice Plates*. June 2003.

Appendix A

Simulation Results

A.1 Case Water

Figures A.1 and A.2 illustrate the velocity contour and vectors of water, respectively, for an inlet velocity of 0.5 m/s. Figures A.3 and A.4 show the pressure and temperature contours for the same conditions.

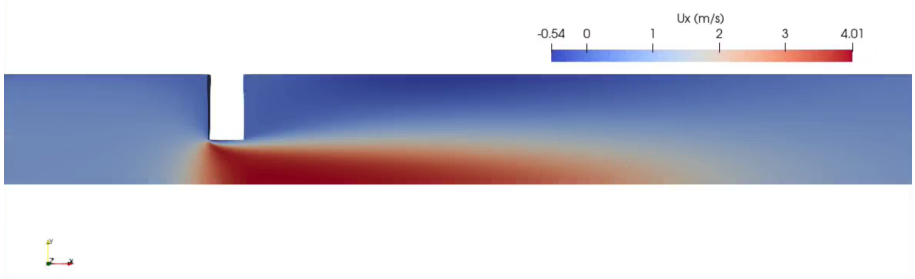

Figure A.1: Velocity contour of water case for U_{inlet} of 0.5 m/s.

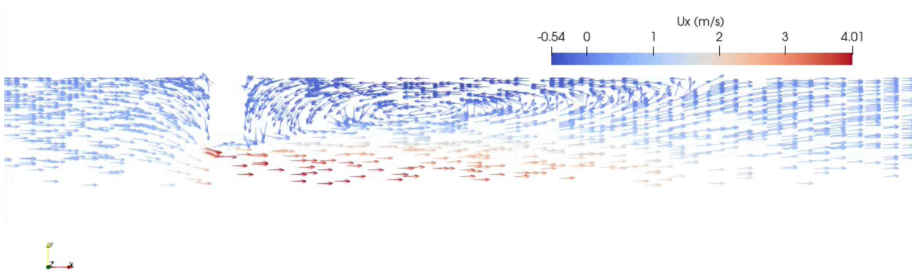

Figure A.2: Velocity contour of water case for U_{inlet} of 0.5 m/s.

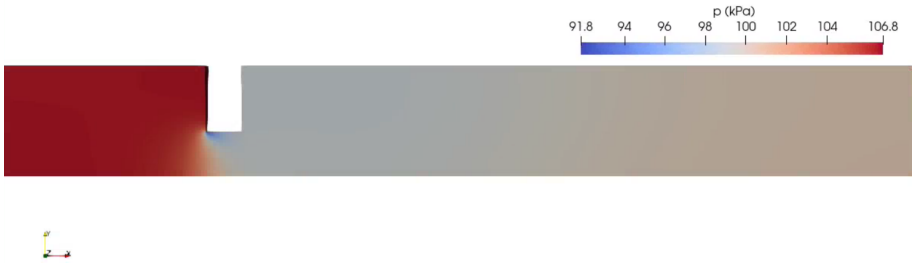

Figure A.3: Pressure contour of water case for U_{inlet} of 0.5 m/s.

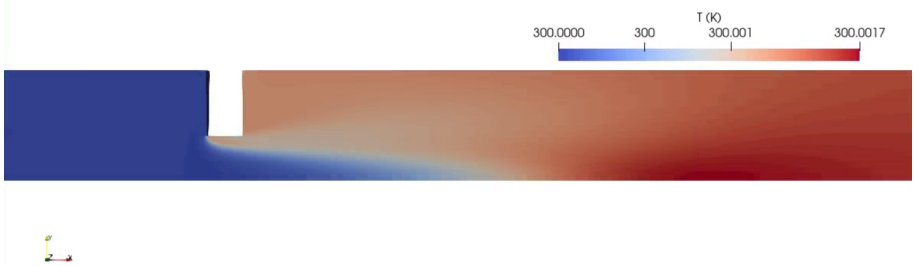

Figure A.4: Temperature contour of water case for U_{inlet} of 0.5 m/s.

Figures A.5 and A.6 illustrate the velocity contour and vectors of water, respectively, for an inlet velocity of 1 m/s. Figures A.7 and A.8 show the pressure and temperature contours for the same conditions.

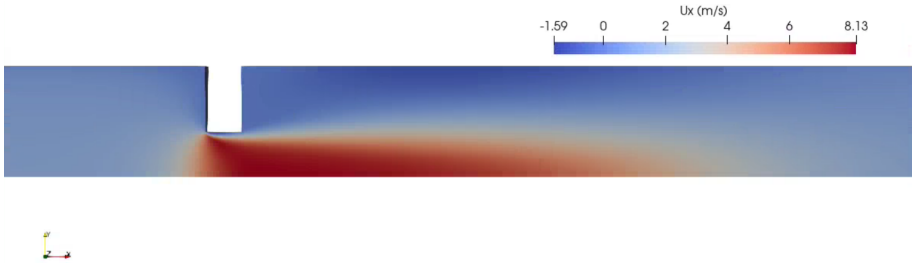

Figure A.5: Velocity contour of water case for U_{inlet} of 1 m/s.

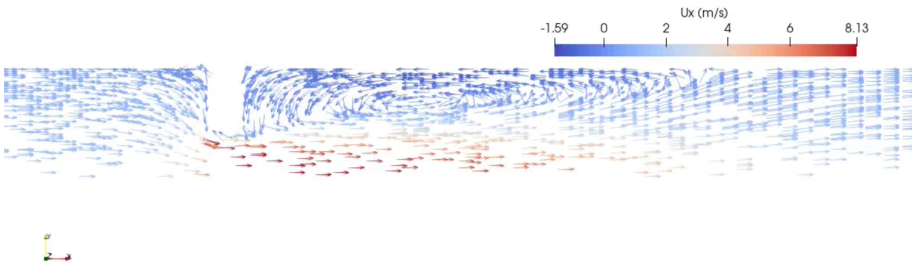

Figure A.6: Velocity contour of water case for U_{inlet} of 1 m/s.

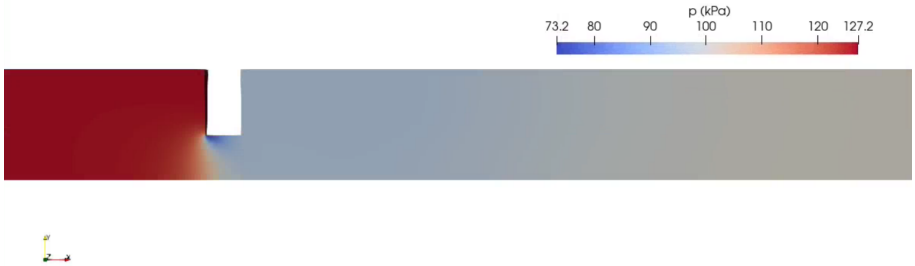

Figure A.7: Pressure contour of water case for U_{inlet} of 1 m/s.

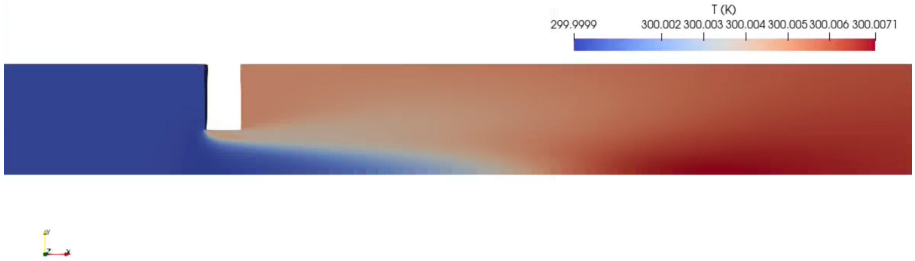

Figure A.8: Temperature contour of water case for U_{inlet} of 1 m/s.

A.2 Case A_1

Figures A.9 and A.10 illustrate the velocity contour and vectors of liquid CO_2 in Case A_2, respectively, for an inlet velocity of 0.5 m/s. Figures A.11 and A.12 show the pressure and temperature contours for the same conditions.

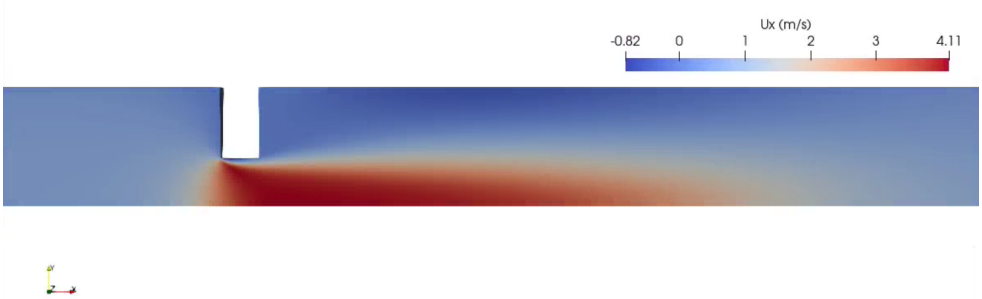

Figure A.9: Velocity contour of Case A_1 for U_{inlet} of 0.5 m/s.

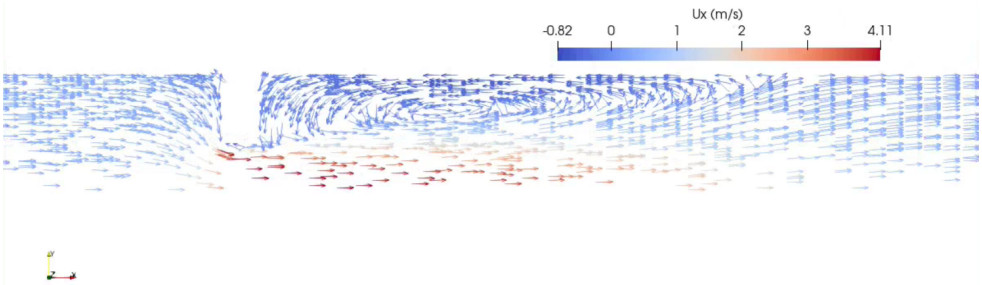

Figure A.10: Velocity vectors of Case A_1 for U_{inlet} of 0.5 m/s.

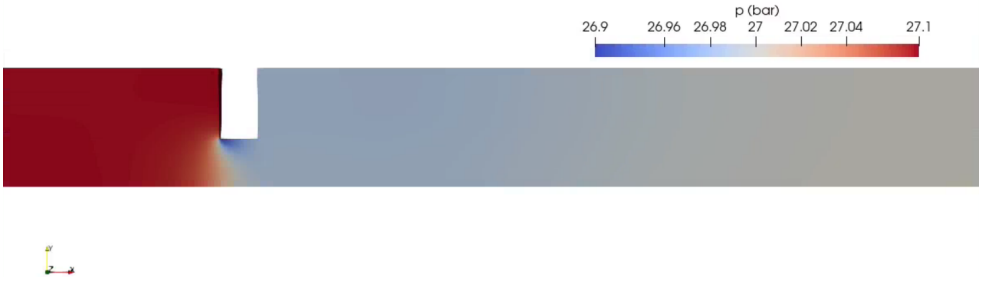

Figure A.11: Pressure contour of Case A_1 for U_{inlet} of 0.5 m/s.



Figure A.12: Temperature contour of Case A_1 for U_{inlet} of 0.5 m/s.

Figures A.13 and A.14 illustrate the velocity contour and vectors of liquid CO_2 in Case A_1, respectively, for an inlet velocity of 1 m/s. Figures A.15 and A.16 show the pressure and temperature contours for the same conditions.

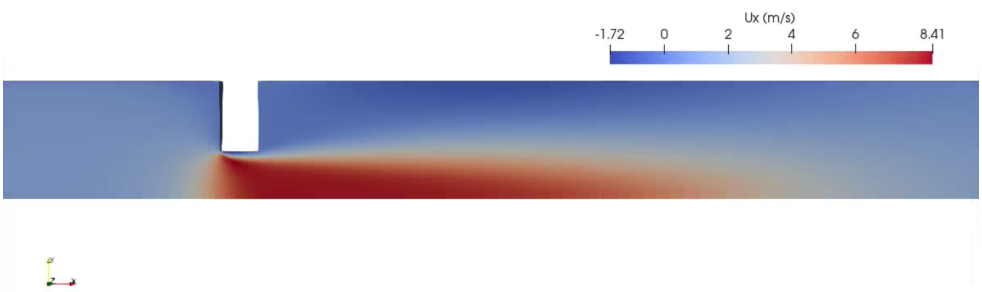

Figure A.13: Velocity contour of Case A_1 for U_{inlet} of 1 m/s.

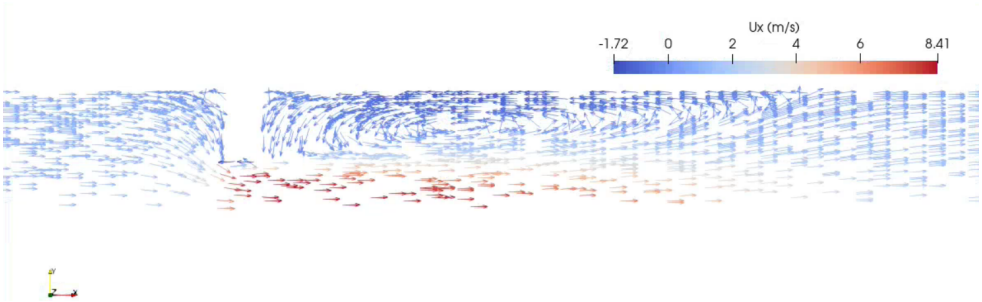

Figure A.14: Velocity vectors of Case A_1 for U_{inlet} of 1 m/s.



Figure A.15: Pressure contour of Case A_1 for U_{inlet} of 1 m/s.



Figure A.16: Temperature contour of Case A_1 for U_{inlet} of 1 m/s.

A.3 Case A_2

Figures A.17 and A.18 illustrate the velocity contour and vectors of liquid CO_2 in Case A_1, respectively, for an inlet velocity of 0.5 m/s. Figures A.19 and A.20 show the pressure and temperature contours for the same conditions.

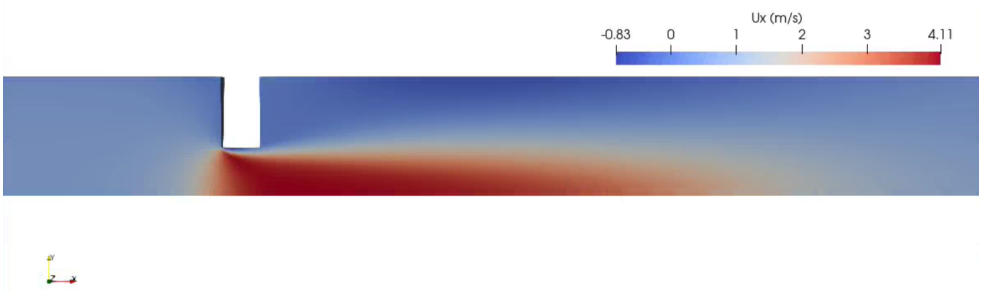

Figure A.17: Velocity contour of Case A_2 for U_{inlet} of 0.5 m/s.

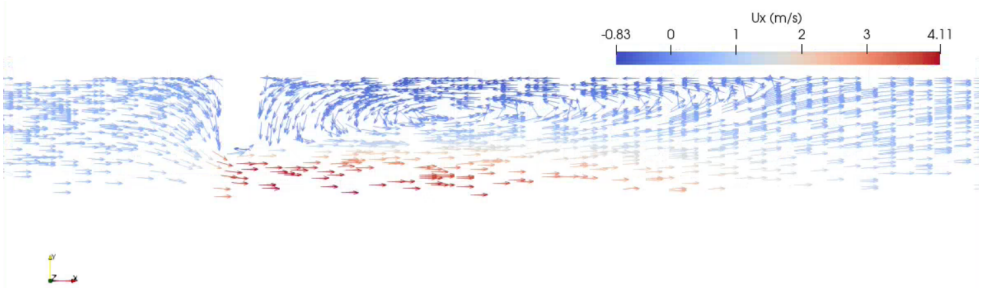

Figure A.18: Velocity vectors of Case A_2 for U_{inlet} of 0.5 m/s.

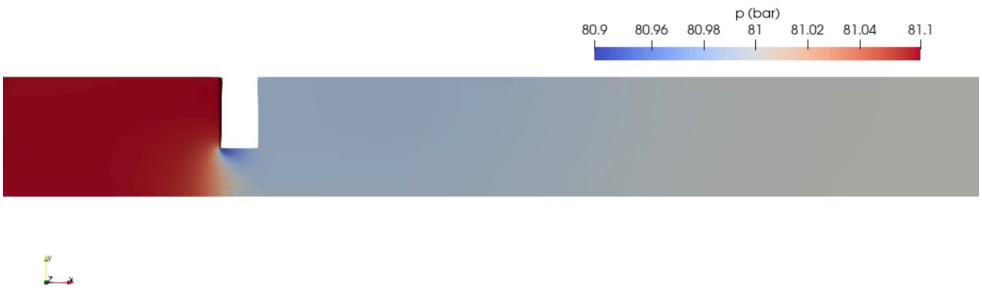

Figure A.19: Pressure contour of Case A_2 for U_{inlet} of 0.5 m/s.



Figure A.20: Temperature contour of Case A_2 for U_{inlet} of 0.5 m/s.

Figures A.21 and A.22 illustrate the velocity contour and vectors of liquid CO_2 in Case A_2, respectively, for an inlet velocity of 0.5 m/s. Figures A.23 and A.24 show the pressure and temperature contours for the same conditions.

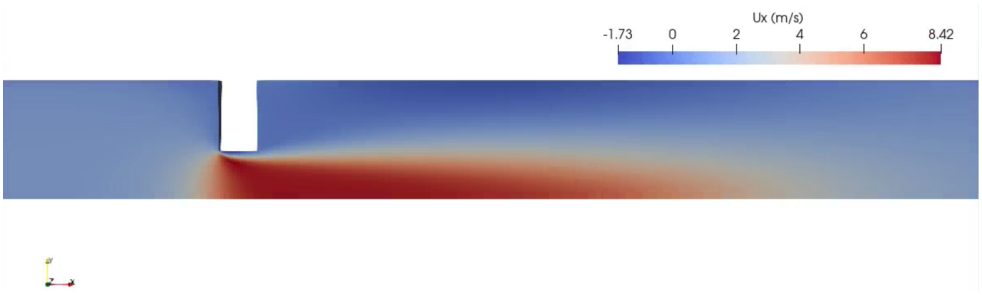

Figure A.21: Velocity contour of Case A_2 for U_{inlet} of 1 m/s.

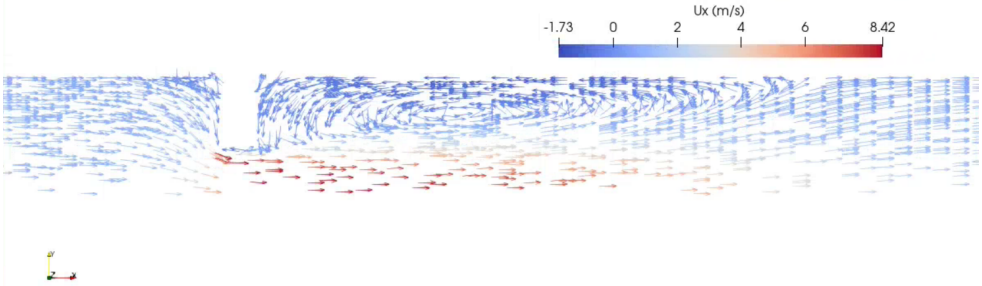

Figure A.22: Velocity vectors of Case A_2 for U_{inlet} of 1 m/s.

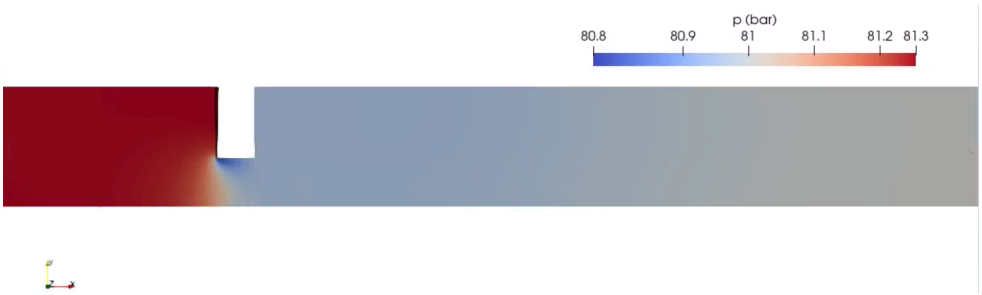

Figure A.23: Pressure contour of Case A_2 for U_{inlet} of 1 m/s.

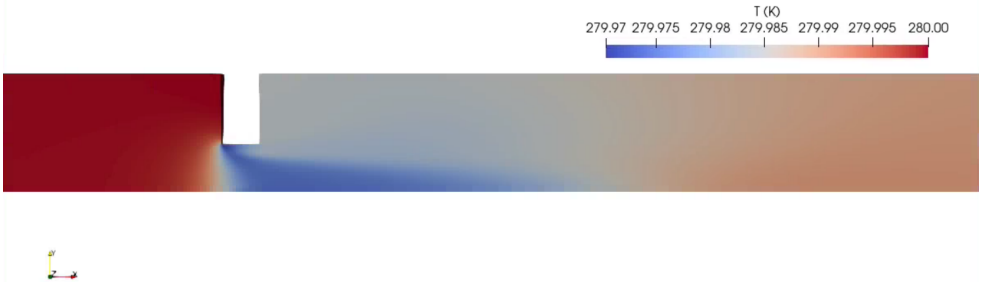

Figure A.24: Temperature contour of Case A_2 for U_{inlet} of 1 m/s.

A.4 Case B

Figures A.25 and A.26 illustrate the velocity contour and vectors, respectively, of supercritical CO_2 in Case B for an outlet pressure of 460 bar. Figures A.27 and A.28 show the pressure and temperature contours for the same conditions.

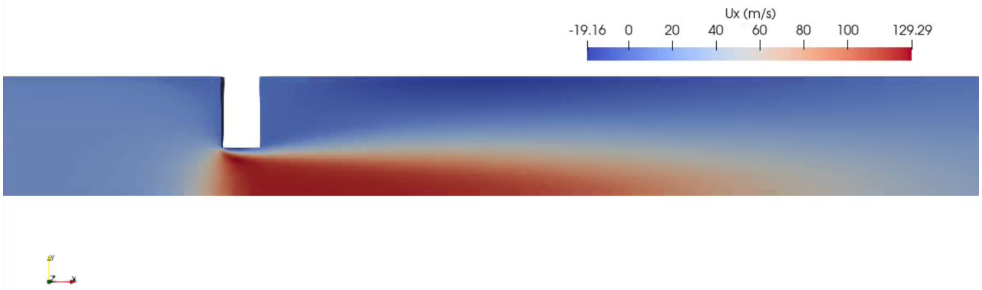

Figure A.25: Velocity contour of Case B for p_{outlet} of 460 bar.

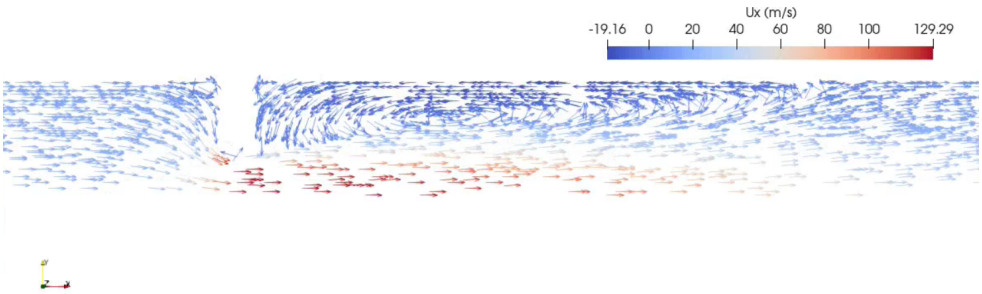

Figure A.26: Velocity vectors of Case B for p_{outlet} of 460 bar.

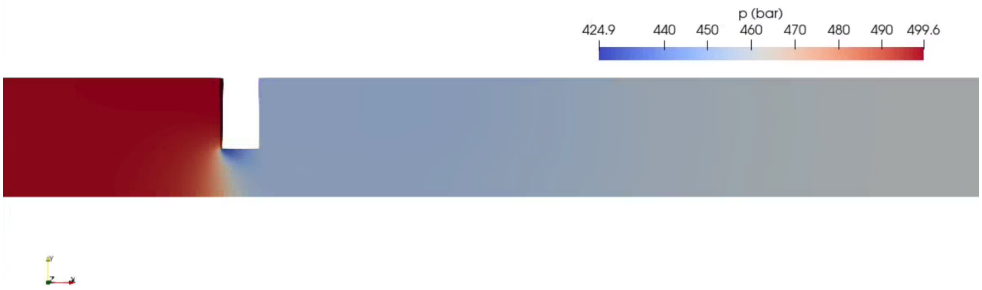

Figure A.27: Pressure contour of Case B for p_{outlet} of 460 bar.

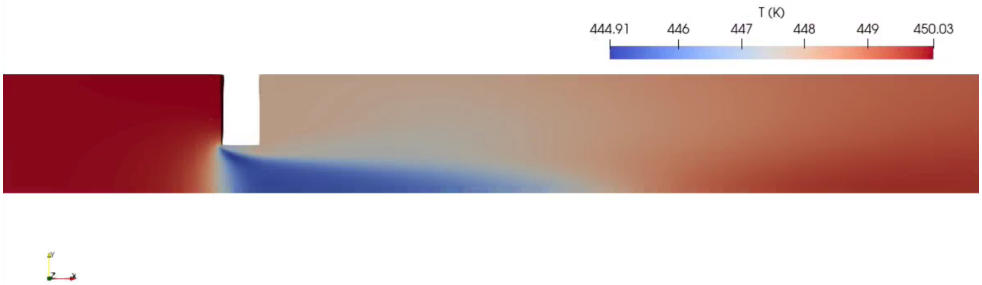

Figure A.28: Temperature contour of Case B for p_{outlet} of 460 bar.

Figures A.29 and A.30 illustrate the velocity contour and vectors, respectively, of supercritical CO_2 in Case B for an outlet pressure of 440 bar. Figures A.31 and A.32 show the pressure and temperature contours for the same conditions.

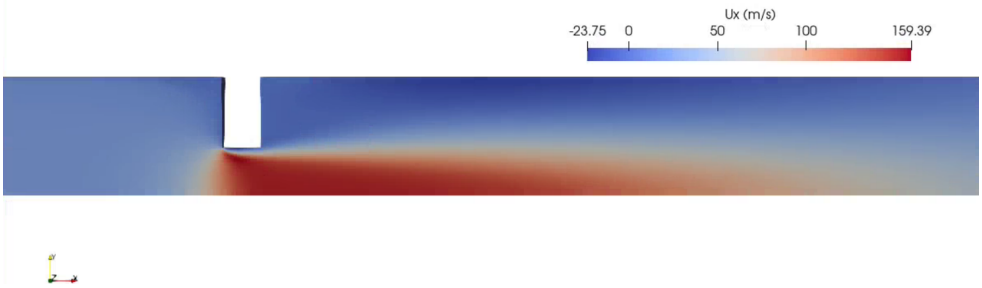

Figure A.29: Velocity contour of Case B for p_{outlet} of 440 bar.

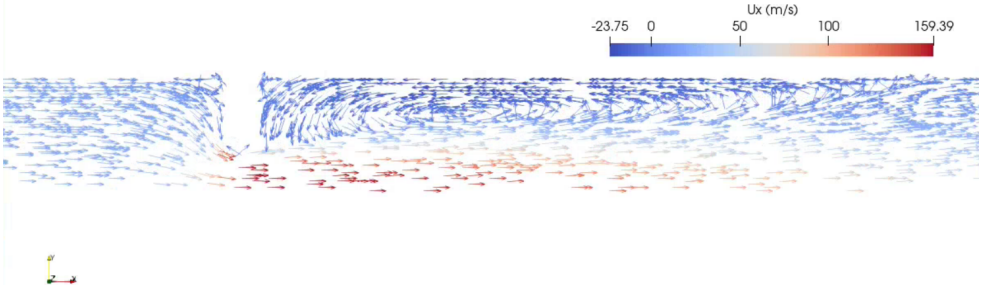

Figure A.30: Velocity vectors of Case B for p_{outlet} of 440 bar.



Figure A.31: Pressure contour of Case B for p_{outlet} of 440 bar.

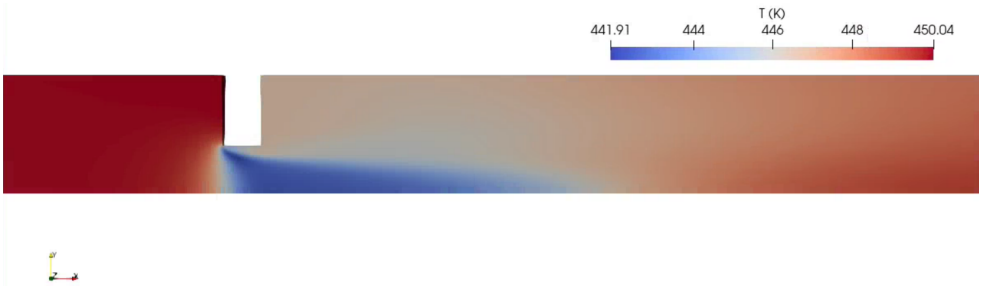

Figure A.32: Temperature contour of Case B for p_{outlet} of 440 bar.

Figures A.33 and A.34 illustrate the velocity contour and vectors, respectively, of supercritical CO_2 in Case B for an outlet pressure of 420 bar. Figures A.35 and A.36 show the pressure and temperature contours for the same conditions.

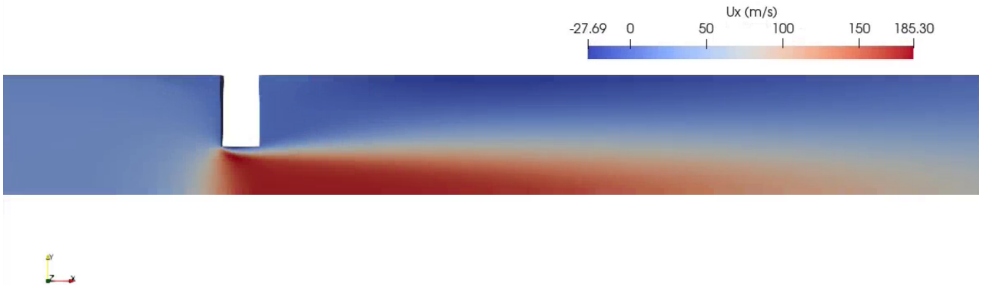

Figure A.33: Velocity contour of Case B for p_{outlet} of 420 bar.

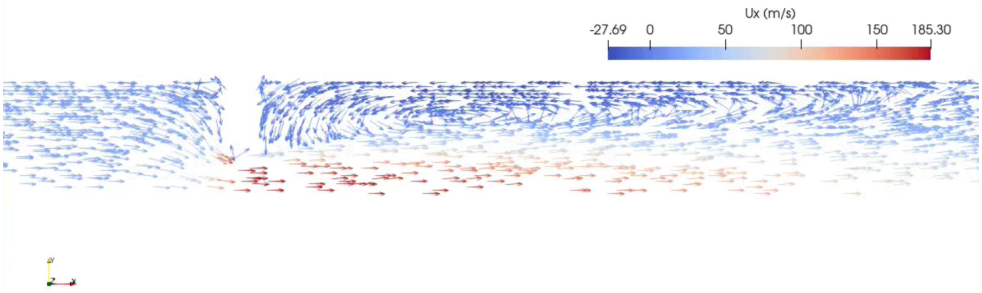

Figure A.34: Velocity vectors of Case B for p_{outlet} of 420 bar.

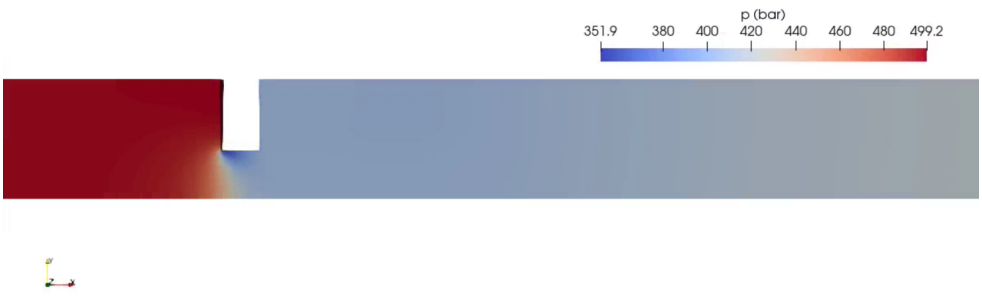

Figure A.35: Pressure contour of Case B for p_{outlet} of 420 bar.

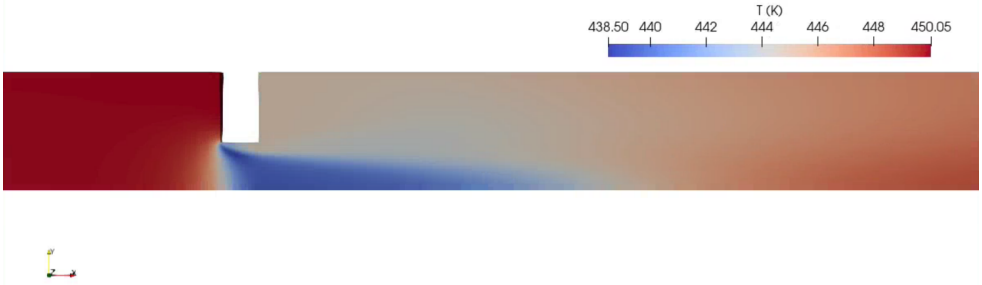

Figure A.36: Temperature contour of Case B for p_{outlet} of 420 bar.

Figures A.37 and A.38 illustrate the velocity contour and vectors, respectively, of supercritical CO_2 in Case B for an outlet pressure of 400 bar. Figures A.39 and A.40 show the pressure and temperature contours for the same conditions.

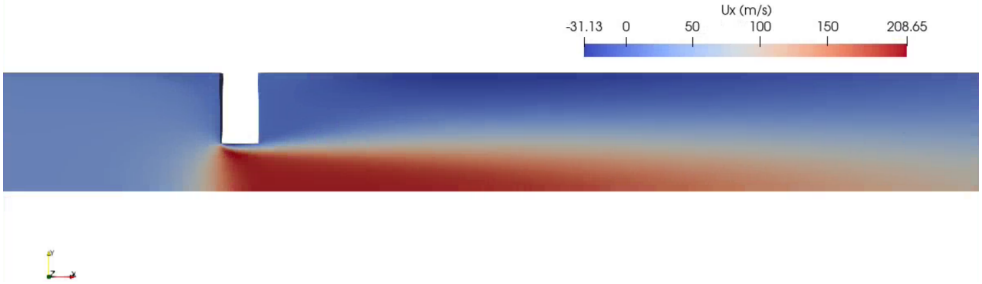

Figure A.37: Velocity contour of Case B for p_{outlet} of 400 bar.

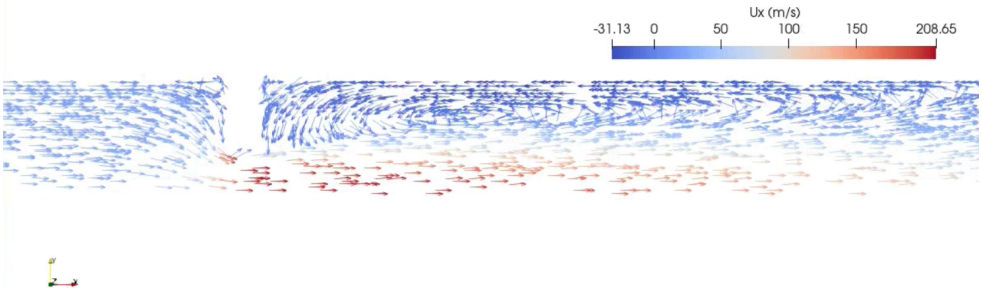

Figure A.38: Velocity vectors of Case B for p_{outlet} of 400 bar.

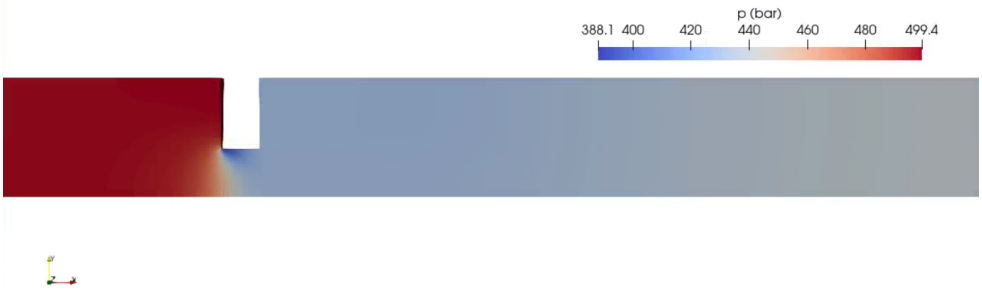

Figure A.39: Pressure contour of Case B for p_{outlet} of 400 bar.

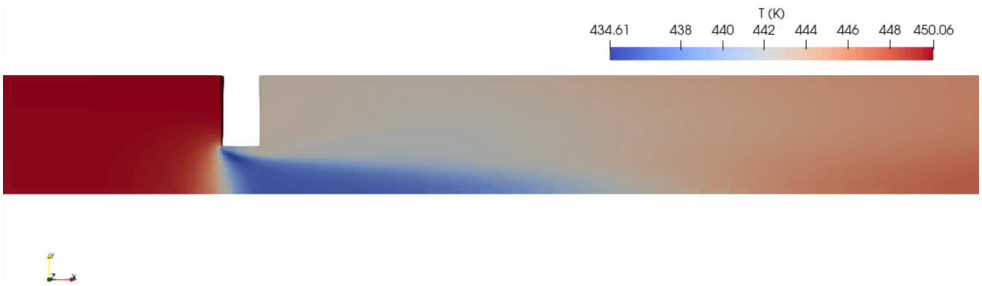

Figure A.40: Temperature contour of Case B for p_{outlet} of 400 bar.

A.5 Case C - Polynomial Pressure

Figures A.41, A.42, A.43, and A.44 illustrate the velocity, α, pressure and temperature contour, respectively, for an outlet pressure of 165 bar considering polynomial p_c.

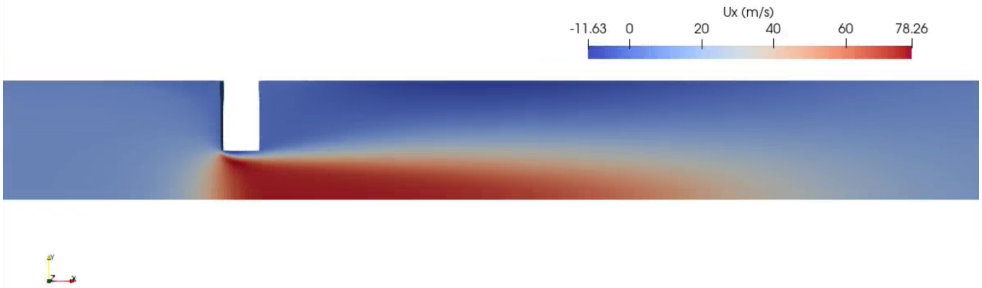

Figure A.41: Velocity contour of Case C for p_{outlet} of 165 bar, polynomial p_c.

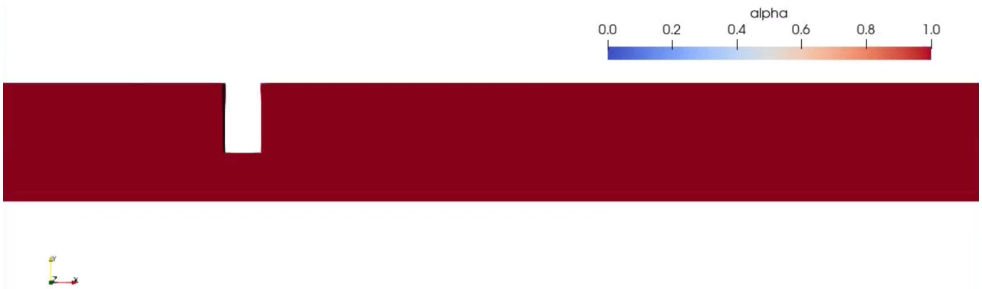

Figure A.42: α contour of Case C for p_{outlet} of 165 bar, polynomial p_c.

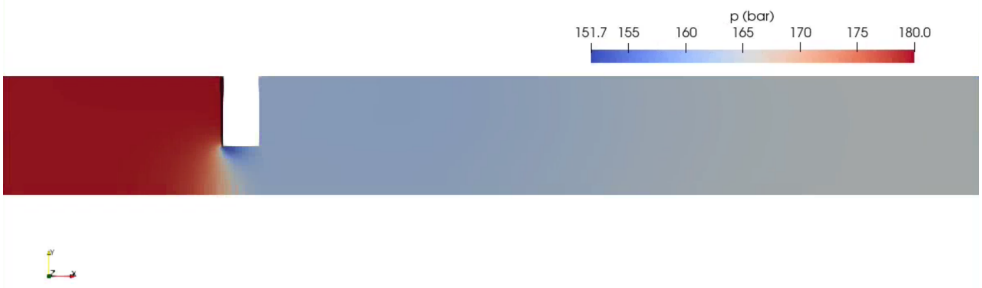

Figure A.43: Pressure contour of Case C for p_{outlet} of 165 bar, polynomial p_c.

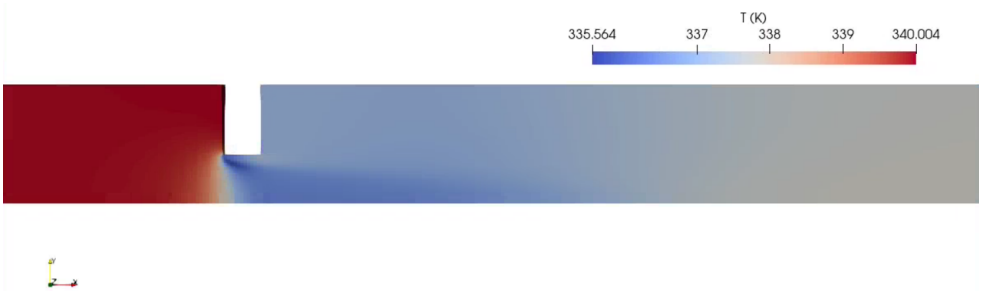

Figure A.44: Temperature contour of Case C for p_{outlet} of 165 bar, polynomial p_c.

Figures A.45, A.46, A.47, and A.48 illustrate the velocity, α, pressure and temperature contour, respectively, for an outlet pressure of 155 bar considering polynomial p_c.

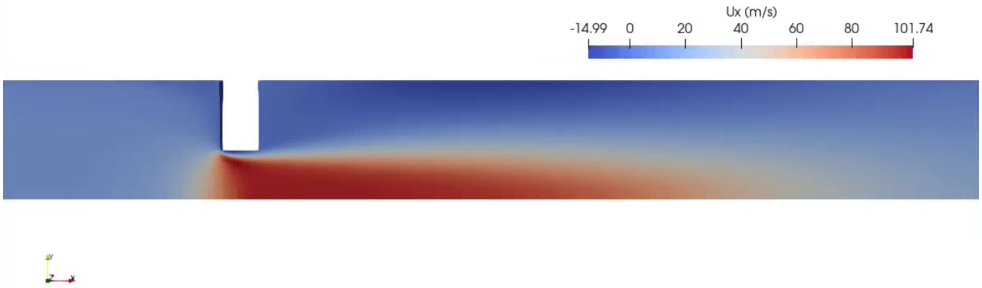

Figure A.45: Velocity contour of Case C for p_{outlet} of 155 bar, polynomial p_c.

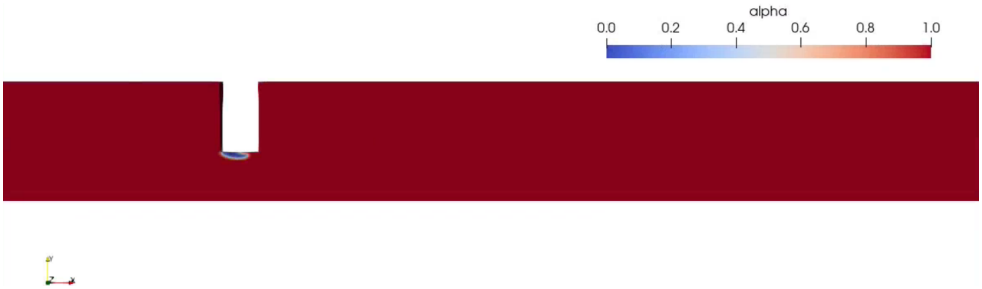

Figure A.46: α contour of Case C for p_{outlet} of 155 bar, polynomial p_c.

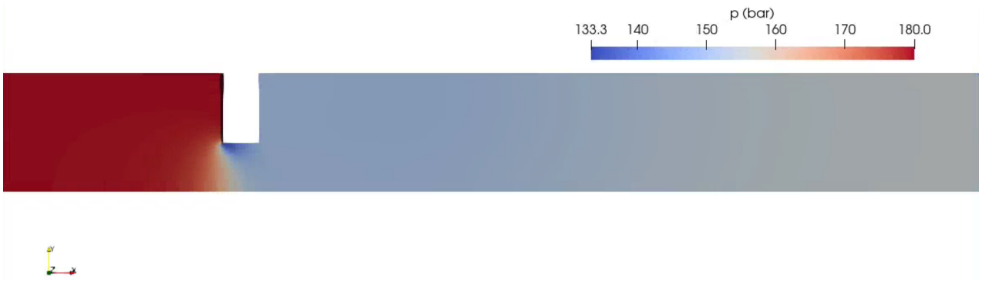

Figure A.47: Pressure contour of Case C for p_{outlet} of 155 bar, polynomial p_c.

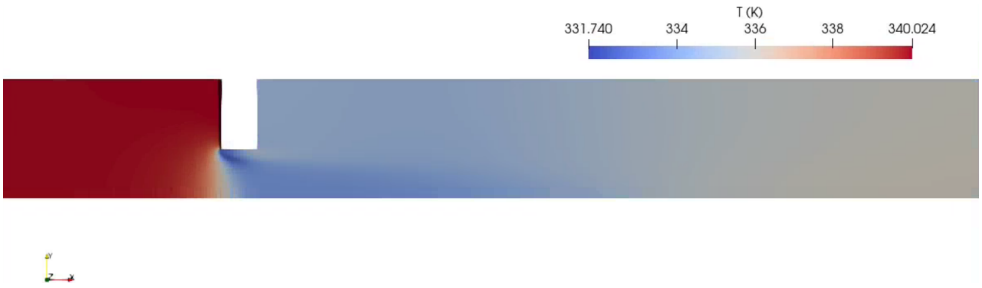

Figure A.48: Temperature contour of Case C for p_{outlet} of 155 bar, polynomial p_c.

Figures A.49, A.50, A.51, and A.52 illustrate the velocity, α, pressure and temperature contour, respectively, for an pressure outlet of 150 bar considering polynomial p_c.

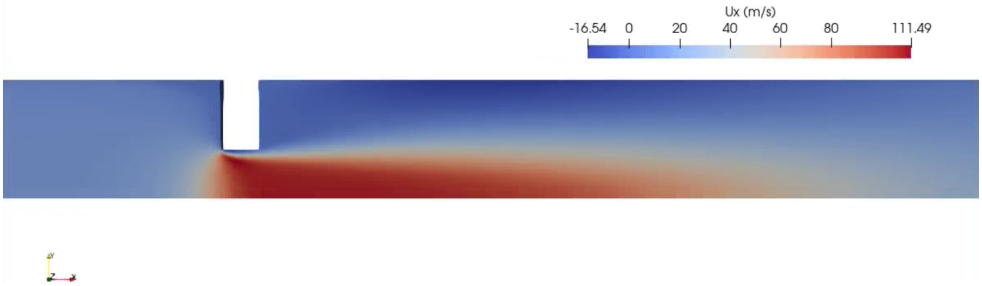

Figure A.49: Velocity contour of Case C for p_{outlet} of 150 bar, polynomial p_c.

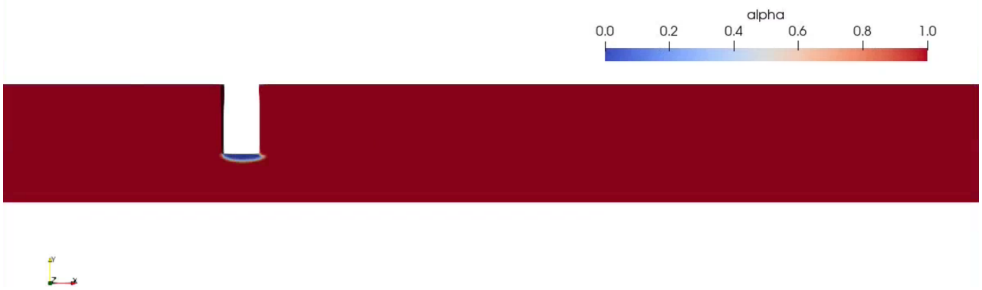

Figure A.50: α contour of Case C for p_{outlet} of 150 bar, polynomial p_c.

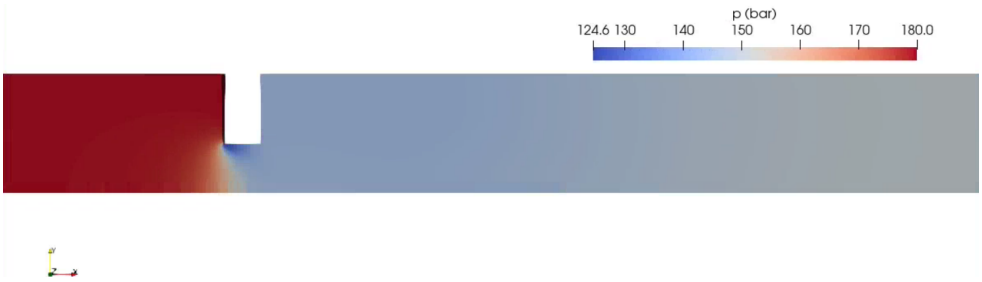

Figure A.51: Pressure contour of Case C for p_{outlet} of 150 bar, polynomial p_c.



Figure A.52: Temperature contour of Case C for p_{outlet} of 150 bar, polynomial p_c.

A.6 Case C - Constant Pressure

Figures A.53, A.54, A.55, and A.56 illustrate the velocity, α, pressure and temperature contour, respectively, for an outlet pressure of 170 bar considering constant p_c.

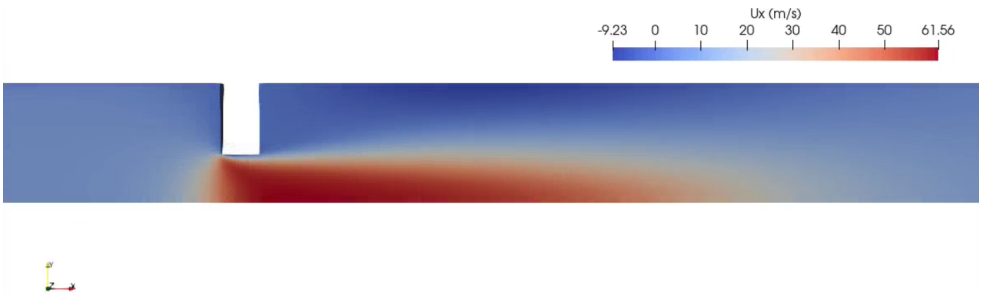

Figure A.53: Velocity contour of Case C for p_{outlet} of 170 bar, constant p_c.

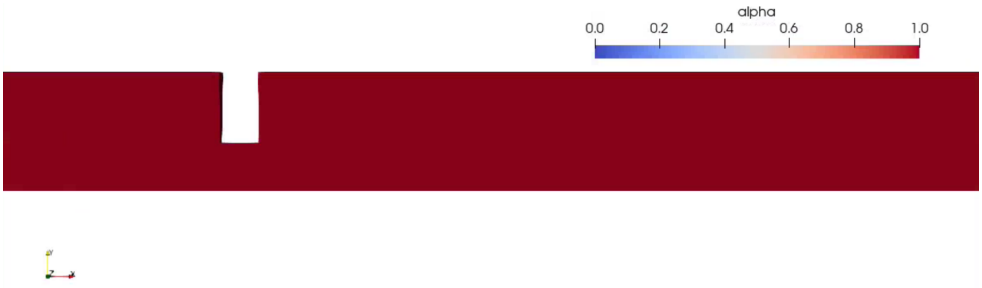

Figure A.54: α contour of Case C for p_{outlet} of 170 bar, constant p_c.

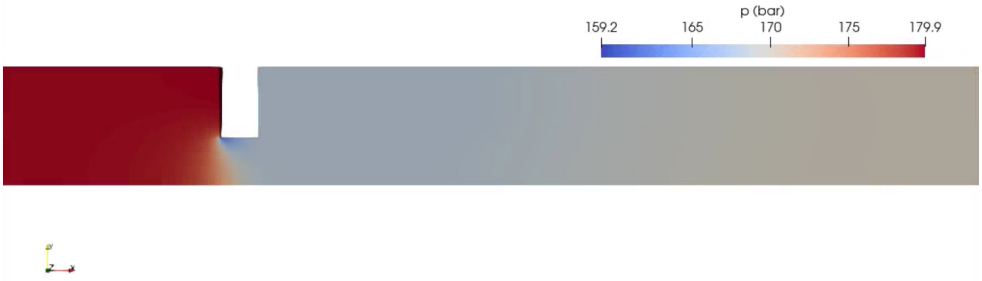

Figure A.55: Pressure contour of Case C for p_{outlet} of 170 bar, constant p_c.

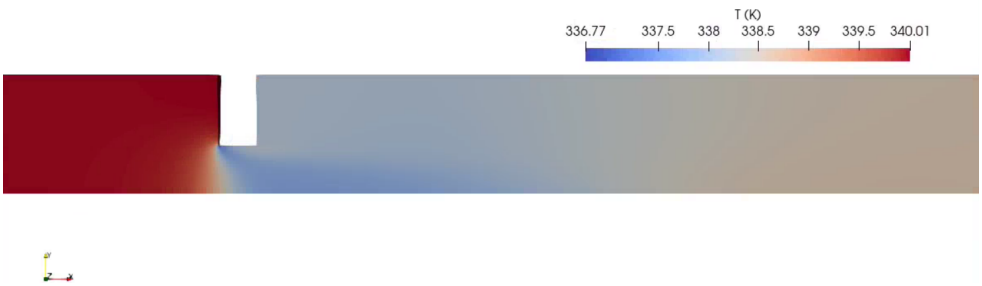

Figure A.56: Temperature contour of Case C for p_{outlet} of 170 bar, constant p_c.

Figures A.57, A.58, A.59, and A.60 illustrate the velocity, α, pressure and temperature contour, respectively, for an outlet pressure of 165 bar considering constant p_c.

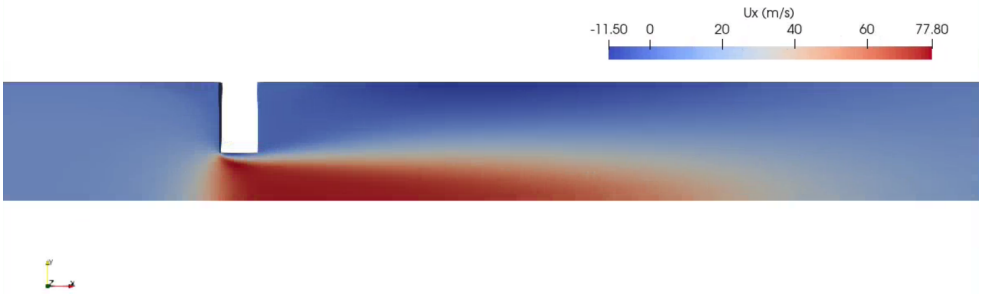

Figure A.57: Velocity contour of Case C for p_{outlet} of 165 bar, constant p_c.

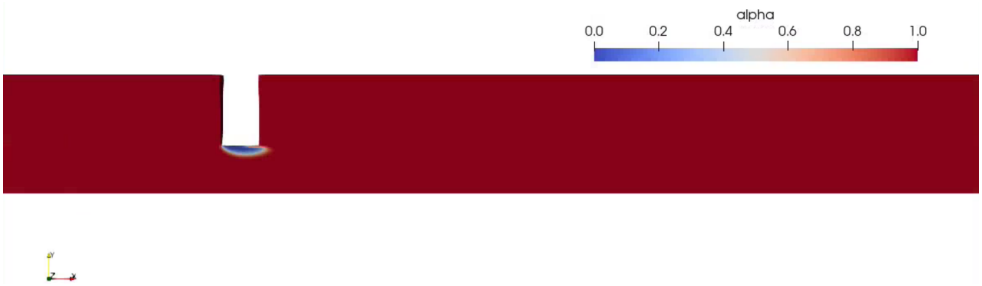

Figure A.58: α contour of Case C for p_{outlet} of 165 bar, constant p_c.

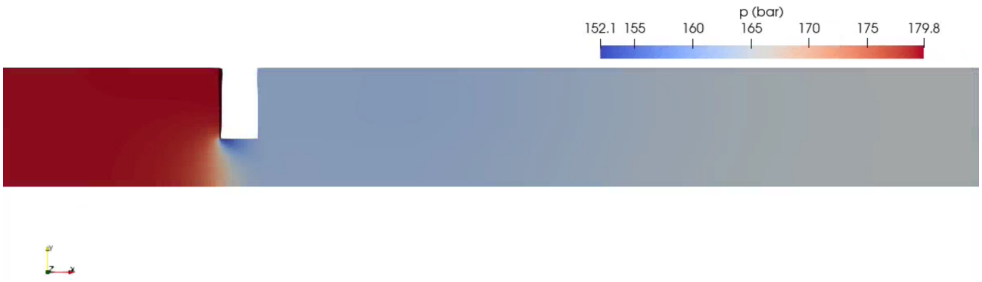

Figure A.59: Pressure contour of Case C for p_{outlet} of 165 bar, constant p_c.

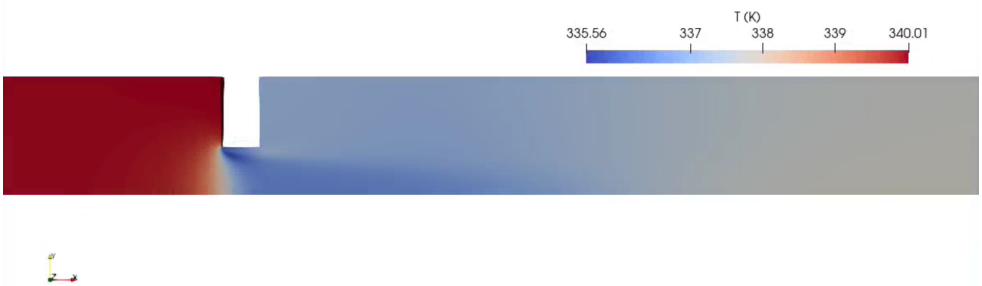

Figure A.60: Temperature contour of Case C for p_{outlet} of 165 bar, constant p_c.

Figures A.61, A.62, A.63, and A.64 illustrate the velocity, α, pressure and temperature contour, respectively, for an outlet pressure of 160 bar considering constant p_c.

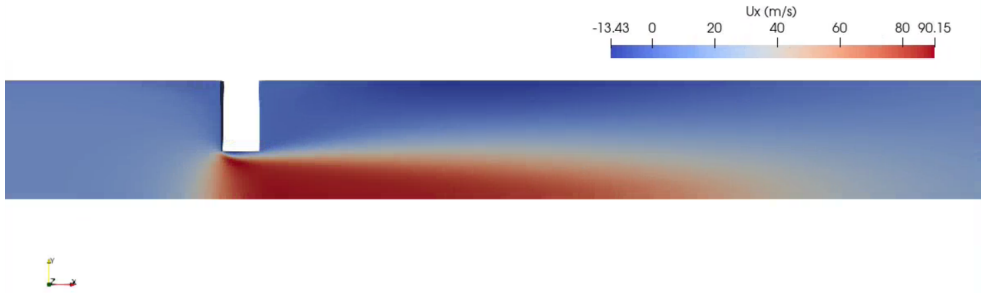

Figure A.61: Velocity contour of Case C for p_{outlet} of 160 bar, constant p_c.

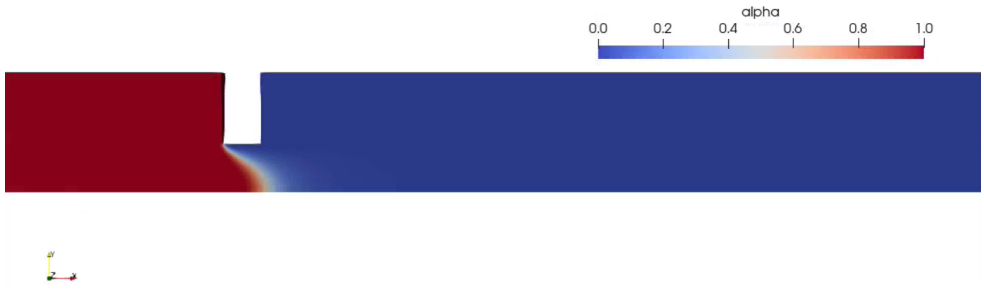

Figure A.62: α contour of Case C for p_{outlet} of 160 bar, constant p_c.

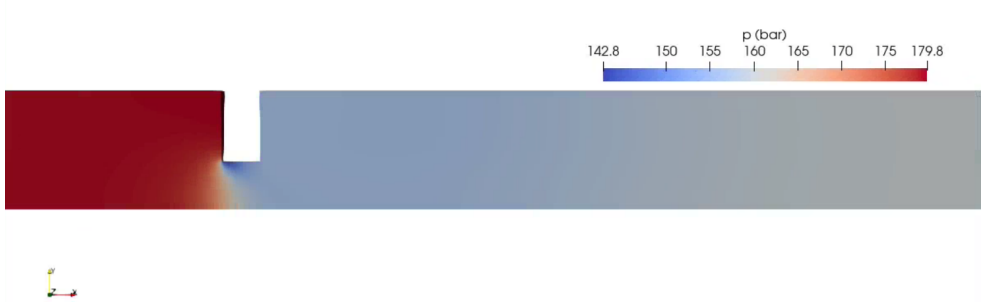

Figure A.63: Pressure contour of Case C for p_{outlet} of 160 bar, constant p_c.



Figure A.64: Temperature contour of Case C for p_{outlet} of 160 bar, constant p_c.

Figures A.65, A.66, A.67, and A.68 illustrate the velocity, α, pressure and temperature contour, respectively, for an outlet pressure of 155 bar considering constant p_c.

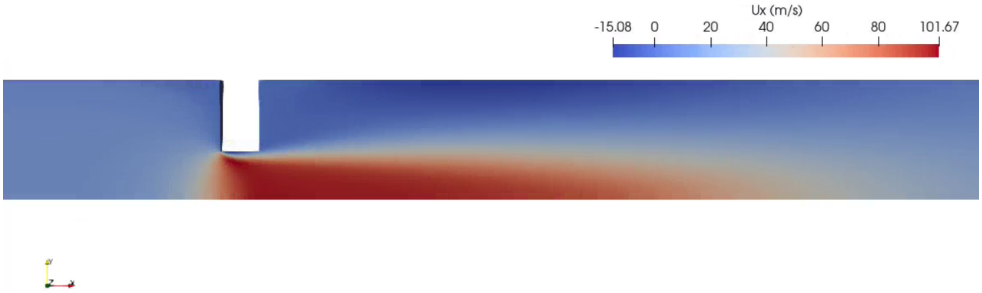

Figure A.65: Velocity contour of Case C for p_{outlet} of 155 bar, constant p_c.

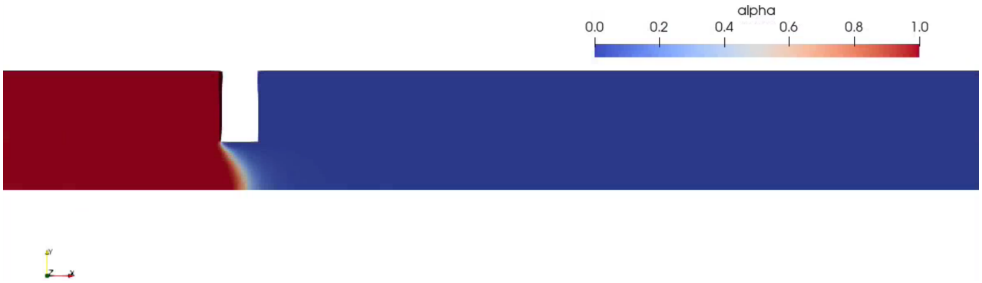

Figure A.66: α contour of Case C for p_{outlet} of 155 bar, constant p_c.

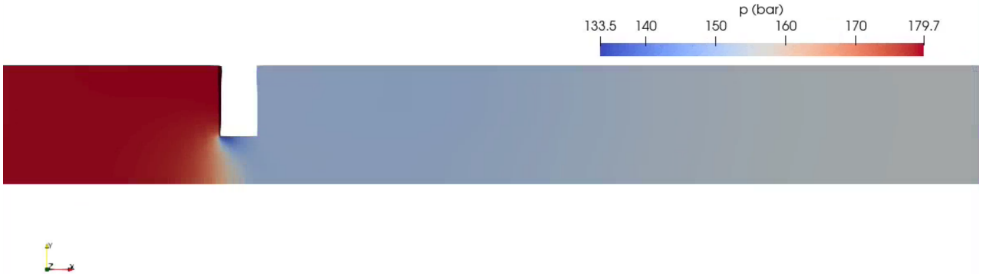

Figure A.67: Pressure contour of Case C for p_{outlet} of 155 bar, constant p_c.

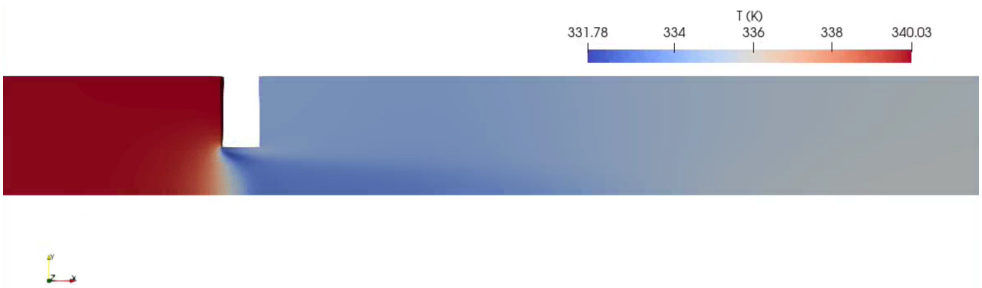

Figure A.68: Temperature contour of Case C for p_{outlet} of 155 bar, constant p_c.

Figures A.69, A.70, A.71, and A.72 illustrate the velocity, α, pressure and temperature contour, respectively, for an outlet pressure of 150 bar considering constant p_c.

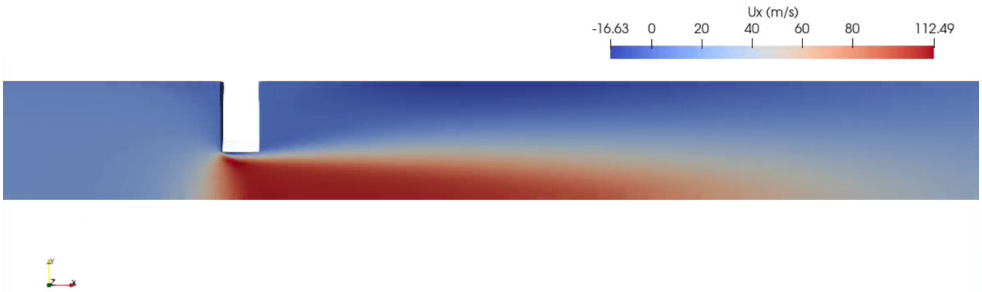

Figure A.69: Velocity contour of Case C for p_{outlet} of 150 bar, constant p_c.

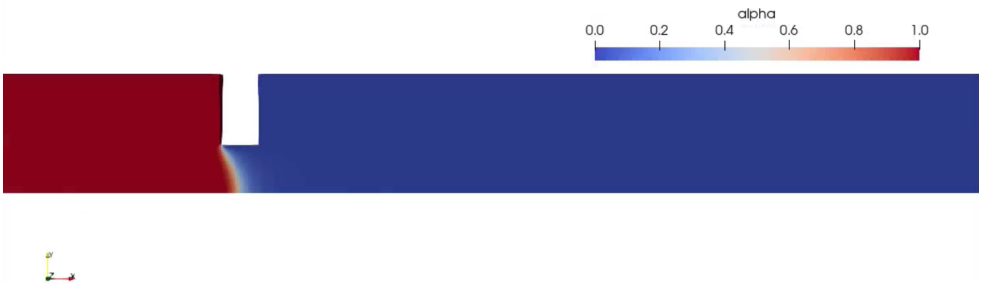

Figure A.70: α contour of Case C for p_{outlet} of 150 bar, constant p_c.

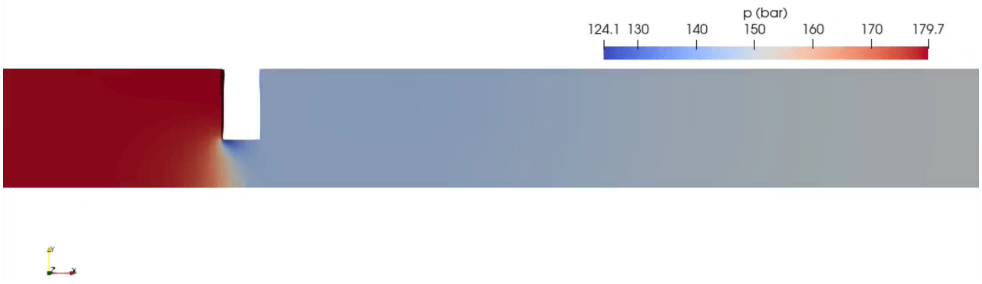

Figure A.71: Pressure contour of Case C for p_{outlet} of 150 bar, constant p_c.



Figure A.72: Temperature contour of Case C for p_{outlet} of 150 bar, constant p_c.